2D AND 3D BREAST ELASTOGRAPHY WITH A COMBINED ULTRASOUND/DIGITAL TOMOSYNTHESIS MAMMOGRAPHY SYSTEM

by

Rebecca C. Booi

A dissertation submitted in partial fulfillment
of the requirements for the degree of
Doctor of Philosophy
(Biomedical Engineering)
in The University of Michigan
2007

Doctoral Committee:

Professor Paul L. Carson, Co-Chair
Professor Matthew O'Donnell, Co-Chair
Professor Jonathan M. Rubin
Professor Mitchell M. Goodsitt
Associate Professor J. Brian Fowlkes

To Mom, Dad, Cari, Doug, and Amy

ACKNOWLEDGEMENTS

The five years that I have spent in graduate school at the University of Michigan have enriched me both intellectually and personally, thanks to my amazing advisors, professors, and colleagues. First and foremost, I would like to thank my advisors Dr. Matthew O'Donnell, Dr. Paul Carson, and Dr. Jon Rubin. Few graduate students can boast three advisors, but I consider myself very lucky to have been taught from such different and talented people. Matt: thank you for taking a chance on me, and inviting me to work with you in the BUL lab. I know that I have barely tapped into the endless knowledge you possess, but I graduate understanding what good engineering work is all about, and with the skills to apply it to the next stage in my career. Paul: you have truly been like a father-figure to me, and your support and guidance has been invaluable. Thank you for including me on the breast imaging project and for the rainbow of knowledge you have imparted on me in the areas of ultrasound, breast imaging, and elasticity. Jon: Working with you for the last year and a half has been a joy, and the enthusiasm you bring to our project is always contagious. I have learned something very different from each of you, and it has made my experience all the better.

Thank you also to my two other dissertation members: Dr. Brian Fowlkes and Dr. Mitch Goodsitt. Brian: you have always been an excellent resource for any questions I have had, and I thank you for your help with my research and our patient scans. Mitch:

your dedication to the quality of your work is admirable, and I thank you for bringing that commitment to the quality of my work, and for all your help with the patient scans.

The work in this dissertation would not have been possible without the funding provided by the National Institute of Health grants RO1-CA91713 and R21- CA109440. Additionally, the strength of this project was based on its strong collaborations through many disciplines and industries. I would like to thank General Electric Global Research Center and General Electric Health Care, especially Dr. Ajay Kapur, Dr. Anne Hall, Dr. Carl Chalek, Andrea Schmitz, and Cynthia Landberg for their contributions and dedication to this project.

A significant portion of my research has been dedicated to the clinical utility of elastography in the current diagnostic breast imaging environment, and I have many people to thank for their contributions to this area of work. First, the ultrasound and tomography team: Dr. Jerry LeCarpentier, Ganesh Narayanasamy, Sumedha Sinha, Dr. Heang-Ping Chan and of course, Mitch, Brian, and Paul. Jerry: working with you has been so much fun and I have appreciated all of your help and advice with the patient scans. On a personal note, I have treasured our bike rides and I thank you for motivating me to complete, and supporting me through the training for, the MS 150. Sumedha and Ganesh: as the other graduate students on the “breast project,” it has been great to bounce ideas off of you, and to conduct the patient scans together. Special thanks to the radiologists who have supported and guided our breast imaging project, and my thesis work: Dr. Marilyn Roubidoux, Dr. Mark Helvie, and Dr. Alexis Nees. Working with you has been a pleasure, and has shaped my understanding of the complicated process of breast lesion characterization and guided my research so that accurate, efficient

characterization can be improved. Thank you to our wonderful x-ray technologists Lisa DeCaussin, Diane Martel, and Cathy Allen and our current clinical studies coordinator, Jeanne Hill. I would especially like to thank our longtime x-ray technologist Chris Lashbrook and our previous clinical studies coordinator Sandy Wilcock for their support, advice, inspiring work ethic, and most of all, friendship.

Equally valuable to my dissertation has been the knowledge imparted on me by the current elasticity group, Dr. Kang Kim, Dr. Rick Weitzel, Dr. Jamie Hamilton, Dr. Ted Kolias, Dr. Cheri Deng, Sheng-Wen Huang, Congxian Jia, and Fong Ming Hooi. The unique mix of physicians, researchers, and students has made this a very fun, dynamic group to work with. I have been particularly proud of being part of the first all-girls elasticity group (the "Girls' Group") with Congxian and Fong Ming, who are both very smart and very sweet, where we giggled our way through our weekly meetings with Matt. More thanks to former elasticity group members over the years, Dr. Hua Xie, Dr. Ramon Erkamp, and Dr. Xunchang Chen who were pioneers for much of the work I conducted in graduate school, and who were always happy to lend a helping hand. Special thanks to Dr. Mike Richards for his camaraderie, enthusiasm, and engaging debates about everything elasticity related.

I have also had the privilege of being part of two incredible research laboratories – the Biomedical Engineering Lab (BUL lab) and the Basic Radiological Sciences (BRS) Research Group. In addition to those I have already mentioned, I would like to thank the former BULlies Dr. Christine Tse, Dr. Jessi Parsons, Dr. Tim Hall, Dr. Zhen Xu, Dr. Todd Erpelding, Dr. Marwa Zohdy, and Dr. Derek Steele for their friendship and advice over the years. Thank you and good luck to the remaining students of the BUL lab,

Congxian Jia, Ragnar Olafsson, and Yang Hou. Thank you former Kresgeans Dr. Aaron Moskalik, Dr. Jochen Kruecker, and Katy Orifici Carneal, and current Kresgeans Dr. Zhi Yang, Dr. Stan Samuel, Dr. Jingping Xu, Dr. Oliver Kripfgans, Dr. Xueding Wang, Rich Rhee, Kevin Hayworth, Nelson Chan, and Andrea Lo. It has been both a pleasure and an honor working with all of you.

Thank you to all my friends for their support and camaraderie over the years. In addition to those I have already thanked, I would like to thank the Girlsnight! group for all the fun memories, my special friends Kelly Bratic and Kiran Pandey, who I couldn't have made it through graduate school without, and my former students and good friends Misha Meerkov and Marybeth Knoth. Thank you to my dear Zach for your love, advice, friendship, and support.

Most of all, I would like to thank my family for encouraging me to make the most out of every opportunity and for their unwavering love and support through all the years. Thank you especially to my amazing parents, Daryl and Cindy Booi – I would not be anywhere without you. Thank you to my brother and sisters Cari, Doug, and Amy – you are each such wonderful and special people and I love you very much. I would also like to thank recent additions to my family, my brother-in-law Dr. Erik Nystrom, and my future sister-in-law Kris Antkowiak – you are like a brother and sister to me. I would like to thank my grandparents, Bob and Terry Rebholz and Marvin and Phyllis Booi for their endless love. Finally, I would like to send my love to the youngest members of the family, my nephews Matthew and James Nystrom, who are treasures.

TABLE OF CONTENTS

LIST OF FIGURES

LIST OF TABLES

ABSTRACT

Ultrasound elastography is a novel imaging method which acts as a surrogate to manual palpation to evaluate elastic properties of tissue. In this dissertation, elastography was conducted through a mammographic paddle in conjunction with a combined ultrasound/digital tomosynthesis mammography system to improve breast lesion characterization. Imaging through a mammographic paddle may adversely affect ultrasound image quality by reducing spatial resolution, increasing attenuation, and decreasing contrast. Thus, appropriate paddle choice is essential to create high quality through-paddle ultrasound images and strain images. Sonographic image quality through mammographic paddles of varying materials and thicknesses was compared with direct-contact (no paddle) image quality. TPX plastic paddles ≤ 2.5 mm thick performed best; when employed *in vivo*, 83% of cases produced image quality as good or better than their direct-contact analogues. Through-paddle 2D elastography was conducted through the best paddle using a 1D ultrasound transducer at 7.5 MHz and performance was compared with freehand elastography. For small strain step sizes (< 0.5%), through-paddle elastography produced correlation coefficients and strain SNR comparable to freehand elastography.

Ultimately, the aim of elastography is to acquire high quality strain estimates in 3D to fully characterize tissue. Thus, data acquisition techniques were extended to a small 3D volume. Compared with its 2D analogue, 3D elastography created higher

correlation coefficients for strain step sizes≥ 1% and at least 35% improve ment in strain SNR for all step sizes. These early successes indicate that through-paddle elastography can create high quality elastograms which might aid in breast lesion characterization. Next, through-paddle elastography was performed in 20 human subjects with varying breast masses. This dissertation introduced the elasticity characteristic “differential correlation coefficient,” which exploits the severe decorrelation observed in cysts under compression to differentiate cystic and solid masses. When applied in a clinical setting, this characteristic demonstrated potential to reduce the malignancy rating of a complicated cyst, changing management options from biopsy to imaging follow-up. Additional elastographic appearances of breast masses were evaluated, including lesion size, stiffness, margin regularity, and boundary flow. These studies suggest that elastography has potential to improve characterization of breast masses beyond x-ray tomography and sonography alone.

CHAPTER 1

INTRODUCTION

1.1. The Current State of Diagnostic Breast Imaging

Each year in the United States, more than 200,000 women are diagnosed with breast cancer and approximately 40,000 die from the disease [1]. Large clinical trials have demonstrated that early diagnosis provides the greatest opportunity for reduced mortality and long-term survival [2-3]. Mammography and ultrasound are the most common imaging modalities used to detect and characterize breast lesions, followed by magnetic resonance imaging (MRI). These modalities seek to reliably identify the many different types of breast lesions and abnormalities, including fibroadenomas, cysts (simple, complicated, and complex), calcifications, ductal carcinomas and other malignancies, and fibrocystic changes within the breast.

The primary goal of mammography is earlier detection of breast cancer in asymptomatic women [4]. The American College of Radiology (ACR) has created a Breast Imaging Reporting and Data System (BI-RADS) lexicon to standardize language in mammography reports as well as assessment of breast lesions. A summary of the mammographic appearance of breast lesions described by the ACR BI-RADS lexicon is shown in Table 1.1. To accurately characterize breast lesions, multiple descriptors including shape, margin, density, and presence or absence of architectural distortion must be reviewed [4].

Table 1.1: BI-RADS 4th Edition Terminology of the mammographic evaluation of breast masses [4].

Mammographic Evaluation of Masses	***Characteristic***
Shape	Round Oval Lobular Irregular
Margins	Circumscribed Microlobulated Obscured Indistinct or ill defined Spiculated
Density	High Equal Low Fat Containing
Architectural Distortion	Present Absent

Best descriptors of benign lesions on mammograms include round shape, circumscribed margins, and no architectural distortions. Note that a radiologist cannot distinguish between a benign cyst and benign fibroadenoma from their appearances in mammograms. In contrast, the highest indicators of malignancy are spiculated margins, lobular or irregular shapes, and high density. Unfortunately, these features can overlap between different lesion types, and most critically, between benign and malignant lesions. Thus, it is common practice in mammography to frequently recommend biopsy and make treatment recommendations based on the most worrisome feature in the image [4].

After mammographic assessment of breast tissue, a radiologist provides a final BI-RADS score (on a scale from 0-5) based on the presence of a breast lesion, its appearance in the mammogram and its likelihood of malignancy [4]. Appropriate actions are recommended based on this score. These BI-RADS assessment categories and resulting recommendation options are provided in Table 1.2.

Table 1.2: ACR BI-RADS 4th edition (2003) assessment categories and treatment recommendations [4].

Assessment Category	***Recommendation Options***
0: Need additional imaging evaluation and/or prior mammograms for comparison	Compare with previous mammograms Additional mammographic views Ultrasound MRI
1: Negative	Normal interval follow-up
2: Benign finding(s)	Normal interval follow-up
3: Probably benign	Short interval follow-up
4: Suspicious abnormality	Biopsy should be considered Needle localization and biopsy Histology using core biopsy Suggestive of malignancy – Take appropriate action Cytologic analysis
5: Highly suggestive of malignancy	Biopsy should be strongly considered Needle localization and biopsy Histology using core biopsy Highly suggestive of malignancy – Take appropriate action Cytologic analysis
6: Biopsy proven malignancy	Appropriate action should be taken

A commonly cited study using mammography as a screening tool in 1000 asymptomatic women demonstrated that mammography can detect 97% of pathologically proven cancers, including over 90% of cancers which had not spread to the axillary lymph nodes, over 90% of non-palpable malignant lesions, and over 90% of cancers smaller than 1 cm [5]. Although mammography can detect most breast cancers, the efficacy of mammography is particularly diminished in the dense breast [4]. As a result of this, and the overlapping mammographic appearances of different breast lesions, the sensitivity of screening mammography in the general population is only 68-88%, whereas the specificity is as low as 25-50% [6, 8]. The American College of Radiology (ACR) defines sensitivity as the "probability of detecting cancer when a cancer exists" and specificity as the "probability of interpreting an exam as negative when cancer does not exist" [4]. Note that there exists a tradeoff between sensitivity and specificity, identified as the area under the receiver operating characteristic (ROC) curve. The low specificity of mammography observed in practice is due in part to the fact that many clinical centers send all solid masses to biopsy. These low sensitivity and specificity scores using standard mammography as the sole screening tool suggests that additional tools are needed to accurately diagnose breast cancer and characterize benign breast lesions.

Breast sonography has demonstrated great potential for improving the specificity and sensitivity of diagnosis when used as an adjunct to mammography [7]. Kolb et al. reported that combining sonography and mammography depicted 97% of breast cancers *in dense breasts*, compared with only 48% of breast cancers depicted by mammography alone [8]. In general, the combination of both a negative mammogram and a negative sonogram reduces the likelihood of malignancy to less than 3% [4]. Note that Sickles et

al. (1983) determined that sonography is unacceptable as a screening tool, detecting just 58% of the biopsy proven cancers (mammography detected 97%) [6].

Recently, an ACR BI-RADS lexicon has been developed for ultrasound assessment of breast lesions (Table 1.3) [4]. Similar to the mammography BI-RADS lexicon, multiple sonographic features are used to fully characterize the lesion, including mass margin properties, shape, orientation, boundary, echo pattern, and posterior acoustic features. Strong indicators of malignancy include spiculated margins, irregular shape ("taller than wide"), nonparallel orientation, posterior acoustic shadowing, and microlobulation [9-11]. High predictors of benign lesions include circumscribed margins, parallel margins, oval or round shapes, and hyperechogenicity [9-11]. Fibroadenomas are the most common benign solid lesion sent to biopsy, and though 40-50% of fibroadenomas can be classified as BI-RADS 3, 50-60% of fibroadenomas have suspicious sonographic appearances which overlap with those of carcinomas [12].

Table 1.3: ACR BI-RADS ultrasound lexicon classification of breast masses (4th edition, 2003) [4].

Sonographic Evaluation of Masses	***Characteristic***
Orientation	Parallel Not parallel
Shape	Oval Round Irregular
Margin	Circumscribed Not circumscribed: indistinct, angular, microlobulated, spiculated
Lesion boundary	Abrupt interface Echogenic halo
Echo pattern	Anechoic Hypoechoic Isoechoic Hyperechoic Complex
Posterior acoustic features	None Shadowing Enhancement Combined pattern

One of the most valuable aspects of breast sonography is its ability to differentiate simple cysts from solid lesions with 98-100% accuracy, reducing biopsies of these benign breast lesions [7, 13-15]. For a cyst to be characterized as “simple”, it must exhibit all four of the following criteria: anechoic, well circumscribed, imperceptible wall, and posterior acoustic enhancement [12, 14, 16-17]. Cysts which meet some but not all of these criteria can fall into several categories, the most common being “complicated” or

“complex”. The ultrasound BI-RADS lexicon describes complicated cysts as containing homogeneous low-level internal echoes and fluid-fluid or fluid-debris levels which can shift as the patient’s position changes [4]. It also defines complex cysts as containing some discrete solid component [4]. Management options for these cysts include 6-month or 1-year imaging follow-up, aspiration, aspiration with possible core biopsy, and excisional biopsy [16, 18]. However, complicated cysts have a very low (~0.3%) malignancy rate, suggesting that if they could be accurately characterized, then they could be managed with follow-up imaging rather than aspiration or biopsy [16-17]. Non-simple cysts are common, and the percentage of cysts being classified as non-simple is increasing; therefore effective identification and management of these cysts is becoming increasingly critical [12, 16, 19-20].

It is important to note that no imaging tool can guarantee that a woman does not have breast cancer, and thus palpable breast abnormalities are recommended for biopsy [4]. The positive biopsy rate for cancer is quite low, with 70-90% of biopsies performed on women with benign masses [21-23]. Reducing biopsies could reduce costs, stress, pain, and waiting times associated with these procedures.

Because breast ultrasound examinations are currently performed free-hand by a radiologist or a technician as a supplement to mammography, these ultrasound images correspond to a different imaging geometry than the mammograms. Consequently, at least 10% of the time, there is a discrepancy between the lesions detected with the two modalities [24]. These findings suggest that additional tools are needed to accurately diagnose breast cancer.

To summarize, current limitations of breast imaging include: 1) the diminished capabilities of mammography in the dense breast due to the superposition of tissue in a single projection mammogram which camouflages masses, 2) the lack of time/space correlation between mammography and sonography which reduces the synergy between the modalities, and 3) the high biopsy rate of benign lesions created by the overlapping mammographic and sonographic appearances of malignant and benign lesions. A combined ultrasound/digital tomosynthesis mammography (DTM) system aims to address some of these limitations, as well as offer new techniques for breast lesion characterization, and will be described in the next section.

1.2. Potential Diagnostic Improvements Using a Combined Ultrasound/DTM System

To maximize the synergy between mammography and sonography, our research group at the University of Michigan, in collaboration with General Electric Global Research Center, has developed a combined imaging system which creates 3D ultrasound images and 3D digital tomosynthesis mammography (DTM) images of the breast in the same orientation at essentially the same time (Fig. 1.1) [25]. Concurrent screening using these mammography and ultrasound with high quality equipment and performed by a skilled physician is reported to significantly improve cancer detection [26-29].

The proposed method for breast imaging with this combined tomosynthesis/ultrasound system is as follows. First, tomographic projection data is obtained through a compressed breast, and then a high frequency (9-12 MHz) transducer scans with ultrasound through the same mammographic paddle while the breast is still under compression. The resulting 3D, full field of view ultrasound images can be

registered to the reconstructed tomographic slices and may obviate most handheld ultrasound. Maximizing the synergy between the two modalities could create more cost effective, efficient, and accurate diagnosis.

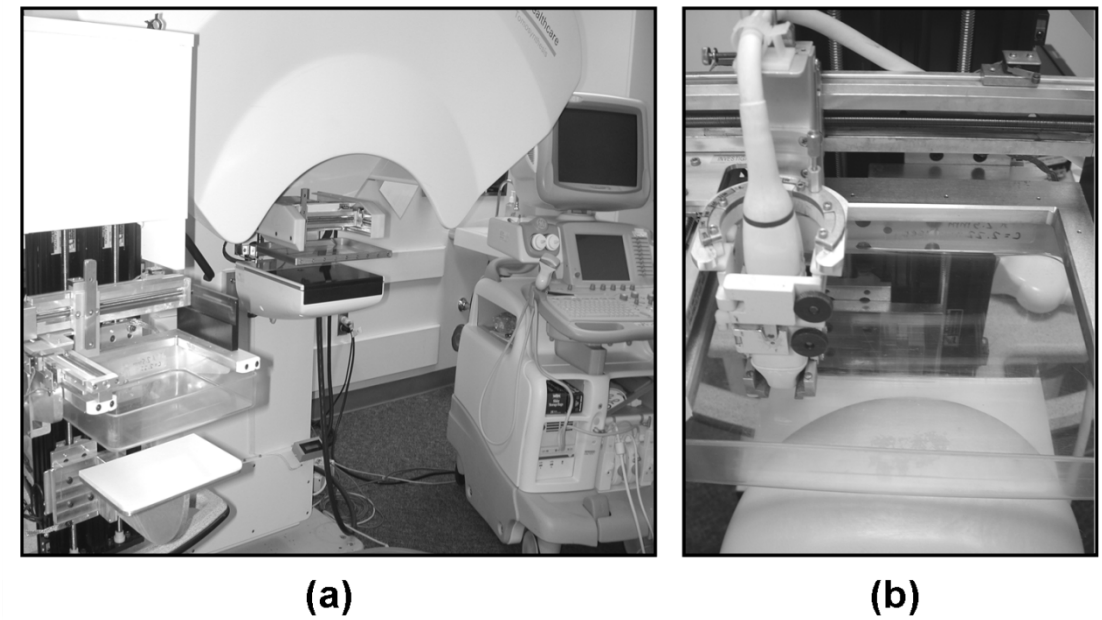

Fig. 1.1: (a) From left, stand alone mammography-mimicking unit, GE combined ultrasound/x-ray tomography unit, and GE LOGIQ 9 ultrasound scanner, **(b)** close-up view of phantom compressed in stand-alone unit with transducer and carriage attached.

Dual-mode whole-breast imaging also exhibits significant potential for advanced ultrasound modes which would provide additional information about breast tissues not available from conventional mammography or sonography. In particular, we are targeting two advanced ultrasound modes - color flow Doppler and elasticity imaging – to assess both their compatibility with the system and their ability to provide supplemental physiological and mechanical information about breast tissue. Collectively, these techniques could provide radiologists with a more complete evaluation of breast tissue, improving the fidelity of lesion detection and characterization. The focus of this dissertation is the utility of through-paddle elastography with the combined system.

1.3. The Role of Elastography in Breast Lesion Characterization

Elasticity imaging, also known as elastography, is a novel diagnostic tool that evaluates the elastic properties of tissue to distinguish between malignant and benign tissue abnormalities. In static or quasi-static ultrasound breast elastography, tissue is compressed by an externally applied force and local tissue displacements are estimated from the time delays between pre- and post-deformation images. Using 2D phase-sensitive, correlation-based ultrasound speckle tracking algorithms, described further in Chapter 2, axial (propagation and compression direction) and lateral (perpendicular to the beam direction) displacements are calculated from the time delays corresponding to the position of the maximum, normalized correlation coefficient. Thus, these algorithms output axial and lateral displacement estimates as well as the value of the correlation coefficient, a measure of the quality of the tracking at each location in the image. The gradient of the axial displacement estimate is calculated and displayed to create the final axial normal strain image, or elastogram.

Changes in tissue elasticity are usually related to an abnormal, pathological process, with malignant tissue appearing harder, or stiffer, than benign or healthy tissue. Thus, strain values obtained from elastograms can act as a surrogate for manual palpation to aid in differentiation of breast lesions.

Elastography has shown promise as a diagnostic aid in many parts of the body, including the cardiovascular system [30-32], kidney [33], deep venous thrombosis in the lower extremities [34], prostate [35-36], thyroid [37], and breast [38-41]. The most common clinically observed breast masses in the female breast are carcinomas, fibroadenomas, and cysts [42] and several studies have attempted to distinguish between

these lesions using elastography, as well as provide general benign/malignant mass differentiation [38-41]. Each of these studies used freehand elastography in the breast by manually compressing with the ultrasound transducer, sometimes attached to a small, stabilizing plate creating frame-to-frame strains between 1-1.5%. Because the clinical utility of elastography is still in its early stages, some studies have reported only qualitative findings, whereas others have tried to quantify their results. A summary of the characteristics displayed by breast masses in elastograms as well as correlation coefficient images is shown in Table 1.4. One of the most promising differentiators is the lesion size comparison between elastograms and sonograms [38-41]. Carcinomas, especially invasive ductal carcinomas, can appear larger in elastograms than their corresponding ultrasound images because their infiltration into surrounding tissue results in the stiffening of those tissues, a property called desmoplasia [39]. This characteristic is not normally noted on sonograms, but recent studies have shown that using a cutoff ratio between the lesion area in the elastogram and lesion area in the sonogram of 1.2 or greater produces 94-100% sensitivity and 25-75% specificity [40-41]. While other studies suggest this high sensitivity is at the great expense of specificity, it is clear that elastography provides different tissue properties than those recorded with sonography and DTM alone [40]. In contrast, benign lesions appear similar in size or slightly smaller in elastograms than sonograms.

More specifically, both carcinomas and fibroadenomas can appear stiff in elastograms. However, fibroadenomas exhibit several interesting elastographic characteristics that carcinomas do not. First, fibroadenoma contrast can decrease with increased pre-compression, an observation made in 74% (14 of 19) of fibroadenomas

studied by Hall et al [39]. Additionally, because fibroadenomas are typically stiffer than surrounding tissue but do not infiltrate, they experience a degree of mobility under compression. This can create boundary flow in the elastogram – a region of high strain (soft tissue) surrounding one or more sides of the fibroadenoma [43]. Unfortunately, the stiffness of fibroadenomas can vary, as can their visibility in elastograms. Garra et al. reported 40% of fibroadenomas were the same stiffness or softer than surrounding tissue. In the same study, 91% of carcinomas were stiffer than surrounding tissue. Garra et al. also evaluated margin regularity and margin definition between cysts, fibroadenomas, and carcinomas, but did not find significantly different values between benign and malignant lesions [38].

Recent studies attempting to characterize cysts with elastograms have had limited, and sometimes conflicting, results [37-39, 41]. These findings indicated that cysts can demonstrate a variety of appearances in elastograms, depending on the ultrasound scanner used, percent compression and pre-compression, type of signal processing, and biological variations in the cyst itself. Using a Diasonics ultrasound scanner, Garra et al. described three different elastographic patterns in the eight cysts studied: 1) a stiffer (darker) area with a softer (brighter) center, 2) a uniformly stiff area, and 3) an area with both soft and stiff regions [38]. Using a Siemens ultrasound scanner, Barr reported that both simple and complicated cysts appeared stiffer in elastograms with a softer, “bulls-eye” appearance in the middle of the cyst [41]. Most notably, Hall et al. described that because echo signals or noise from cysts rapidly decorrelate, they can appear relatively stiff or soft in elastograms, often depending on how much strain is applied [39].

Table 1.4 Summary of elastographic characteristics of breast masses [38-41].[†]

Elastographic Evaluation of Masses		***Characteristic***
Elastogram	Lesion Size Comparison: Elastogram to Sonogram	Smaller in elastogram Similar to sonogram Larger (> 1.2x) in elastogram
	Relative Stiffness	Much harder (stiffer) Harder Same as surrounding tissue Softer Much softer
	Margin regularity	Smooth and round Irregular Combination
	Margin definition	Sharp Somewhat sharp or slightly indistinct Indistinct
	Effect of increased pre-compression on contrast	No effect Contrast changes unpredictably Contrast decreases with pre-compression Contrast increases with pre-compression
	Elastographic pattern	Uniform Heterogeneously softer and stiffer Complex
	Slip boundary	Present/Absent
Correlation coefficient image	Correlation coefficient comparison	Much lower in lesion Lower in lesion Similar to surrounding tissue Higher in lesion Much higher in lesion

[†] Tabulated from four independent studies evaluating elastographic breast lesion behavior in 252 patients with 313 lesions (235 benign, 78 malignant).

1.4. Original Contributions of Thesis

The goal of this dissertation is to obtain high quality 2D and 3D elastography results through a mammographic paddle in conjunction with the combined ultrasound/digital tomosynthesis mammography system. Furthermore, new methods of lesion characterization are explored and the clinical utility of elastography with the combined system is assessed.

Elastography with the combined system holds several advantages over conventional freehand elastography. Compressing the breast with a mammographic paddle improves breast stability and compression uniformity. The transducer carriage prevents out-of-plane motion created by transducer rotation during compression, a significant concern during freehand elastography. Because compression is automated, operator skill will no longer be a major factor in image quality. Additionally, compression steps can be controlled with great precision and to a wide range of sizes.

With this system, 3D elastography using a 1D linear array transducer is also possible, by automating the compression process and controlling elevational step size. Imaging over a single plane limits the fidelity of elasticity imaging, but when extended to three dimensions, information provided by strain images covers a larger area of the breast and is more robust and reproducible. Implementing 3D speckle tracking over a 3D volume improves tracking accuracy and reduce artifacts and decorrelation by tracking out-of-plane motion, while increasing robustness by imaging over a breast volume. The resulting elastograms have increased contrast-to-noise ratio (CNR) over their 2D analogues, which directly corresponds to increased lesion visibility when applied *in vivo*. Most importantly, unlike freehand elastography, elasticity images with the combined

system are obtained in the breast in the same orientation as the corresponding tomosynthesis images, 3D grayscale B-mode ultrasound images, and Doppler ultrasound images. This allows direct comparisons between several imaging modalities for improved breast lesion characterization.

The remaining chapters in this dissertation are summarized below:

Chapter 2 provides a technical basis for the work presented in the following chapters. Speckle behavior in ultrasound images is reviewed, as the presence of speckle and its characteristics drive tracking precision and capabilities in elastography. The derivation of 2D phase-sensitive, ultrasonic speckle tracking from analytical and basebanded ultrasound signals is provided, and resulting artifacts and limitations are discussed. Finally, the extension of these algorithms to include tracking in the elevational direction is presented, and potential improvements in tracking capabilities with 3D speckle tracking are discussed.

Chapter 3 provides the groundwork for ultrasound imaging through a mammographic paddle by comparing important aspects of ultrasound image quality - including the point spread function (a measure of spatial resolution and speckle spot size in all 3 directions), sidelobes, reverberations, contrast and attenuation - when no paddle is present and when mammographic paddles of different materials and thicknesses are present. In particular, lexan and TPX paddles are directly compared for several thicknesses and the implications of through-paddle sonography on elasticity imaging are discussed. Portions of the work contained in Chapter 3 were presented at the 2004 IEEE Ultrasonics Symposium and the 2004 Radiological Society of North American

Symposium, and were subsequently published in *Ultrasound in Medicine and Biology*. The relevant citations for this work are:

1. Booi RC, Krücker JF, Goodsitt MM, O'Donnell M, Kapur A, LeCarpentier GL, Roubidoux MA, Fowlkes JB, Carson PL. Evaluating thin compression paddles for mammographically compatible ultrasound. Ultrasound in Medicine and Biology 2007; 33(3): 472-482.
2. Booi RC, Krücker J, Goodsitt MM, O'Donnell M, Kapur A, LeCarpentier GL, Roubidoux MA, Fowlkes JB, Carson PL. "Evaluation of thin compression plates for mammographically compatible breast ultrasound." Proceedings of the 2004 IEEE Ultrasonics Symposium; p. 2129-2132.

Chapter 4 explores the utility of through-paddle elastography by comparing elastographic image quality, specifically CNR, correlation coefficient values, and out-of-plane motion, for several paddle thicknesses (0.25, 1.0, 2.5 mm) as well as transducer types (M12L, 10L, and 7L) and frequencies (5-10 MHz) on a tissue-mimicking phantom. Using the best combination of these parameters, a final, through-paddle 2D elastogram is presented and compared with an elastogram using freehand elastography under the same conditions. The efficacy of 3D elastography is also explored and features such as scanning speed and time, scanning direction, and mechanical backlash are quantified to determine the best data acquisition techniques for fast, reliable 3D elastography. Resulting elastograms and correlation coefficients will be compared with their 2D analogues. Limitations of this work will also be addressed. Portions of the work presented in Chapter 4 were presented at the 2005 and 2006 IEEE Ultrasonics Symposiums. The relevant citations are:

1. Booi RC, O'Donnell M, Knoth MM, Xie H, Hall AL, Rubin JM, Carson PL. "3D breast elastography with a combined ultrasound/tomography system." Proceedings of the 2006 IEEE Ultrasonics Symposium; p. 2056-2059.

2. Booi RC, Carson PL, Erkamp RQ, Xie H, Kapur A, LeCarpentier GL, Roubidoux MA, Fowlkes JB, O'Donnell M. "Applying *in vitro* elasticity imaging results to

optimize *in vivo* breast lesion characterization using a combined 3D ultrasound/digital x-ray system." Proceedings of the 2005 IEEE Ultrasonics Symposium; p. 727-730.

Chapter 5 assesses the clinical utility of 2D and 3D elastography with the combined system. Most notably, in response to confusion over description and management of benign complicated cysts, and their conflicting appearances in elastograms, the high decorrelation rate associated with cysts in cross-correlation imaging is evaluated to determine whether it could be used directly to distinguish cysts from solid masses. Additionally, a reader study reviewed by 2 radiologists in the Breast Imaging Division at the University of Michigan assigns a BI-RADS score and percent likelihood of malignancy score to the 17 breast lesions imaged with tomosynthesis, ultrasound, and elastography. Finally, the characteristics of the 3 most common clinically observed breast lesions – carcinomas, fibroadenomas, and cysts – are reviewed by the 2 radiologists and summarized to determine which descriptors can best predict lesion type and likelihood of malignancy. Portions of the work presented in Chapter 5 were presented at the 2005 Radiological Society of North America Symposium, the 2005 Biomedical Engineering Society Symposium, the 2006 Tissue Elasticity Conference, and the 2007 American Institute of Ultrasound in Medicine Convention, and are in press in *Journal of Ultrasound in Medicine* and *Ultrasound in Medicine and Biology*. The relevant citations are:

1. Booi RC, Carson PL, O'Donnell M, Richards MS, Rubin JM. Diagnosing cysts with correlation coefficient images from 2D freehand elastography. Journal of Ultrasound in Medicine 2007 *(in press).*
2. Booi RC, Carson PL, O'Donnell M, Roubidoux MA, Hall AL, Rubin JM. Characterization of cysts using differential correlation coefficient values from 2D and 3D elastography. Ultrasound in Medicine and Biology 2007 *(in press).*

Chapter 6 provides a summary of the experimental work detailed in this dissertation and recommends future work based on promising results as well as limitations. Using cross-beam imaging to improve lateral displacement estimate quality is discussed, and the potential of using elastography to monitor changes in breast tumor elasticity before, during, and after chemotherapy as a predictor of complete response is addressed.

1.5. References

[1] Monticciolo D. Breast Disease: Anatomy, Pathology, and Diagnosis. RSNA Categorical Course in Diagnostic Radiology Physics: Advances in Breast Imaging – Physics, Technology, and Clinical Applications 2004, p 9-16.

[2] Shapiro S. Periodic breast cancer screening in seven foreign countries. Cancer 1992; 69:1919-1924.

[3] Verbeek ALM, Hendriks JH, Holland M, Mravunac F, Sturmans NE, Day NE. Reduction of breast cancer mortality through mass screening with modern mammography. Lancet 1984; 1:1222-1224.

[4] American College of Radiology (ACR). Breast imaging reporting and data system (BI-RADS) 4th edition. Reston, VA: American College of Radiology; 2003.

[5] Sickles EA, Filly RA, Callen PW. Breast cancer detection with sonography and mammography: comparison using state-of-the-art equipment. AJR 1983; 140:843-845.

[6] Taylor KJW, Merritt C, Piccoli C, et al. Ultrasound as a complement to mammography and breast examination to characterize breast masses. Ultrasound in Med. and Biol. 2002; 28(1): 19-26.

[7] Jackson VP. The current role of US in breast imaging. Radiol Clin North Am 1995; 33(6): 1167-1170.

[8] Kolb TM, Lichy J, Newhouse JH. Comparison of the performance of screening mammography, physical examination, and breast US and evaluation of factors that influence them: an analysis of 27,825 patient evaluations. Radiology 2002; 225(1): 165-175.

[9] Stavros AT, Thickman D, Rapp CL, Dennis MA, Parker SH, Sisney GA. Solid breast nodules: use of sonography to distinguish between benign and malignant lesions. Radiology 1995; 196: 123-134.

[10] Hong AS, Rosen EL, Soo MS, Baker JA. BI-RADS for sonography: positive and negative predictive values of sonographic features. AJR 2005; 184: 1260-1265.

[11] Cho N, Moon WK, Cha JH, et al. Differentiating benign from malignant solid breast masses: comparison of two-dimensional and three-dimensional US. Radiology 2006; 240(1): 26-32.

[12] Stavros AT. Breast Ultrasound. Philadelphia, PA: Lippincott Williams & Wilkins, 2004; 276-350.

[13] Sickles EA, Filly RA, Callen PW. Benign breast lesions: ultrasound detection and diagnosis. Radiology 1984; 151:467-470.

[14] Hilton SV, Leopold GR, Olson LK, Willson SA. Real-time breast sonography: application in 300 consecutive patients. AJR Am J Roentgenol 1986; 147:479-486.

[15] Bassett LW, Kimme-Smith C. Breast sonography. AJR Am J Roentgenol 1991; 156:449-455.

[16] Venta LA, Kim JP, Pelloski CE, Morrow M. Management of complex breast cysts. AJR Am J Roentgenol 1999; 173:1331-1336.

[17] Berg WA, Campassi CI, Ioffe OB. Cystic lesions of the breast: Sonographic-pathologic correlation. Radiology 2003; 227:183-191.

[18] Mendelson EB, Berg WA, Merritt CR. Toward a standardized breast ultrasound lexicon, BI-RADS: ultrasound. Semin Roentgenol 2001; 36:217-225.

[19] Jackson VP. The role of US in breast imaging. Radiology 1990; 177:305-311.

[20] Parker SH, Jobe WE. Percutaneous breast biopsy, 1st ed. New York: Raven, 1993: 111-114.

[21] Gisvold JJ, Marin JK Jr. Prebiopsy localization of nonpalpable breast lesions. AJR 1984; 143:477-481.

[22] Rosenberg AL, Schwartz GF, Feig SA, Patchefsky AS. Clinically occult breast lesions: localization and significance. Radiology 1987; 162: 167-170.

[23] Bassett LW, Liu TH, Giuliano AI, Gold RH. The prevalence of carcinoma in palpable vs impalpable, mammographically detected lesions (comment). AJR 1992; 158: 688-689.

[24] Conway WF, Hayes CS, Brewer WH. Occult breast masses: Use of mammographic localizing grid for US evaluation. Radiology 1991; 181: 143-146.

[25] Kapur A, Carson PL, Eberhard J, et al. Combination of digital mammography with semi-automated 3D breast ultrasound. Technol Cancer Res. Treat 2004; 3(4):325-334.

[26] Novak D. Indications for and comparative diagnostic value of combined ultrasound and x-ray mammography. Eur J Rad 1983; 3 Suppl 1: 299-302.

[27] Kolb TM, Lichy J, Newhouse JH. Occult cancer in women with dense breasts: Detection with screening ultrasound: Diagnostic yield and tumor characteristics. Radiology 1998; 207: 191-198.

[28] Brem RF and Gatewood OMB. Template-guided breast US. Radiology 1992; 184: 872-874.

[29] Lunt LG, Peakman DJ, Young JR. Mammographically guided ultrasound: a new technique for assessment of impalpable breast lesions. Clin Radiol 1991; 44(2):85-88.

[30] Chen X, Li X, Sahn D, Kim K, Xie H, and O'Donnell M. Evaluation of 2-D Speckle Tracking Based Strain Rate Imaging (SRI) using a 3-D Heart Simulation Model. IEEE Ultrasonics Symposium Proceedings 2004; 2125-2128.

[31] Céspedes EI, de Korte CL, van der Steen AFW, von Birgelen C, Lancée CT. Intravascular elastography: Principle and potentials. Sem Interventional Cardiol 1997; 2:55-62.

[32] de Korte CL, Pastercamp G, van der Steen AFW, Woutman HA, Bom N. Characterization of plaque components with intravascular ultrasound elastography in human femoral and coronary arteries in vitro. Circulation 2000; 102:617-623.

[33] Weitzel WF, Kim K, Rubin JM, Xie H, O'Donnell M. Renal advances in ultrasound elasticity imaging: measuring the compliance of arteries and kidneys in end-stage renal disease. Blood Purif. 2005; 23(1):10-7.

[34] Rubin JM, Xie H, Kim K, Weitzel WF, Emelianov SY, Aglyamov SR, Wakefield TW, Urquhart AG, O'Donnell M. Sonographic elasticity imaging of acute and chronic deep venous thrombosis in humans. J Ultrasound Med. 2006 Sep;25(9):1179-86.

[35] Lorenz A, Sommerfield HJ, Garcia-Schurmann MG, Philippou S, Senge T, Ermert H. A new system for the acquisition of ultrasonic multi-compression strain images of human prostate in vivo. IEEE Trans Ultrason, Ferroelectr Freq Contr 1999; 46(5):1147-1154.

[36] Pesavento A, Lorenz A, Siebers S, Ermert H. New real-time strain imaging concepts using diagnostic ultrasound. Phys Med Biol 2000; 45:1423-1435.

[37] Lyshchik A, Higashi T, Asato R, et al. Thyroid Gland Tumor Diagnosis at US Elastography. Radiology 2005 237: 202-211.

[38] Garra BS, Céspedes EI, Ophir J, et al. Elastography of breast lesions: initial clinical results. Radiology 1997; 202:79-86.

[39] Hall TJ, Zhu Y, Spalding CS. In vivo real-time freehand palpation imaging. Ultrasound Med Biol 2003; 29:427-435.

[40] Regner DM, Hesley GK, Hangiandreou NJ, et al. Breast lesions: evaluation with ultrasound strain imaging – clinical experience of multiple observers. Radiology 2006; 238(2): 425-437.

[41] Barr RG. Clinical applications of a real time elastography technique in breast imaging. Proceedings of the 5th International Conference on the Ultrasonic Measurement and Imaging of Tissue Elasticity. 2006; p. 112.

[42] Harper P. Ultrasound mammography. Baltimore: University Park Press, 1985.

[43] Jiang J and Hall TJ. A novel lateral motion tracking algorithm and its application in shear strain imaging: a feasibility study. Proceedings of the 5th International Conference on the Ultrasonic Measurement and Imaging of Tissue Elasticity. 2006; p.107.

CHAPTER 2

2D AND 3D PHASE SENSITIVE, ULTRASONIC SPECKLE TRACKING FOR ELASTOGRAPHY

2.1. Chapter Overview

The process of quantitative elasticity imaging comprises three parts: 1) evaluation of tissue motion by tracking speckle displacements, 2) estimation of strain tensor components, and 3) reconstruction of the tissue elastic modulus from the resulting strain images [1]. “Speckle” is the granular appearance observed in brightness mode (B-mode) ultrasound images and is produced by coherent interference at the transducer face of echoes from scatterers with tissue. As tissue is deformed, speckle moves with the ultrasonic scatterers and this motion is tracked in elastography. When speckle is fully-developed, it follows a stochastic process which can be described using correlation-based processing. Correlation-based processing has been used to estimate motion in many previous studies [1-5] and has been shown to be the maximum likelihood estimator (MLE) for constant time delay estimation when using properly pre-filtered signals [6]. In this chapter, the origin and behavior of fully-developed speckle in ultrasound images is explored, as this behavior drives the fundamentals of elastography. Next, how speckle motion is tracked using correlation-based, time-delay estimation techniques and how strain images are derived from the resulting displacement estimates are detailed. Limitations of these techniques and potential artifacts in the final images are discussed. Finally, methods for reconstructing the tissue elastic modulus are briefly reviewed.

2.2. Behavior of Speckle in Ultrasonic B-mode Images

2.2.1. Origin of Speckle

B-mode ultrasound image acquisition begins when a transducer fires a series of spherical (if focused system) or planar (if non-focused system) acoustic pulses into tissue. The resulting waves interact with the tissue and a component of their echoes is reflected back to the transducer face. These echoes are created by radiation effects between the sound waves and tissue structures [7]. If a structure is larger than a wavelength, this event is called specular reflection; if the structure is much smaller than a wavelength it is called scattering [7].

A resolution cell in tissue is defined as the volume of material over which the echo is produced [8]. Within each cell there are a large number of randomly distributed complex point scatterers exhibiting echo different magnitudes and phases [7]. The magnitude of the echo is related to the strength of its reflection, whereas its phase corresponds to a delay caused by the scatterer's position and is uniformly distributed between 0 and 2π for any imaging system, with resolving power limited by the ultrasonic wavelength [7]. It is important to note that the scatterer density in a resolution cell is assumed to be very high in tissue [9]. Therefore, individual scatterers cannot be resolved and the speckle pattern of an image only contains *statistical* information regarding the physical properties of the wave source [9]. In this way, imaging the same region of tissue under the same imaging circumstances produces identical speckle patterns; imaging the same region of tissue under different imaging circumstances produces very different speckle patterns. This is an important point, as much previous work has been conducted to extract medical information directly from speckle, but without success. As will be

described in section 2.2.3, many ultrasound parameters influence speckle patterns, and extensive knowledge of all of them would be required before speckle could describe properties of tissue, rather than the imaging system.

An acoustic pulse traveling through tissue will be aberrated by interference with these multiple resolution cell scatterers, intervening media, varying acoustic velocities, frequency dependent attenuation, and reverberation from multiple targets [10]. Thus, echoes returning to the detector are no longer perfectly spherical or planar [10]. The detection system in ultrasound imaging is phase-sensitive, meaning that detection of the returning wave is instantaneous and not averaged over many cycles [10]. When the aberrated wavefront is phase detected, the complex summation of overlapping echoes with varying phases across the aperture creates amplitudes ranging from dark (destructive interference of echoes) to bright (constructive interference), giving the granularity characteristic of speckle [10]. This process is described as a random walk process, and follows a Rayleigh distribution, which will be discussed further in the next section [9].

Thus, in summary, speckle is created by the constructive and destructive interference of echoes returning to the transducer face after interactions with tissue, and its incidence is related to the large number of randomly distributed scatterers in a resolution cell [7].

2.2.2. First and Second Order Speckle Characteristics

Ultrasonic speckle can be characterized by stochastic analysis [9]. This chapter will limit itself to the statistics of “fully developed” speckle; that is, speckle which results from echoes from five or more scatterers per period [11]. For this case, echoes returning

to the transducer experience a uniformly distributed phase (0 - 2π), and the summation of these echoes is a linear, spatially invariant process [9]. The result of this complex summation at the transducer face is a complex field with real and imaginary parts which follow a joint circular Gaussian probability distribution [9]. The envelope of the echo amplitude thus has a Rayleigh probability distribution function (pdf) of:

$$p(V) = \frac{V}{\sigma^2} \exp \frac{\left(-V^2\right)}{2\sigma^2} \qquad \textbf{(2.1)}$$

where V is the calculated envelope expressed by the inphase, X, and quadrature, Y, components as $V = \sqrt{X^2 + Y^2}$, and σ^2 is the variance [9]. An ideal Rayleigh probability density function of acoustic speckle is shown in Fig. 2.1.

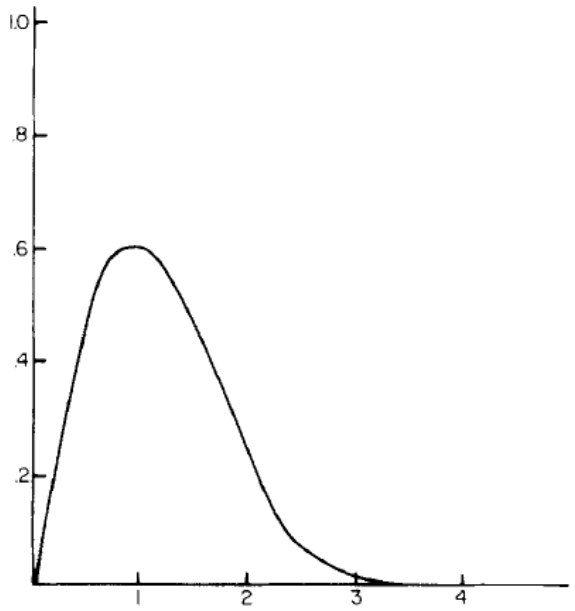

Fig. 2.1: Ideal Rayleigh probability density function (PDF) created by [10] for fully developed acoustic speckle. The y-axis in this figure is *p(V)* and the x-axis is *V*.

The second order statistics of speckle describe its correlation properties and can be used to determine the average speckle size in the ultrasound image [9, 12-13]. Smith and Wagner have demonstrated that both the autocorrelation function and autocovariance

function equivalently measure average speckle size [12]. These processes are quantified by the full-width-at-half-maximum (FWHM) in the axial and lateral directions, which is the -6 dB width of the ideal Gaussian pulse [13]. Thus the FWHMs in each direction are independent at the focus and proportional to the point spread function (PSF) of the transducer [13].

The autocorrelation $R_{XX}(t_1, t_2)$ of a process *X* is defined as the joint moment of the random variables $X(t_1)$ and $X(t_2)$, and is given by [9]:

$$R_{XX}(t_1, t_2) = \left\langle X(t_1) X^*(t_2) \right\rangle = E[X_1 X_2] \qquad \textbf{(2.2)}$$

Equation 2.2 indicates that the autocorrelation function is simply the expected value of a product. If the process *X* is wide sense stationary, then its mean, or expected, value is constant. When this is the case, the autocorrelation can be treated as the function of one variable, $|t_2 - t_1|$. Thus, if t_1 and t_2 are time points, separated by a lag τ, then the autocorrelation would no longer be a function of the time at which it was computed, but only a function of the correlation lag. In this case, the global maximum of the autocorrelation function is at $\tau = 0$.

$$R_{XX}(t_1, t_1 + \tau) = E[X(t_1) X^*(t_1 + \tau)] = R_{XX}(\tau) \qquad \textbf{(2.3)}$$

Similarly, the autocovariance function of *X* is the covariance of the random variables $X(x_1)$ and $X(x_2)$:

$$C_X(x_1, x_2) = \langle \left[X(x_1) - \left\langle X(x_1) \right\rangle \right] \left[X^*(x_2) - \left\langle X^*(x_2) \right\rangle \right] \rangle \qquad \textbf{(2.4)}$$

where $\left\langle X(x_1) \right\rangle$ is the expected value of X at position x_i, and the asterisk denotes complex conjugation [9].

Figure 2.2 shows experimental axial (along the beam direction) and lateral (perpendicular to beam direction) autocorrelation functions at 1.8 cm depth in breast tissue, which produces fully-developed speckle, imaged at 7.5 MHz using a GE LOGIQ 9 ultrasound scanner. These images were calculated from the FWHM of the autocorrelation function averaged over multiple locations as a function of lag, as described in equation 2.3.

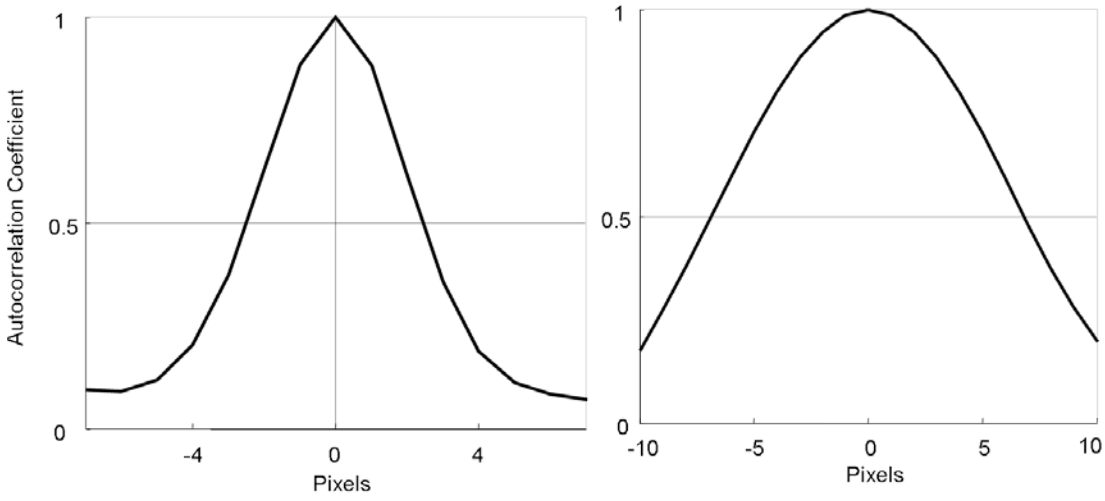

Fig. 2.2: Autocorrelation plots in lateral **(left)** and axial **(right)** directions at 1.8 cm depth. Data was obtained using a 7.5 MHz transducer and GE LOGIQ 9 scanner imaged over human breast tissue. Speckle spot size is determined from the FWHM, which, under these conditions, is approximately 7x15 pixels, corresponding to 0.92x0.28mm (lateral x axial).

2.2.3. Parameters Influencing Speckle

When an object is imaged under exactly the same circumstances, its speckle pattern does not change [14]. This demonstrates that though speckle patterns are random, they are not random in the same sense as electrical noise. However, if the same region of the object is imaged using different ultrasound imaging parameters, the speckle pattern will be quite different [14]. Speckle is thus influenced by many imaging characteristics, including depth of field and focus, attenuation, and transducer center frequency,

bandwidth, and aperture size [10, 13, 15-16]. Understanding the effects of changing these parameters will become important for the next section, which evaluates both the reduction of speckle in images and the extraction of information from speckle.

The lateral PSF of an ultrasound system is highly depth dependent on beam diffraction and focusing [13]. Therefore, the speckle, which was shown in Section 2.2.2 to be proportional to the PSF, is also depth dependent. Thijssen et al. reported the change in speckle size with depth by showing that the lateral speckle size is relatively small near the transducer face, and then gradually increases up to and beyond the focus of the transducer [13]. This effect is further amplified when attenuation is present in the system, which occurs in all "real" tissue [13]. Attenuation blocks high frequencies, gradually shifting the frequency spectrum of the system down as depth increases [13]. The outcome of this shift is the proportional increasing in lateral speckle size with depth [13]. To account for this depth-dependence in practice, the average speckle size in the ultrasound image is used for speckle tracking. In contrast, axial speckle size remains fairly constant with depth because the pulse envelope remains nearly constant with depth, though other pulse characteristics, such as amplitude and mean frequency, change [13]. An experimental example of different speckle patterns at two depths is provided in Fig. 2.3.

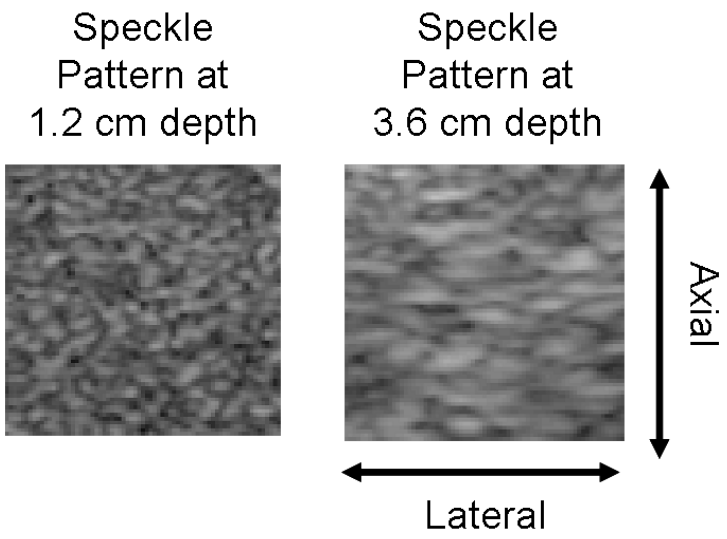

Fig. 2.3: Speckle patterns created in a tissue-mimicking rubber breast phantom (model BB-1, ATS Laboratories, Bridgeport, CT, USA) imaged with a 10L transducer at 7.5 MHz at 1.2 cm and 3.6 cm, demonstrating the increased lateral speckle size with depth.

Speckle pattern also changes with varying acoustic center frequency and bandwidth [15]. In general, the greater the center frequency shift, the more uncorrelated the speckle patterns become [15]. Additionally, for a given center frequency shift, longer acoustical (greater bandwidth) pulses decorrelate more quickly than shorter pulses [15].

Change in speckle pattern can also be expressed as a function of lateral translation [16]. For linear arrays which are focused on the target of interest, the theoretical correlation curve can be expressed as $\rho(b) = (1 - b/A)^2$ where b is the lateral translation and A is the aperture length. Consequently, the larger the array length, the more slowly the speckle pattern decorrelates. Speckle patterns are thus nearly independent when translation is 40-50% of array length [14, 16]. In practice, more rapid decorrelation occurs for speckle patterns which are not at the focus of the imaging system [16]. However, when the target is in the focal zone, the rate of correlation coefficient decrease as a function of lateral translation is independent of frequency and target range [16].

2.2.4. Speckle: Artifact vs. Information

Speckle is considered both an undesirable artifact which decreases lesion contrast resolution and a vital tool for extracting additional information. Speckle creates fine-false structures whose resolution is too small for the imaging system, thus masking true tissue boundaries [7]. Many methods to reduce speckle have been explored by researchers, including speckle reduction imaging, frequency compounding and spatial compounding [17]. Spatial compounding is the most common method for reducing speckle to improve object visibility, image contrast, and signal-to-noise ratio (SNR) [14, 16].

Conversely, speckle can be utilized as a potential source of information on tissue characteristics, capable of providing information regarding whether tissue is benign or malignant, including tissue characterization using power spectral density, spectral correlation, and, the focus of this dissertation, elastography [18-21]. Details of evaluating tissue elasticity via tracking speckle are described in the remainder of this chapter.

2.3. Phase-Sensitive, Correlation-Based Speckle Tracking

Displacement estimation in elastography has been derived from time delay estimation techniques [22]. In practice, ultrasonic elasticity imaging begins by compressing tissue and measuring the time delay between corresponding RF signals in the pre-deformation and post-deformation images. These time delays are later expressed as displacements using the equation:

$$\upsilon = \tau * \frac{c}{2} \qquad \textbf{(2.5)}$$

Where ν is the axial displacement, τ is the time delay, c is the speed of sound in the medium, generally assumed constant at 1.54 mm/μs in tissue, and the factor of 2 accounts for pulse-echo propagation.

Techniques for tracking tissue motion using speckle tracking algorithms from RF ultrasound images will initially be described in one dimension for clarity, and later will be extended to their 2D and 3D forms, which were used for processing all data collected in this dissertation. The mathematical derivation below is a summary of the methods described in [1, 3-5, 23-24].

Briefly, it is important to note that there are other methods to induce tissue displacements and measure the body's response to deformation besides those used in this dissertation. Internal motion generated by the body, such as cardiac motion, has been used to study the elastic properties of the heart [4]. Additionally, internal deformations can be generated by the radiation force produced by an external transducer [25]. Ultrasonic displacement imaging has also been achieved using optical flow [26] and Fourier-based methods [27], in addition to the correlation-based processing described below. In general, the desired process of deformation and displacement estimation techniques will depend on the application.

2.3.1. Time-Delay Estimation using Correlation-Based Processing

For an isolated point scatterer lying along the beam line, the axial RF signal recorded by the ultrasound imaging system can be described as a cosine-modulated envelope:

$$s_1(t) = A(t-\tau_0)\cos\left(\omega_0(t-\tau_0)\right) \qquad \textbf{(2.6)}$$

where τ_0 is the round-trip propagation time from the transducer to the point scatterer, $s_1(t)$ is the impulse response, *A(t)* is the envelope of the transceived Gaussian pulse, and ω_0 is the angular carrier frequency of the ultrasound signal [1]. After tissue compression in the axial direction, this equation becomes:

$$s_2(t) = A(t-\tau_1)\cos[\omega_0(t-\tau_1)] \quad \textbf{(2.7)}$$

where $s_2(t)$ is the delayed signal of $s_1(t)$ by time $(\tau_1 - \tau_0)$. Describing these signals in their complex forms allows phase information to be extracted:

$$s_1(t) = A(t-\tau_0)\left[\frac{e^{j\omega_0(t-\tau_0)} + e^{-j\omega_0(t-\tau_0)}}{2}\right] \quad \textbf{(2.8)}$$

$$s_2(t) = A(t-\tau_1)\left[\frac{e^{j\omega_0(t-\tau_1)} + e^{-j\omega_0(t-\tau_1)}}{2}\right] \quad \textbf{(2.9)}$$

It is computationally expensive to directly apply correlation methods to determine displacement estimates from the RF signal, so, in practice, analysis is conducted on the analytic or complex baseband signals derived from the original RF signal. Note that correlation-based speckle tracking using analytic and baseband signals produces estimate variances that are approximately the same as with full RF processing [1]. To convert from the original RF signal to the analytic signal, the negative frequency component is removed, and the positive frequency component is doubled, giving:

$$a_1(t) = A(t-\tau_0)e^{j\omega_0(t-\tau_0)} \quad \textbf{(2.10)}$$

$$a_2(t) = A(t-\tau_1)e^{j\omega_0(t-\tau_1)} \quad \textbf{(2.11)}$$

Only the positive analytic signal is required for analysis because the negative analytic signal gives precisely the same information.

Displacement between two frames under axial compression is calculated using the complex correlation between the frames. Because fully-developed speckle characteristics can be described using correlation-based processing, the complex correlation function is estimated over a given kernel, spatially equivalent to one speckle spot, of length T at time t:

$$\hat{R}_{12}(\tau) = \frac{1}{T}\int_0^T a_1(t)a_2^{*}(t+\tau)dt \qquad \textbf{(2.12)}$$

One speckle spot is chosen for the length of the correlation kernel because the displacement error is at its minimum over this window size, regardless of strain step size, and the strain can be calculated as the derivative of the displacement over this region [3].

The cross-correlation function is normalized to the correlation coefficient, ρ, which has values in the range [-1, 1]. If the correlation function is not normalized, then bright speckle spots will dominate analysis [3]. For a zero-mean signal, ρ at time *t* can be described as:

$$\hat{\rho}_{12}(t,\tau) = \frac{R_{12}(t,\tau)}{\sqrt{R_{11}(t,t)R_{22}(t+\tau,t+\tau)}} \qquad \textbf{(2.13)}$$

where $R_{11}(t,t)$ and $R_{22}(t+\tau,t+\tau)$ are the autocorrelation functions (cross-correlation between a signal and itself) of signals 1 and 2, respectively. The correlation time lag, τ, which corresponds to the spatial displacement, is estimated as the position where the correlation coefficient function is at its maximum. The magnitude of $R_{12}(t,\tau)$ calculated from the analytic signal is equivalent to the envelope of the magnitude of $R_{12}(t,\tau)$ calculated from the RF signal (Fig 2.4).

After the axial displacement is initially estimated using the magnitude of the correlation function, this estimate is then refined using the phase of the correlation function produced from the analytic signal. For analytic signal correlation, the phase crosses zero at the true time delay. Mathematically, the phase of the analytic correlation function, $\phi^a(\tau)$, can be represented according to:

$$\phi^a(\tau) = \angle R_{12}(t,\tau) = \omega_0(\tau_0 - \tau) \qquad \textbf{(2.14)}$$

From equation 2.14, it is evident that at the true time delay, τ_0, the phase $\phi^a(\tau) = 0$.

Fig. 2.4 illustrates the magnitude and phase of the correlation coefficient for RF and analytic signals. Note that the phase of the analytic correlation function crosses zero at multiple locations. Thus, the magnitude of the cross-correlation function must be estimated within one-quarter wavelength of the true peak in order to identify the true phase-zero crossing [3].

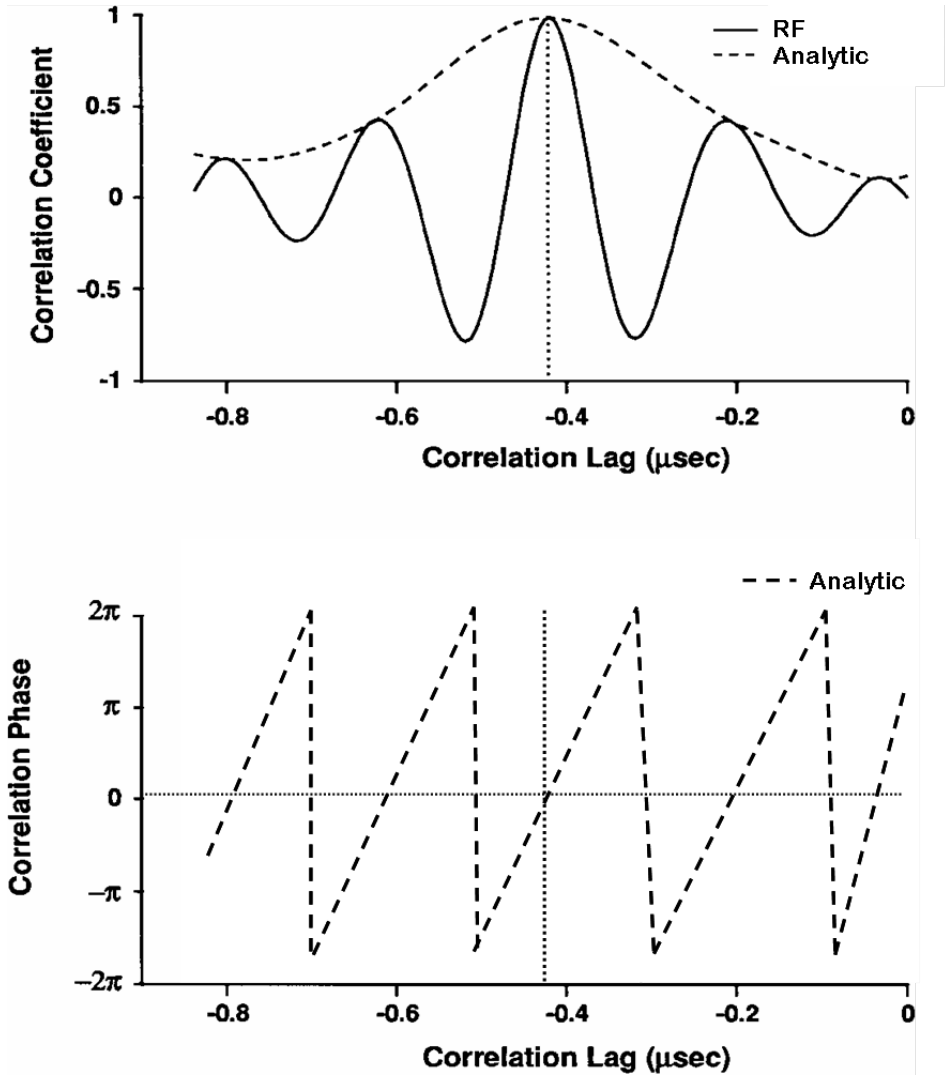

Fig 2.4: (Top) Magnitude of the cross-correlation coefficient function for RF and analytic signals. Note that the magnitude of the correlation coefficient derived from the analytic signal corresponds to the envelope of the correlation of the RF signal; the dotted line is a reminder that these signals have the same maximum. **(Bottom)** Phase of the cross-correlation function produced by analytic signals. The phase of the analytic correlation crosses zero at the true time delay. Plots are modified from [3].

The 2D and 3D speckle tracking algorithms used to process all data collected in this dissertation are an extension of these basic concepts. Specifically, a 2D or 3D kernel, again spatially equivalent to a speckle spot in each direction, is formed around each pixel in the pre- and post-deformation images. This kernel is moved laterally and axially (and elevationally, for 3D) over a "search region." In experimental practice, the deformation is applied externally and thus the induced displacement and strain are roughly known. That

initial strain guess is then incorporated into the speckle tracking algorithms to start the tracking in an area near the true displacement, reducing the region over which the algorithms must search, and, consequently, the computation time. In 2D speckle tracking, at every pixel in the search region, the 2D kernel is cross-correlated with the complex post-deformation image. The resulting unit-normalized, complex, cross-correlation coefficient function ρ'_{xy} at pixels (x, y) as a function of lags (l_x, l_y) is described in equation 2.15. In this equation, $G_t(x, y)$ is the original pre-deformation image, $G_{t+1}(x, y)$ is the post-deformation image, and W_{ij} is a 2D hamming window over the 2D correlation kernel.

$$\rho'_{xy}(l_x, l_y) = \frac{\sum_i \sum_j W_{ij}\left[G_t(x+i, y+j) G^*_{t+1}(x+l_x+i, y+l_y+j)\right]}{\left[\sum_i \sum_j W_{ij}\left|G_t(x+i, y+j)\right|^2\right]^{1/2}\left[\sum_i \sum_j W_{ij}\left|G^*_{t+1}(x+l_x+i, y+l_y+j)\right|^2\right]^{1/2}}. \quad \textbf{(2.15)}$$

To decrease noise in the correlation coefficient function, it is then low-pass filtered with a unity gain function $\left(\sum F_{ij} = 1\right)$, twice the speckle size:

$$\rho_{xy}(l_x, l_y) = \sum_i \sum_j F_{ij}\left[\rho'_{x+i, y+j}(l_x, l_y)\right], \quad \textbf{(2.16)}$$

There is a linear tradeoff between spatial resolution and strain SNR as a function of filter size [3]. Increasing filter size reduces peakhop errors (discussed in section 2.4.3) by reducing correlation error variance, and increasing strain SNR [3]. However, too large of a filter will reduce spatial resolution in the final strain images and will counteract the benefits of reduced variance from smaller correlation kernels [3].

This process in 3D dimensions is a natural extension of the 2D version:

$$\rho'_{xyz}(l_x, l_y, l_z) =$$

(2.17)

$$\frac{\sum_i \sum_j \sum_h W_{ijh}\left[G_t(x+i, y+j, z+h) G^*_{t+1}(x+l_x+i, y+l_y+j, z+l_z+h)\right]}{\left[\sum_i \sum_j \sum_h W_{ijh}\left|G_t(x+i, y+j, z+h)\right|^2\right]^{1/2}\left[\sum_i \sum_j \sum_h W_{ijh}\left|G^*_{t+1}(x+l_x+i, y+l_y+j, z+l_z+h)\right|^2\right]^{1/2}}$$

.

and

$$\rho_{xyz}(l_x, l_y, l_z) = \sum_i \sum_j \sum_h F_{ijh}\left[\rho'_{x+i, y+j, z+h}(l_x, l_y, l_z)\right] \quad \textbf{(2.18)}$$

From these equations, the integer displacements u, v (and w) (corresponding to lateral, axial, and elevational directions) are determined from the maximum of the magnitude ρ. Because ρ is a discrete function, a 2D 2nd (and 3D 3rd) order polynomial is fit to the function. Sub-pixel accuracy of the displacements is then achieved by interpolating the polynomial over a 3x3(x3) pixel region centered at u, v (and w). Because phase information from the correlation function is only available in the axial direction, only the axial displacement estimates are then further refined using the phase zero-crossing. Specifically, over a small region, the phase of the analytic signal can be expressed as a linear function within the region of the correlation peak, and thus over a 3 pixel region, simple linear interpolation is used to find the location where it crosses zero. The final outputs of the 2D processing are the lateral displacement $u(x, y)$, axial displacement $v(x, y)$, and magnitude of the correlation coefficient $|\rho(x, y)|$. Analogously, in 3D, these outputs are the axial displacement $v(x, y, z)$, lateral displacement $u(x, y, z)$, elevational displacement $w(x, y, z)$, and magnitude of the correlation coefficient $|\rho(x, y, z)|$.

2.3.2. Calculation of Strain from Displacement Estimates

Elastic Young's modulus and shear modulus values between different tissue types, as well as tissue abnormalities, differ by many orders of magnitude [24]. No imaging modalities (including ultrasound, NMR, and computed tomography) can directly provide information regarding elasticity of tissue. However, the elastic properties of tissue describe its deformation in response to applied forces. Thus, the components of the strain tensor can be approximated from derivatives of the displacements measured by speckle tracking (equation 2.19):

$$\varepsilon = \begin{bmatrix} \varepsilon_{xx} & \varepsilon_{xy} & \varepsilon_{xz} \\ \varepsilon_{yx} & \varepsilon_{yy} & \varepsilon_{yz} \\ \varepsilon_{zx} & \varepsilon_{zy} & \varepsilon_{zz} \end{bmatrix} \quad \textbf{(2.19)}$$

In this equation, *x* corresponds to the lateral (perpendicular to propagation) direction, *y* is the axial (along the beam and in the direction of compression) direction, and *z* is orthogonal to the ultrasound imaging plane, which is often called the "out-of-plane" direction. The shear tensor components from equation 2.19 are symmetric, such that:

$$\varepsilon_{xy} = \varepsilon_{yx} = \frac{1}{2}\left(\frac{\partial u}{\partial y} + \frac{\partial \upsilon}{\partial x}\right) \quad \textbf{(2.20)}$$

Note that the vertical, longitudinal component of the 2nd ranked strain tensor is the spatial derivative of the axial displacement with respect to axial distance (equation 2.21). This component of the strain tensor is most often displayed in strain images, including all strain images created in this dissertation.

$$\varepsilon_{yy} = \frac{\partial v}{\partial y} \tag{2.21}$$

Though the term “elastogram” can be used to describe any elastic characteristic in tissue, in this dissertation it will refer solely to the axial strain image.

In practice, the axial normal strain estimates are computed from axial displacements using a 1D difference filter:

$$\varepsilon_{yy}[n] = \frac{v[n - ws] - v[n + ws]}{ws} \tag{2.22}$$

where *v* is the axial displacement with units of range samples, and *ws* is the window size, or filter size, used during speckle tracking. Because deformations are tracked over a small window, corresponding to the speckle size, measured displacements are linear over this region and thus resulting strains can be derived from this simple difference filter. From equations 2.21 and 2.22 it is evident that displacement errors must be minimized because they will be amplified by the spatial derivative operation.

2.3.3. Estimation Artifacts and Limitations

When using phase-sensitive correlation-based speckle tracking to measure displacements and estimate spatial derivatives, there are several tradeoffs which must be considered to create high quality final images.

One metric of estimation error is the strain SNR:

$$SNR_{\varepsilon} = \frac{E[\varepsilon]}{\sigma_{\varepsilon}} \tag{2.23}$$

where ε is the component of the strain tensor, $E[\varepsilon]$ is the mean strain, and σ_{ε} is the variance of the strain estimates.

Assuming that motion is uniform in a speckle generating object like tissue, then estimation errors are controlled primarily by the SNR, bandwidth, and the carrier frequency of the ultrasound system. If applied displacements result in small strains, these are the factors which dominate SNR in resulting elastograms. However, if the applied displacements are too large, then scatterers move in and out of the plane and cannot be tracked. If strains are too large, then the spatial distribution of scatterers used for tracking significantly change, decorrelating the speckle patterns required for tracking. In both of these instances, substantial decorrelation occurs, increasing the errors in displacement estimation and in the strain derived from those displacements. The relationship between strain SNR and strain magnitude is illustrated in Fig. 2.5. Clearly, there is an optimal compression range over which strain images should be created in order to produce the greatest SNR_ε.

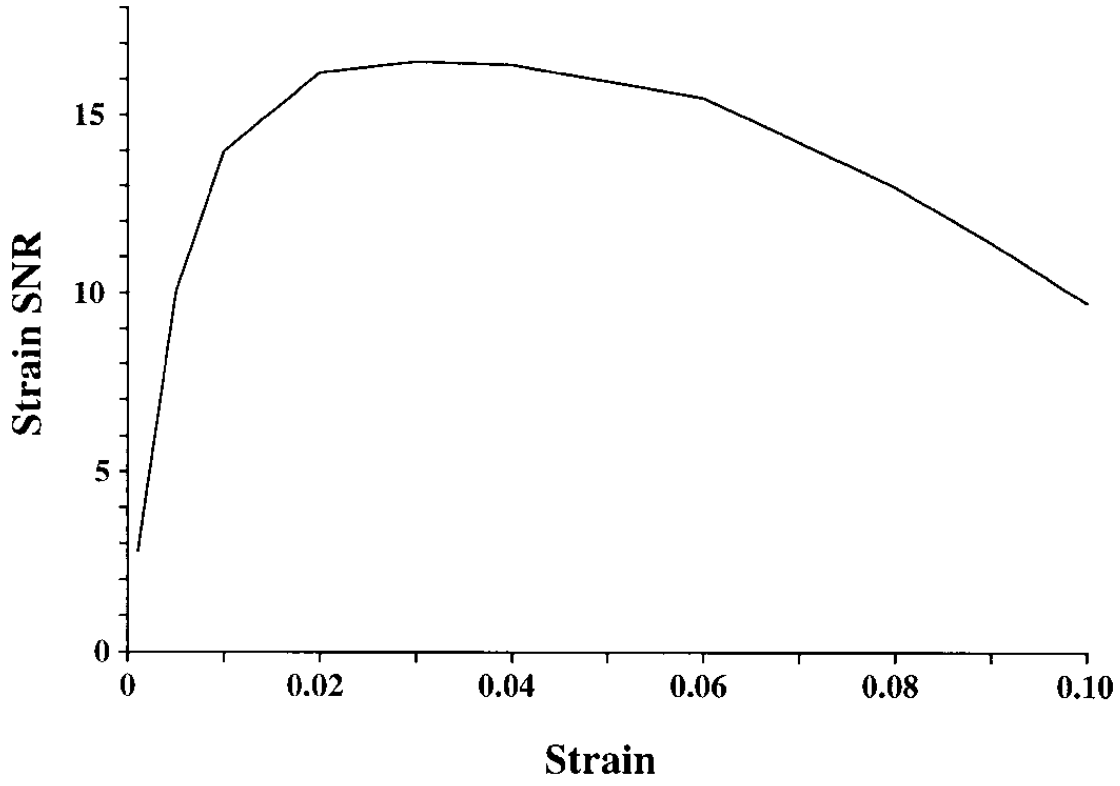

Fig. 2.5: Strain SNR as a function of strain magnitude, obtained from a 1D simulation in [23]. At low strains, SNR is limited by the characteristics of the ultrasound system and at high strains, SNR is limited by decorrelation from the speckle tracking estimates. In practice, deformation should be controlled in order to obtain strains within these limits so high quality strain images can be produced.

To achieve high strain SNR while reducing uncorrelated errors in the displacement estimates, multi-compression steps are induced in smaller increments, and then summed over the entire deformation range, a process called "accumulation" [1, 24]. In accumulation, displacement estimates are bilinear interpolated to the same geometry of the initial B-mode ultrasound image, and then the resulting displacements are summed to create a final displacement estimate over the entire deformation range. This produces strain SNRs that are nearly as high as if they were created from a single-compression step, but without the additional decorrelation observed at high strains or created from displacement-related decorrelation (such as of out-of-plane motion).

Recall that only the axial normal strain images will be presented in this dissertation. This is because lateral resolution in ultrasound images is limited by the beamwidth of the system whereas axial resolution is limited by the system Q and transducer frequency [28]. The accuracy of lateral displacement estimates cannot be improved using phase-zero crossings, as they can in the axial direction, because there is no lateral carrier frequency. Thus, the accuracy of 2D displacement estimates is much lower in the lateral direction than in the axial direction [29]. Displacement variance can be approximately quantified from an analysis of correlation errors [30]. Assuming measurement noise is white, additive, and small with respect to the signal, and the powers of the two signals being correlated is the same, then the variance of the fluctuation of the peak position of the cross-correlation function, *R*, can be described as [30]:

$$\sigma_R^2 = \frac{4\pi}{W}\frac{1}{SNR} \qquad \textbf{(2.24)}$$

where W is the normalized second moment of the signal power spectrum. In the axial and lateral directions, W is described as:

$$W_{axial} = \left(\frac{4\pi}{\lambda}\right)^2 \left(1 + \frac{BW^2}{8\ln(2)}\right) \quad \textbf{(2.25)}$$

$$W_{lateral} = \frac{1}{10}\left(\frac{2\pi}{\lambda * fnum}\right)^2 \quad \textbf{(2.26)}$$

In equations 2.25 and 2.26, BW is the bandwidth of the system, λ is the wavelength, and $fnum$ is the F-number of the transducer. Assuming SNRs are the same in each direction, the relative variance of the lateral to axial displacement estimates is:

$$\frac{\sigma^2_{R,lateral}}{\sigma^2_{R,axial}} = 40(fnum)^2\left[1 + \frac{BW^2}{8\ln(2)}\right] \approx 40(fnum)^2 \quad \textbf{(2.27)}$$

If the fractional bandwidth of the system is 40% then the term in the brackets is 1.03, so the variance of lateral displacement estimates is approximately $40(fnum)^2$ greater than that of axial [30]. The f-number of an ultrasound system is the ratio of depth to lateral aperture size and is a measure of lateral resolution: the lower the f-number, the greater the lateral resolution. For the 10L transducer at 7.5 MHz used for many experiments in this study, the f-number is 1.1. Thus, it is evident that lateral normal strain images are currently too noisy to extract information from.

The most common artifact observed in axial strain images are “peakhops”. Peakhopping occurs when the correlation search finds a false peak that is larger than the true one and thus “hops” to that peak [3]. The way peakhopping integrates itself into axial displacement and axial strain images is depicted in Fig. 2.6, which was created using a 7.5 MHz transducer in a tissue-mimicking phantom with fully-developed speckle using a strain step size of 1.4%. The likelihood of peakhopping can be reduced by spatially

filtering the correlation coefficient functions before displacement estimation and keeping induced strains from being so large that significant decorrelation occurs. However, these efforts will not eliminate the presence of all peakhops which, when present, can obstruct visibility in strain images.

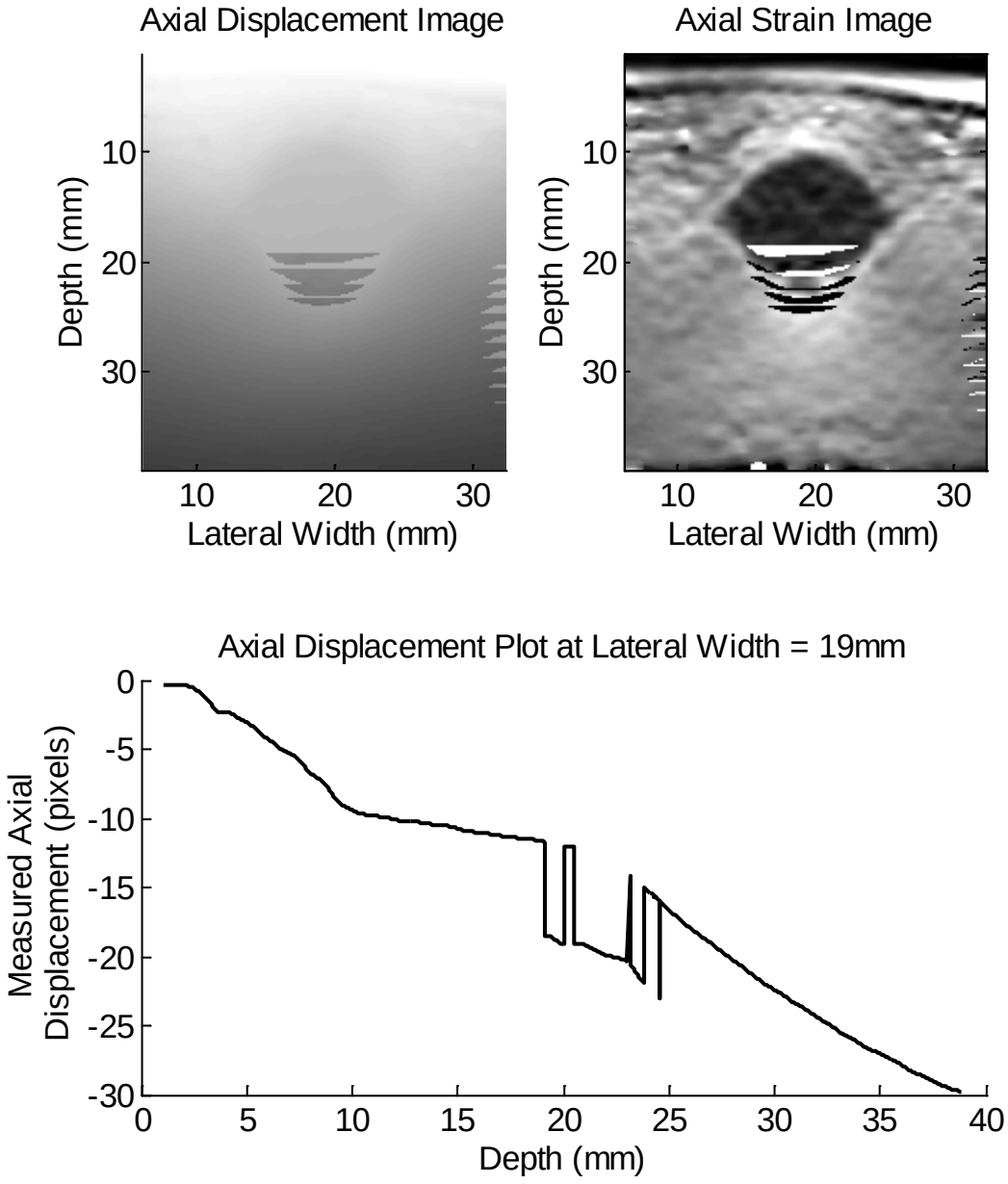

Fig. 2.6: (Top, left) Axial displacement image with peakhops created from a tissue mimicking phantom imaged at 7.5 MHz over a 4 cm depth. **(Top, right)** Resulting axial strain image (mean strain = 1.4%). The peakhop artifacts in the inclusion exhibit both white and black streaks. **(Bottom)** Axial displacement plot through the center of the axial displacement image. Jumps in the axial displacement values (peakhops)

between 19-25 mm depth correspond to the streaks observed in both the axial displacement and axial strain images.

Another important limitation of this technique is that data acquisition must be conducted within a breathold. If elasticity data can be collected over a patient breathold, then motion artifacts will be minimized [1]. Additionally, long-time constant processes such as strain relaxation and creep are not significant over this period [30].

A block diagram of the process of creating the final elastogram from the original IQ data obtained from the GE LOGIQ 9 scanner used in experiment conducted in this dissertation is shown in Fig. 2.7. Before inputting the compression data into the speckle tracking algorithms, the data must be basebanded and upsampled from a 10 MHz sampling frequency to a 40 MHz sampling frequency. To reduce errors due to boundary conditions, edges of the image are cutoff in each direction and the final image is 3.8 cm (axially) x 2.6 (laterally).

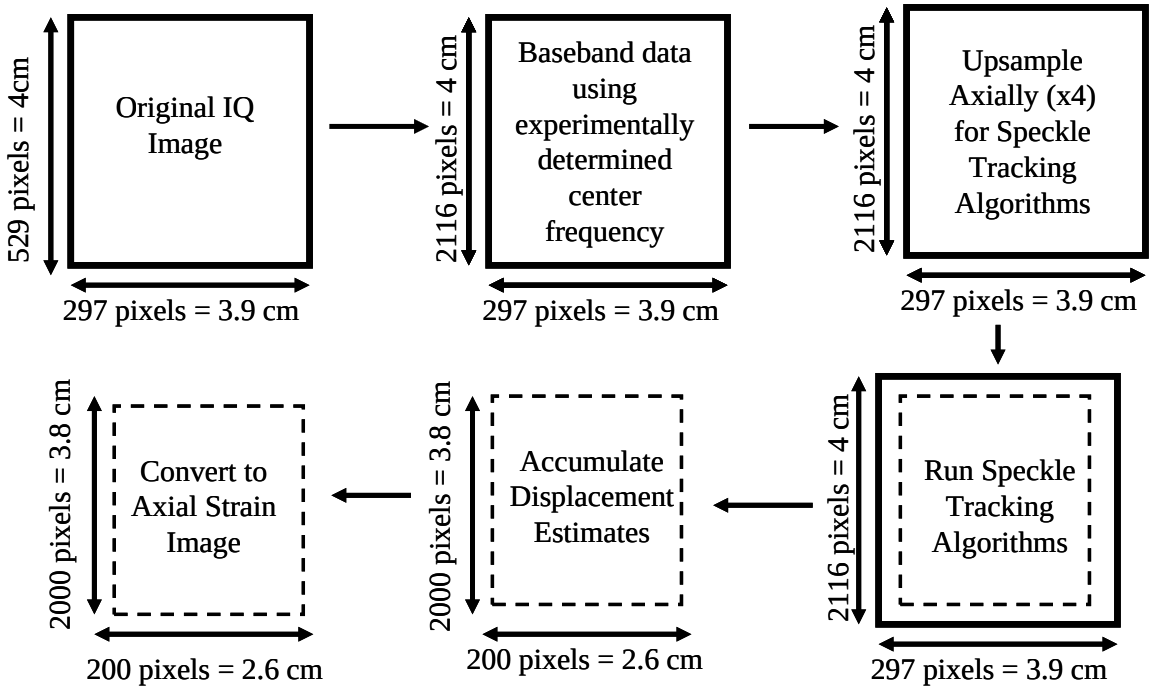

Fig. 2.7: Block diagram of process used in this dissertation to create elastograms from initial IQ data.

2.3.4. Reconstruction of Elastic Modulus

When tissue deformation in response to applied forces is accurately measured, the elastic properties of the tissue can be reconstructed using a mechanical model which relates stress and strain. Images of a material's reconstructed mechanical properties are expected to contain fewer artifacts than strain images alone and an absolute measure of material properties may be an important indicator of a tissue's pathology [31].

Because elastic modulus reconstructions use the deformations estimated in elastography, these estimates must have a high SNR for the reconstructions to be accurate [31]. Additionally, the type of mechanical model used for reconstruction will determine which deformation measurements are needed for its assumptions to hold. For example, a common reconstruction technique uses a linear elastic, isotropic, incompressible model to determine the tissue's Young's modulus [31]. If a plane strain or plane stress model is used, then it would require tissue displacement measurements from a 2D vector field on a plane of the tissue [32]. The assumptions made in [32] are common assumptions when 2D ultrasound data is used for displacement measurements. Although this assumption may remove many strain artifacts caused by boundary effects [31], a purely plane strain or plane stress relation is rarely realized in most 3D tissue structures.

It is expected that a full 3D linear elastic, isotropic, incompressible material assumption and thus a full 3D vector field of a tissue's volume would more accurately represent its stress-strain relation. However, because 3D elastography is currently in its infancy, the efficacy of this reconstruction method is limited. The work presented in this dissertation will focus on the feasibility and utility of 2D and 3D breast elastography conducted through a mammographic paddle in conjunction with a combined

ultrasound/digital tomosynthesis mammography unit. Until these techniques are fully developed and can produce high quality elastograms, the full utility from reconstructing the elastic modulus may not be realized. Therefore, reconstructing the elastic modulus is beyond the scope of this dissertation, but the work presented in the following chapters may pave the way for full tissue reconstructions to be conducted in the future.

2.4. Conclusions

Because speckle is an inherent feature in ultrasound images and provides the fundamental theoretical framework for elastography, an understanding of its behavior is essential. Speckle is created from the constructive and destructive interference of echoes which are complex summed across a transducer aperture and, when fully-developed, can be described using correlation-based techniques. In elastography, the response of the tissue to applied deformations is measured using time-delay techniques and correlation-based processing analyzed over the spatially equivalent distance of one speckle spot. The resulting axial displacement estimates are converted into strain images, which must contain high SNR in order to provide meaningful information about the elasticity of the tissue. In order to fully characterize tissue, the elastic modulus should be reconstructed, however, that is beyond the scope of this dissertation. Efforts to conduct elasticity through a mammographic paddle and use the resulting elastograms to characterize breast lesions are the focus of the remainder of this dissertation.

2.5. References

[1] O'Donnell M, Skovoroda AR, Shapo BM, Emelianov SY. Internal displacement and strain imaging using ultrasonic speckle tracking. IEEE Trans Ultrason, Ferroelectr Freq Contr 1994; 41(3): 314-325.

[2] Ophir J, Cespedes I, Ponnekanti H, Yazdi Y, Li X. Elastography: a quantitative method for imaging the elasticity of biological tissues. Ultrasonic Imag 1991; 13: 111-134.

[3] Lubinski MA, Emelianov SY, O'Donnell M. Speckle tracking methods for ultrasonic elasticity imaging using short-time correlation. IEEE Trans Ultrason Ferroelectr Freq Control 1999; 46: 82-96.

[4] Kaluzynski K, Chen X, Emelianov SY, Skovoroda AR, O'Donnell M. Strain rate imaging using two-dimensional speckle tracking. IEEE Trans Ultrason Ferroelectr Freq Control 2001; 48: 1111-1123.

[5] Chen X, Xie H, Erkamp R, et al. 3-D correlation-based speckle tracking. Ultrason Imaging 2005; 27(1): 21-36.

[6] Knapp CH, Carter GC. The generalized correlation method for estimation of time delay. IEEE Trans Acoust, Speech, Signal Proc 1976; 24(4): 320-327.

[7] Dantas, RG, Costa ET, Leeman S. Ultrasound speckle and equivalent scatterers. Ultrasonics 2005; 43: 405-420.

[8] Wells PNT, Halliwell M. Speckle in ultrasonic imaging. Ultrasonics 1981; 19: 225-229.

[9] Wagner RF, Smith SW, Sandrik JM, Lopez H. Statistics of speckle in ultrasound B-scans, IEEE Trans Sonics Ultrasonics 1983; 30: 156-163.

[10] Abbott JG, Thurstone FL. Acoustic speckle: theory and experimental analysis. Ultrason Imaging 1979; 1: 303-324.

[11] Tuthill TA, Sperry RH, Parker KJ. Deviations from Rayleigh statistics in ultrasonic speckle. Ultrasonic Imaging 1988; 10: 81-89.

[12] Smith SW, Wagner RF. Ultrasound speckle size and lesion signal to noise ratio: verification of theory. Ultrason Imaging 1984; 6: 174-180.

[13] Thijssen JM, Oosterveld BJ. Speckle and texture in echography: artifact or information? IEEE Ultrasonics Symposium 1986; 803-809.

[14] Burckhardt CB. Speckle in ultrasound B-mode scans. IEEE Trans. Sonics Ultrasonics. 25, 1-6 (1978).

[15] Trahey, GE, Allison JW, Smith SW, and von Ramm OT. Speckle pattern changes with varying acoustic frequency: experimental measurement and implications for frequency compounding. IEEE Ultrasonics Symposium, 815-818 (1986).

[16] Trahey GE, Smith SW, and von Ramm, OT. Speckle pattern correlation with lateral aperture translation: experimental results and implications for spatial compounding. IEEE Trans. Ultrasonics, Ferroelectrics, and Frequency Control. UFFC-33, 257-264 (1986).

[17] Szabo, T. Diagnostic Imaging, Inside Out. Elsevier Academic Press: Burlington, MA, 2004.

[18] Ophir, J, Alam KA, Garra B. Elastography: ultrasonic estimation and imaging of the elastic properties of tissues. J Eng Med 1999; 213: 314-325.

[19] Tuthill, TA, Krucker, JF, Fowlkes JB, Carson PL. Automated three-dimension US frame positioning computed from elevational speckle decorrelation. Radiology 1998; 209: 575-582.

[20] Lizzi FL, Greenebaum M, Feleppa EJ, Elbaum M. Theoretical framework for spectrum analysis in ultrasonic tissue characterization. J of Acoust Soc of Am 1983; 73: 1366-1373.

[21] Varghese T, Donohue KD. Characterization of tissue microstructure scatterer distribution with spectral correlation. Ultrason Imaging 1993; 15: 238-254.

[22] Special issue on time delay estimation. IEEE Trans. Acous., Speech, Signal Processing. 29(3); 1981.

[23] Lubinski MA, Emelianov SY, O'Donnell M. Adaptive strain estimation using retrospective processing. IEEE Trans Ultrason Ferroelectr Freq Control 1999; 46: 97-107.

[24] O'Donnell M, Emelianov SY, Skovoroda AR, Lubinski MA, Weitzel WF, Wiggins RC. Quantitative elasticity imaging. Proc. IEEE Ultras Symp 1993; 893-903.

[25] Nightingale KR, Kornguth PJ, and Trahey GE. The use of acoustic streaming in breast lesion diagnosis: a clinical study. Ultrasound Med Biol 1999; 25:75-87.

[26] Mailloux, GE, Bleau A, Bertrand M, Petitclerc R. Computer analysis of heart motion from two-dimensional echocardiograms. IEEE Trans Biomed Eng 1987; 34(5): 356-364.

[27] O'Donnell M, Skovoroda AR, Shapo BM. Measurement of arterial wall motion using Fourier based speckle tracking algorithms. Proc IEEE Ultrason Symp 1991; 1101-1104.

[28] Hein IA and O'Brien WD. Current time-domain methods for assessing tissue motion by analysis from reflected echoes – a review. IEEE Trans. Ultrason. Ferroelectr. Freq. Contr. 1993; 40(2): 84-102.

[29] Bohs LN and Trahey GE. A novel method for angle independent imaging of blood flow and tissue motion. IEEE Trans Biomed Eng, 38(3): 290-296.; 1991.

[30] Lubinski MA, Emelianov SY, Raghavan KR, Yagle AE, Skovoroda AR, O'Donnell M. Lateral displacement imaging using tissue incompressibility. IEEE Trans Ultrason Ferroelectr Freq Control 1996; 43(2): 247-256.

[31] Skovoroda, AR, Emelianov SY, O'Donnell M. Tissue elasticity reconstruction based on ultrasonic displacement and strain images IEEE Trans Ultrason Ferroelectr Freq Control 42(4): 747-765; 1995.

[32] Barbone PE and Bamber JC. Quantitative elasticity imaging: what can and cannot be inferred from strain images. Phys Med Biol 2002; 47(12): 2147-2164.

CHAPTER 3

EVALUATING THIN COMPRESSION PADDLES FOR MAMMOGRAPHICALLY COMPATIBLE ULTRASOUND

3.1. Chapter Overview

This chapter examines the effects of sonographic imaging through mammographic paddles of different materials and thicknesses to determine the most acoustically suitable paddle for a combined ultrasound/tomosynthesis system. Imaging through a plastic paddle could have adverse effects on ultrasound image quality, including beam widening in all 3 directions, increased attenuation, decreased contrast, increased sidelobes, and increased reverberations. The effects of various paddles on these aspects of image quality are quantified and compared. Furthermore, the roles of acoustic coupling, breast stabilization, and imaging access to all areas of the breast are highlighted for this system. After the most suitable paddle(s) are determined, initial clinical results are presented to demonstrate that the minor losses of image quality with this system should not have clinical impact when coupling and coverage issues are minimized. Finally, the implications of through-paddle ultrasound on elastography with this system are discussed.

The work presented in this chapter has been published in [25] and [26].

3.2. Introduction

Breast ultrasound examinations are currently performed free-hand by a radiologist or a technician as a supplement to mammography when lesions are radiographically suspicious or indeterminate. These ultrasound images correspond to a different imaging geometry than the mammograms and, at least 10% of the time, there is a discrepancy between the lesions detected with the two modalities [1]. A combined x-ray/ultrasound system essentially eliminates this problem by first taking a digital x-ray over a compressed breast, then scanning a high frequency (9-12 MHz) ultrasonic transducer across the mammographic paddle while the breast is still under compression. This creates x-ray and ultrasound images in the same imaging geometry. The resulting 3D full field-of-view ultrasound images can later be registered to the digital mammograms. Thus this method of scanning might be able to expand the utility of ultrasound breast imaging and replace some hand-held, direct-contact ultrasound.

Sonographic detection of cancer has been problematic because it has relied heavily on operator and interpreter skill and patience. False positives are a particular problem when searching for secondary masses and for detection in high risk or screening populations. When supplemental to mammography, however, ultrasound has been a valuable tool in detecting and characterizing lesions in asymptomatic high-risk women, including those with mammographically dense breasts [2-8]. Concurrent screening with these two imaging modalities using high quality equipment and performed by a skilled physician is reported to inexpensively provide high mammographic-US correlation of breast lesions and to significantly improve cancer detection [9-12].

Other systems developed for ultrasound imaging of a compressed breast through a mammographic paddle have experienced limited success [13-18]. Some of the difficulties these systems faced included highly attenuating compression paddles, substantial reverberations, lower frequency operation, weakly focused beams and image artifacts created by refractions through the paddles. By thoroughly evaluating compression paddles to find nearly ideal material(s) and thickness(es) for both mammographic and sonographic requirements, we hope to improve on these past efforts.

The goal of this chapter is to compare image quality of the combined system (automated, through-paddle scanning) with that of current practice (hand-held, direct-contact scanning). Ultrasound image quality of the combined system could be adversely affected in comparison with direct-contact ultrasound because of three key factors.

First, the compression paddle affects the point- or line-spread function (PSF or LSF) of the system by refracting and attenuating the ultrasound beam. Refraction then exacerbates reverberation artifacts. Thus, the primary focus of this study is to investigate the consequences of imaging through the paddle on the LSF, sidelobe levels, range lobes (reverberations), contrast and signal loss. Some of these effects can be partly compensated by modifying the beamforming of the ultrasound scanner [19-20]. The efficacy of such corrections and severity of remaining differences compared with direct-contact scanning are evaluated in several test object experiments and on human subjects examined with known cysts.

In addition, parallel compression paddles may introduce acoustic coupling difficulties on the sides of the breast and in the areolar region. Preliminary methods to

increase breast contact with the paddle are introduced in this study and suggestions for other techniques to improve contact are addressed.

Finally, the probe with holder restricts access to parts of the breast, such as those near the chest wall. Scanning through a paddle limits insonification angles and planes, which could impede visualization of specular surfaces and increase the possibility that shadows from Coopers ligaments obstruct other tissue visibility. Imaging at 20° or in trapezoidal mode could lessen these issues. This study did not evaluate image quality under those conditions, but initial images and are shown and addressed further in the Conclusions section.

3.3. Methods

3.3.1. Experimental Setup

Note that the experiments in this chapter were conducted before the development of the tomosynthesis unit. Thus, though the goals of the experiments were the same, slight differences exist between this setup and the one described in Chapter 1. Thus the experimental setup used for the experiments will be described here. Human subject experiments were conducted at the Cancer and Geriatric Center at the University of Michigan Medical Center on the combined system using a GE LOGIQ 9 ultrasound scanner and GE Senographe 2000D digital mammography unit (Fig. 3.1a). Test object experiments were performed on the stand-alone (ultrasound only) modified dual system developed by researchers at the University of Michigan and General Electric (GE Healthcare, Milwaukee, WI, USA). All experiments used a 1.5D M12L array transducer (length = 39 mm, focus = 1.6 cm) operating at 10 MHz. It was housed in a carriage and

attached to two motors translating it across the mammographic paddle (Fig. 3.1b). The transducer carriage was spring-loaded to ensure constant contact with the paddle. Hardware and software were developed for both systems to semi-automatically drive the transducer across the compression paddle, as well as to communicate with the LOGIQ 9 ultrasound system to trigger image and data acquisition [22].

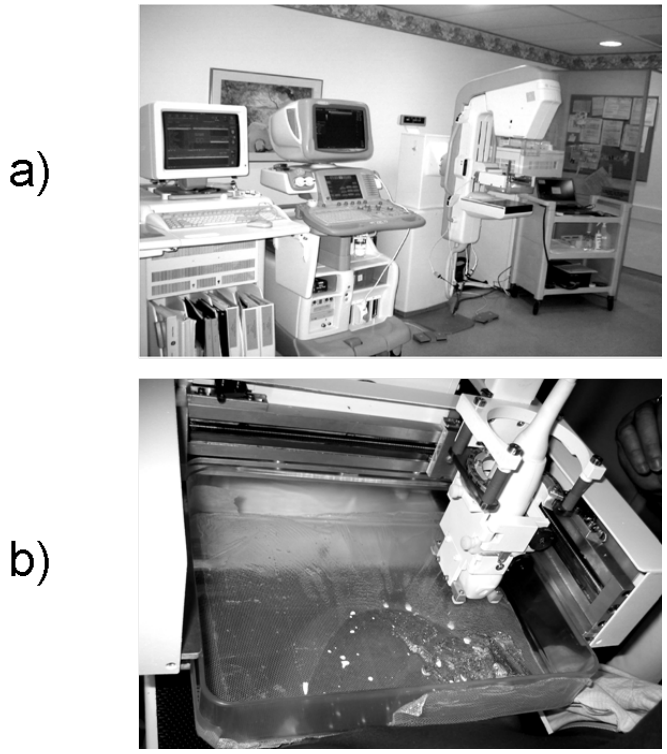

Fig. 3.1: a) Combined 3D ultrasound/ digital mammography system. From left to right are the mammogram storage unit, GE LOGIQ 9 scanner, Senographe 2000D digital mammography unit, and cart containing hardware and software to drive the combined system. **b)** Close up view of a breast compressed between the mammographic paddle and x-ray detector, with the ulrasound transducer and holder attached.

3.3.2. Choice of Mammographic Compression Paddles

Standard mammography compression paddles are 2.5 mm thick and made of lexan, a polycarbonate. However, the high level of acoustic attenuation in lexan (23.2 dB/cm at 5 MHz) precludes this standard mammographic paddle from sonographic imaging. Simply reducing paddle thickness insufficiently solves this problem, since a thin

paddle will excessively deform under the pressure required to compress the breast, resulting in a non-planar scanning surface. Another option then is to investigate alternative paddle materials with improved sonographic imaging characteristics.

Mammographic paddles used with the combined system should have favorable mechanical, x-ray, optical and acoustical properties. A paddle should be mechanically tough and rigid, bowing less than 1 cm when maximum allowed force (200 N) is applied [21]. It should be uniform mammographically and acoustically as well as relatively transparent mammographically, acoustically, and optically. The preferred paddle would have an acoustic impedance well matched with both breast tissue (~1.5 MRayl) and the transducer lens to minimize reverberations and beam refraction. These properties are further discussed in [22].

The paddle materials and thicknesses chosen for this study have a combination of the above mentioned mammographic and acoustic characteristics and are commercially available. They are: TPX (a polymethylpentene) 0.25, 0.5, 1.0 and 2.5 mm thick, lexan 125, 250 and 375 μm thick, mylar (a polyester) 250 μm thick and polyurethane 500 μm thick. Preliminary results revealed that only TPX and lexan materials were acoustically competitive for use with this system, so this report will directly compare the TPX 2.5 mm and lexan 375 μm paddles. The acoustic properties of these two materials are listed in Table 3.1.

Table 3.1: Acoustic properties of mammographic paddles.[*] [**]

Paddle	***Speed of Sound (mm/μs)***	***Attenuation (dB/cm/MHz)***	***Acoustical impedance (kg/(m^{2}s))***
TPX	2.22	1.1	1.84
Lexan	2.30	4.6	2.75

[*] Physical properties can vary substantially with the specific formulation of the polymer.
[**] Source: Onda Corporation, "Acoustic Properties of Plastics"

3.3.3. Beamforming Corrections

Most ultrasound scanners compute the electronic time delays used for focusing the ultrasound beam and scan-converting the received echo by treating tissue as a one-layer system with a fixed speed of sound (c = 1.54 mm/μs). However, the speeds of sound of most paddle materials are significantly greater than that of tissue. Thus, the propagation of the ultrasound beam through the mammographic paddle causes the beam to deviate from its assumed path, displacing it off the focus of the transducer. These aberrations can deteriorate image contrast and resolution, degrading diagnostic value. To compensate, time-delay corrections were applied to take into account the speed of sound through the mammographic paddle. Treating the paddle as an additional propagation layer with a distinct speed of sound, beam refraction occurs at the entrance and exit of the layer, behaving according to Snell's Law. Since the position of the layer is known, computation of the corresponding phase delays follows the approach described in further detail in [19]. Corrections were not implemented in the elevational direction, because their effect would be minimal due to the transducer's small aperture size and number of independent elements in that direction.

3.3.4. Test Object Experiments

Test objects were chosen to measure those aspects of image quality predicted to degrade as a result of imaging through a mammographic paddle, mainly image resolution and contrast. These test objects are described below, and were used to select preferred paddle materials and thicknesses for the combined system. These results were then confirmed *in vivo* by imaging patients with simple cysts.

A step-shaped string test object was constructed to evaluate the space-varying LSF, as shown in Fig. 3.2a. Steps were designed such that the LSF of each of the twenty 25 μm silver strings did not interfere with each other and so the LSF could be determined at a number of discrete depths from 3 - 40 mm from the transducer face. The test object was immersed in a tank of saline at body temperature ($c = 1.54$ mm/μs). Saline also provided acoustic coupling between the transducer and paddle except when the paddle was not deep enough to contain liquid, in which case ultra-myossage lotion (Chattanooga Medical Supply, Chattanooga, TN, USA) was used instead. Sound absorbing rubber surrounded the line targets to eliminate extraneous reverberations. To avoid saturation of pixel amplitudes caused by the low attenuation of saline, a preliminary experiment was conducted on the targets to determine the appropriate gain to utilize the full dynamic range without saturating.

The space-varying LSFs were measured in the lateral (along the length of the array), axial (perpendicular to the array face) and elevational (out of plane) directions. To determine lateral and axial LSFs, the test object was turned so the length of the transducer was perpendicular to the length of the strings. Lateral LSFs were constructed at each discrete depth by plotting a horizontal line through the center of each string cross-section

displayed in the resulting image. Analogously, axial LSFs were constructed at each discrete lateral position by plotting a vertical line through the center of each string cross-section. The elevational extent between the strings was too great for all of them to appear in a single image. Therefore, to obtain the elevational LSF at each discrete depth, the transducer was positioned parallel to the length of the strings and scanned in 100 μm increments over a 5 cm elevational distance. Twenty-one adjacent y-z (elevational-axial) planes were extracted from the center of this volume and the peak value over this range was selected to account for small string fluctuations in the saline. Then, the elevational LSF was constructed by plotting a horizontal line through each string in this final image.

The spatial resolution of the system was determined from the LSF using the measures of full-width at half-maximum (FWHM, -6 dB) and full-width at tenth-maximum (FWTM, -20 dB). Pixel amplitudes were log-decompressed to dB values from a log-linear grayscale map according to the equation for the "E" grayscale curve setting on the scanner:

$$Y = \left[20\log_{10}(X+1)\right] * \frac{255}{DR}, \qquad \textbf{(3.1)}$$

where the first half of the equation converts pixel amplitude, *X*, to dB and the second half of the equation scales these dB values by the number of gray scale levels (255) divided by the dynamic range (DR), 72 dB, in all experiments. This high DR was chosen to accommodate the large differences in signal level seen in breasts, from anechoic cysts to bright glandular tissue.

Main sidelobe levels and range lobe amplitudes, which include all reverberations, relative to maximum signal were calculated in the elevational and axial directions, respectively. Errors due to electronic noise were minimized by fitting these values to

spatial polynomials of appropriate degrees. Each paddle's axial and lateral LSF was measured with and without beamforming corrections.

To measure contrast, a contrast-detail test object (Computerized Imaging Reference Systems (CIRS), Norfolk, VA, USA, Model 47) was imaged. This object contained an anechoic cylinder which was angled along the length of the test object relative to the transducer. To simulate a small simple cyst occurring at a range of depths, the transducer was translated over this object for 80 mm in step sizes of 500 μm. The contrast between the circular cross-section of the cylinder (diameter = 2.4 mm) and the test object background was the calculated as a function of depth. In each acquired image, the center of the cylinder was manually identified and then three circles with radii 1.2 mm, 2.2 mm and 4.2 mm were drawn from that center, as shown in Fig. 3.2b. The mean amplitude in the anechoic cylinder was calculated in the innermost circle. The mean amplitude of the background was calculated in the area defined between the two outer circles. The final contrast was then the difference between these two means. The gain was raised so the mean value of the signal in the anechoic cylinder was greater than zero.

Signal strength measurements were also made using the contrast detail test object. A uniform speckle region in the test object was averaged at each range sample location to determine signal strength through the paddles, with and without beamforming correction factors, relative to signal strength with no paddle. A fourth degree-polynomial fit was applied as a function of depth to reduce errors caused by noise.

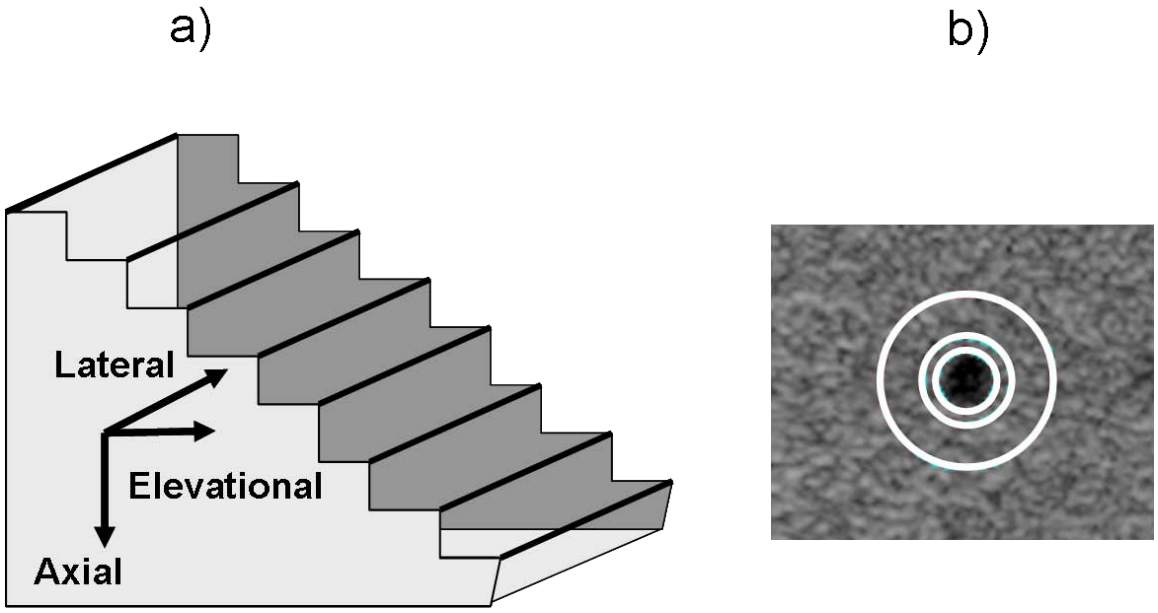

Fig. 3.2: a) Step-shaped string test object with 25 μm silver wires acting as line targets to assess the LSF of the system in all three directions. **b)** Anechoic cylinder within contrast test object for determining contrast with and without imaging through a mammographic paddle. Mean cylinder amplitude was calculated within the innermost white circle and mean background amplitude was calculated in the area between the two outermost white circles. Mean signal strength for each paddle and no paddle was also calculated from a uniform speckle region within this phantom over a 4 cm depth.

3.3.5. Human Subject Scans

Informed consent was obtained using a protocol and other procedures that were approved by the University of Michigan Institutional Review Board. Women recruited for this study had clinically confirmed simple cysts. Strongly hypoechoic cysts were chosen for this study because they allowed quantitative and subjective measurements of ultrasound image quality losses due to the mammographic paddles that would affect detection and diagnosis of more complex solid masses.

To maximize comfort and minimize human subject motion during clinical scans, subjects were seated while the mammogram and ultrasound images were acquired. At the beginning of the procedure, a radiologist conducted a hand-held, direct-contact ultrasound scan across the breast to verify the region-of-interest (ROI) and determine the

appropriate imaging view (cranial-caudal (CC), medial-lateral (ML), or mediolateral-oblique (MLO)). An acoustic coupling material was then placed between the transducer and paddle, and another was placed between the paddle and breast. Coupling between the transducer and paddle was achieved using water (contained in the paddle if the scan was in the CC view) or ultrasound gel (for LM/ML or LMO/MLO views). The appropriate acoustic coupling material between the paddle and breast must prevent breast slippage (measured by subtracting an image taken at the end of the procedure from one taken at the beginning over the same plane) without creating bubbles or extra attenuation compared to traditional coupling aids. Based on these requirements, mineral oil, ultra-myossage lotion, glycerin and "sticky" primrose oil were individually tested for preliminary evaluation. The success of these and other coupling materials was quantified and discussed in a separate study [24].

After coupling materials were applied, the subject's breast was compressed by the combined system and a foam wedge or a soft mammopad was placed underneath it to lift up the areolar region to improve anterior breast contact with the paddle. The transducer was then translated over the paddle and breast to obtain a whole breast volume. Afterwards, the ultrasound scan, the transducer, its carriage, and the coupling medium were removed from the compression paddle and a mammogram was taken. An appropriate filter was added to the mammography unit prior to imaging to account for differences in x-ray dose absorption between the tested paddle and the standard mammography paddle.

Contrast and CNR between tissue and cyst signal levels were calculated for each of the 10 human subjects scanned in this study using the equation:

$$CNR = \frac{\mu_{cyst} - \mu_{background}}{\sqrt{\sigma_{cyst}^2 + \sigma_{background}^2}} \approx \frac{contrast}{\sigma_{background}} \quad \textbf{(3.2)}$$

Based on the results from the test object experiments, human subject scans were performed through TPX 0.25 mm, 1.0 mm, or 2.5 mm paddles. System settings were adjusted to provide the clearest cyst images in the direct-contact ultrasound scan. The system gain was then increased to raise cyst signal level above zero to avoid underestimation of contrast between the background and the cyst. This did not change contrast measurements, however, because a linear grayscale map was used in all experiments. Additionally, saturation of the surrounding tissue signal was prevented by using a 72 dB display dynamic range. Gain was further increased between direct-contact and through-paddle scans to compensate for average signal loss through the paddle over the 4 cm depth, as determined by the test object experiments. Signal in the cyst ROI to within 1 mm of the cyst's edge was compared with signal from ROIs in adjacent fat and glandular tissue, for both through-paddle and direct-contact scans. Log-decompressed signals were averaged over five slices in the ROIs.

Two radiologists evaluated the differences in clinical automated and hand scans in terms of overall image quality, ease of lesion detectability and relative image quality.

3.4. Results and Discussion

3.4.1. Spatial Resolution

Mean FWHM and FWTM values were calculated over a 4 cm depth range for each direction, with and without a paddle.

One exemplary plot of the elevational LSF is shown in Fig. 3.3a. Mean FWHM values in the elevational direction for no paddle, TPX 2.5 mm paddle and lexan 375 μm paddle were 0.90 +/- 0.17 mm, 1.05 +/- 0.18 mm and 0.99 +/- 0.18 mm, respectively. Note that these values are within one standard deviation of each other and of no paddle values. Mean FWTM values were 2.10 +/- 1.0 mm, 2.56 +/- 1.2 mm and 2.18 +/- 1.1 mm, respectively. Mean sidelobe levels were calculated for each of the paddles relative to maximum signal level. With no paddle, the mean sidelobe level was -19.4 dB. Sidelobe levels were moderately elevated by paddles, with TPX performing slightly better than lexan (-16.2 dB and -15.3 dB, respectively). Defocusing due to refraction and reverberations in the paddle caused image quality losses in the elevational direction.

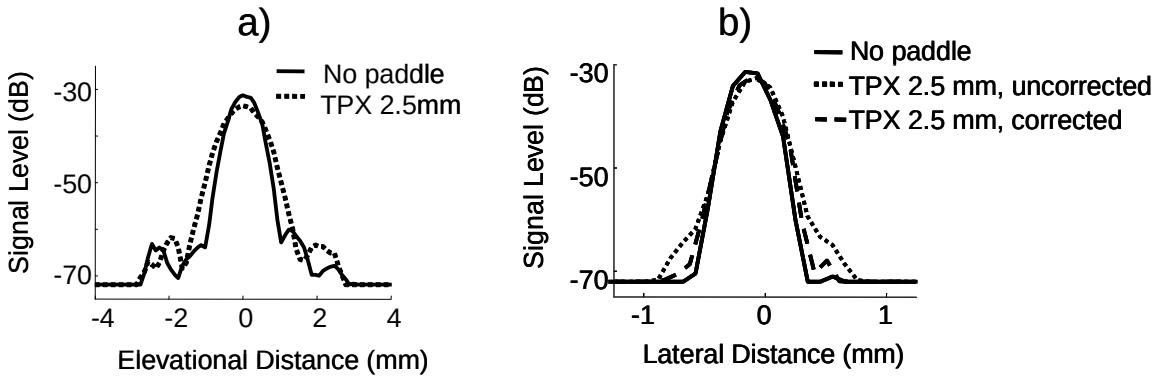

Fig. 3.3: Representative **a)** elevational LSF and **b)** lateral LSF for no paddle and TPX 2.5 mm paddle. Lexan 375 μm paddle LSFs exhibited similar shapes to no paddle LSFs. Lateral LSF was calculated with and without beamforming corrections. In the elevational direction, FWHM values were increased up to 17% and sidelobe levels were increased up to 4 dB when imaging through a paddle. FWHM values in the lateral direction were only increased 2% in both paddles when beamforming corrections were implemented.

Lengthening of the LSF as the beam travels through the paddle was inevitable, but could be reduced by implementing beamforming corrections. The improvement of image quality due to these corrections was most notable in the lateral direction. Fig. 3b shows the lengthening of the LSF due to the TPX 2.5 mm paddle and its subsequent shortening when the corrections were applied.

Mean lateral FWHM and FWTM values for no paddle, TPX 2.5 mm and lexan 375 μm paddles without corrections were 0.39 ± 0.04 mm, 0.41 ± 0.04 mm and 0.41 ± 0.04 mm, respectively, and 0.70 ± 0.07 mm, 0.75 ± 0.09 mm and 0.90 ± 0.14 mm, respectively. A student t-test revealed that even without beamforming corrections, the differences in FWHM were not statistically significant, though the differences in FWTM were. With corrections, the TPX 2.5 mm and lexan 375 μm mean FHWM and FWTM values reduced to 0.40 ± 0.02 mm and 0.40 ± 0.03 mm, and 0.72 ± 0.04 and 0.81 ± 0.12 mm, respectively. Thus, the addition of the TPX and lexan paddles only caused a 5% increase in lateral FWHM values, which was reduced to a 2% increase after beamforming corrections were implemented. Lateral FWTM values increased 28.5% due to the lexan paddle but only 7% due to the TPX paddle without corrections, and to 17% and 3%, respectively, with corrections.

Pulse lengthening due to the paddle was practically negligible in the axial direction and, thus, beamforming correction improvements in this direction were also negligible (Fig. 3.4a). Before correction algorithms were implemented, no paddle, TPX 2.5 mm paddle and lexan 375 μm paddle mean FWHM and FWTM values were 0.23 ± 0.03 mm, 0.23 ± 0.03 mm and 0.25 ± 0.03 mm, respectively and 0.48 ± 0.04 mm, 0.48 ± 0.04 mm and 0.55 ± 0.04 mm, respectively. After beamforming corrections were applied, TPX 2.5 mm paddle and lexan 375 μm paddle mean FWHM and FWTM values reduced to 0.22 ± 0.02 mm and 0.24 ± 0.02 mm and 0.46 ± 0.02 mm and 0.54 ± 0.03 mm, respectively.

In the axial direction, the addition of substantial range lobes can significantly degrade an image. As range lobes increase, they affect the main lobe, degrading

resolution. When no paddle was present, the impulse response of the transducer produced range lobes -39 ± 3.1 dB from the signal maximum, averaged over 1.5 to 3.2 cm depths. They were visibly increased with the lexan paddle (-29 ± 5.2 dB) and marginally increased by the TPX paddle (-37 ± 4.9 dB) when beamforming corrections were not implemented (Fig. 3.4b). The high range lobe levels of the lexan paddle were caused by its high impedance mismatch with saline (z = 1.48 kg/m^2s). Implementation of beamforming corrections reduced TPX range lobes to -40 ± 3.5 dB and lexan range lobes to -30 ± 3.3 dB. No signal difference was observed between paddles and no paddle beyond 2 mm of the main signal lobe, confirming that all reverberations were included in the range lobe response. Because both paddles exhibit range lobe levels 30 dB down from signal maximum, range lobes should not be a major concern for this system.

All LSF measurements, with beamforming corrections implemented where relevant, are summarized in Table 3.2.

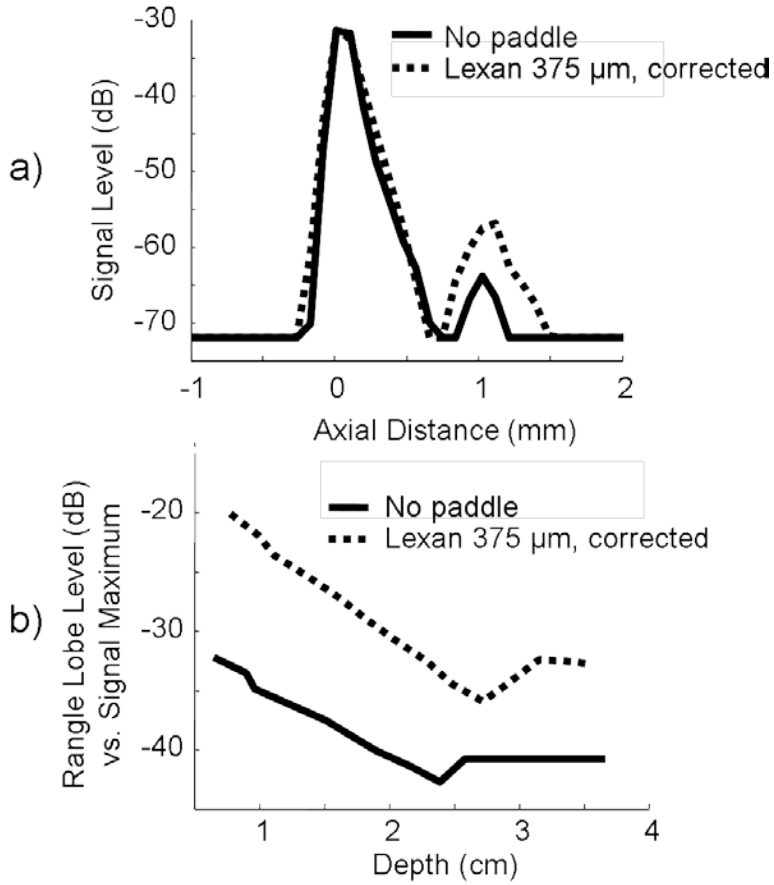

Fig. 3.4: a) Axial LSF and **b)** relative range lobe levels for no paddle and lexan 375 µm paddle with beamforming corrections. Range lobe levels, which include all reverberations, were 9 dB greater when imaging through the lexan paddle than when imaging through the TPX paddle or no paddle, primarily due to the acoustical impedance mismatch between lexan and saline.

3.4.2. Contrast

Object contrast was calculated as a function of depth with beamforming corrections implemented (Fig. 3.5a). Averaged over 25 mm to 36 mm, the contrast of the anechoic cylinder was -23 dB, -20 dB and -20 dB, respectively, for no paddle, TPX 2.5 mm paddle and lexan 375 µm paddle. Valleys in these plots are at transitions between transmit focal zones. Overall, contrast decreases with depth, mainly due to increased signal loss, beam degradation, and accumulation of multiple scattering as the beam propagates further into tissue. This reinforces the importance of positioning breast lesions

as close to the transducer as possible for high contrast, and thus high quality, ultrasound images. Mean contrast values for each paddle and no paddle are listed in Table 3.2.

3.4.3. Relative Signal Strength

Figure 3.5b shows relative signal strength for the TPX and lexan paddles over common breast lesion depths. Signal loss through the paddles occurred in the form of beam absorption and reflection. At depths greater than 3.2 cm, acoustic and electronic noise caused a minor rise in relative signal loss. The TPX paddle exhibited less signal loss averaged over the 4 cm range than the lexan paddle (-6 dB and -8.3 dB, respectively), despite being 6 times thicker. These values are listed in Table 3.2.

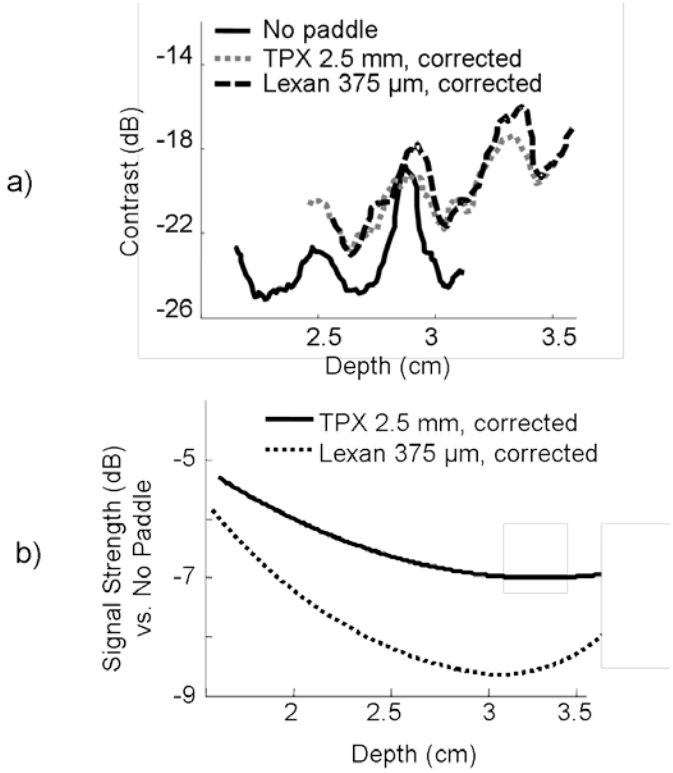

Fig. 3.5: a) Contrast between a small anechoic cylinder (mimicking a simple cyst) lying orthogonal to the image plane and a uniform speckle background, shown as a function of depth for TPX and lexan paddles, and no paddle. Contrast decreases with depth as the ultrasound beam is attenuated. Valleys correspond to transitions between transmit focal zones. **b)** Signal strength compared to no-paddle, with beamforming corrections over common breast imaging depths. TPX is clearly a much less acoustically attenuating material than lexan.

3.4.4. Evaluation of TPX Paddles ≤ 2.5 mm

Image performance of thinner TPX paddles (250 μm and 1.0 mm) was also compared with TPX 2.5 mm results. These thinner paddles exhibited similar LSF and contrast values as the 2.5 mm paddle, but with less signal loss (-2.4 dB and -4.2 dB, respectively). When less signal loss or a more flexible paddle is preferred, these paddles could also be used for mammographically compatible ultrasound. Even so, thin paddles exhibit greater deformation than thicker paddles, which results in a non-planar scan surface for the ultrasound probe. This trade-off between signal loss and paddle deformation can be decided according to system design and requirements.

3.4.5. Summary of Test Object Results

Overall, imaging through a mammographic paddle only mildly degraded test object image quality when beamforming corrections were implemented. Compared with no paddle values, LSF FWHM calculated through paddles increased 10% (lexan 375 μm paddle) and 17% (TPX 2.5 mm paddle) in the elevational direction and ≤ 5% in the lateral and axial directions for both paddles. Sidelobe levels were increased ≤ 4 dB regardless of paddle material and range lobe levels were comparable between no paddle and the TPX 2.5 mm paddle, but increased 9 dB with the lexan 375 μm paddle. Signal loss was 8 dB greater through the lexan paddle than through no paddle, but only 6 dB greater through the TPX paddle even though it was 6 times thicker than the lexan paddle. A summary of all these image quality measurements is listed in Table 3.2.

Based on these results, it is clear that the TPX 2.5 paddle performed better than the lexan 375 μm paddle overall and the minor losses in image quality through this paddle should not inhibit detection or characterization of lesions. To determine whether these losses had clinical impact, we compared cyst contrast, lesion detectability, and overall image quality with and without a mammographic paddle in human subjects, as described below.

Table 3.2: Image quality summary based on test object experiments for no paddle, TPX 2.5 mm paddle and lexan 375 μm paddle. Beamforming corrections were implemented on all relevant measurements.

Paddle	***No paddle***	***TPX 2.5 mm***	***Lexan 375 μm***
Elevational FWHM (mm)	0.90 ± 0.17	1.05 ± 0.18	0.99 ± 0.18
Elevational FWTM (mm)	2.1 ± 1.0	2.6 ± 1.2	2.2 ± 1.1
Mean sidelobe level (dB)	-19.4	-16.2	-15.3
Lateral FWHM (mm)	0.39 ± 0.04	0.40 ± 0.02	0.40 ± 0.03
Lateral FWTM (mm)	0.70 ± 0.07	0.72 ± 0.04	0.81 ± 0.12
Axial FWHM (mm)	0.23 ± 0.03	0.22± 0.02	0.24 ± 0.02
Axial FWTM (mm)	0.48 ± 0.04	0.46 ± 0.02	0.54 ± 0.03
Range lobe levels (dB)	-39 ± 3.1	-40 ± 3.5	-30 ± 3.3
Contrast (dB)	-23	-20	-20
Mean signal strength vs. no paddle (dB)	0	-6.0	-8.3

3.4.6. Human Subject Scans

Before high quality images can be obtained with the combined system, adequate human subject positioning, acoustic coupling, and breast stabilization must occur. Though these topics were addressed more thoroughly in a separate study, preliminary

efforts to stabilize and sonographically image the breast through the paddle will be briefly mentioned here [24].

Stable positioning of the compressed breast is crucial to ensure efficient scanning procedures, complete breast coverage, and accurate registration of ultrasound and mammographic images. If the human subject's breast begins to slip during the procedure, the paddle will lose contact with parts of the breast and important structural information will be lost. The breast might then need to be removed from compression and repositioned, contributing to human subject procedure time.

Adding a Mammopad under the breast helped prevent it from sliding during compression, and human subjects find the soft material comfortable. Foam wedges used to push the areolar region upward towards the paddle were partially successful at improving imaging of anterior breast tissue. Ultrasound gel and water have successfully coupled the transducer to the paddle, allowing it to scan across the paddle without interruptions in coupling contact, though water is more easily applied and removed. However, none of the coupling materials (mineral oil, ultra-myossage lotion, glycerin, or "sticky" primrose oil) were able to keep the breast in the same position at the end of the scan as at the beginning. Recent work has investigated better coupling materials for this purpose and the results of this work were implemented in Chapters 4, 5, and 6 [24].

Though these methods of coupling and stabilization were not necessarily ideal, they were sufficient to obtain preliminary human subject images of simple cysts which could be compared to the image quality of direct-contact scans.

Treating the human subject cysts as ellipsoids, mean areas in automated, through-paddle and hand-held, direct-contact scans were 150 ± 140 mm^2 and 190 ± 160 mm^2,

respectively. Differences in apparent cyst size were most likely caused by alteration of the cyst's shape in the third dimension during compression. Mean depths of the centers of the cysts in the two scan modes were 19 ± 1.8 and 18 ± 3.0 mm. There was no distinguishable correlation between contrast and cyst depth because cyst depths were so similar.

In through-paddle and direct-contact scans, average signal levels were: cyst -68 and -69 dB; fat -52 and -52 dB; and glandular -45 and -44 dB, respectively. This indicates that the contrast in through-paddle and direct-contact was 14 ± 10 and 16 ± 9 dB, respectively, between fat tissue and cyst and 25 ± 21 and 27 ± 23 dB, respectively, between glandular tissue and cyst (Fig. 3.6 a,b). The ~1.5 - 2.0 dB loss in contrast for both types of tissue is slightly less than the 3 dB contrast loss calculated in the test object scans averaged over a 4 cm depth, because human subject contrast was calculated only at cyst levels. In six out of 10 human subjects, hand-held, direct-contact fat-to-cyst contrast was greater than automated, through-paddle fat-to-cyst contrast. In four out of six human subjects in which substantial glandular signal could be identified at the same depth as the cyst, direct-contact cyst-to-glandular-tissue contrast was greater than through-paddle cyst-to-glandular-tissue contrast. Cyst-to-fat CNR for through-paddle and direct-contact scans was 5.5 ± 3.0 and 7.5 ± 3.6, respectively, and cyst-to-glandular tissue CNR was 9.8 ± 1.3 and 10.0 ± 2.0, respectively. This data was not statistically significant because of the small size of the study group. In every case for both scan modes, cyst signal levels were lower than fat signal levels, which were lower than glandular signal levels.

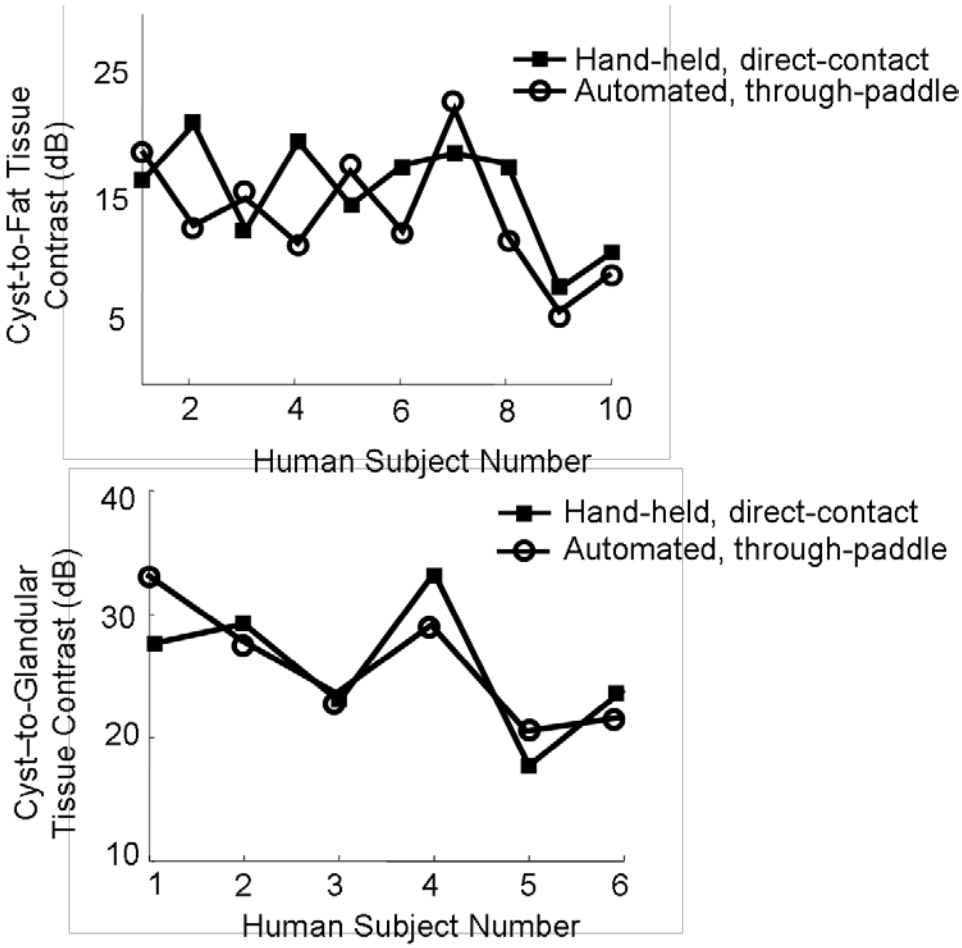

Fig. 3.6: a) Cyst-to-fat contrast in 10 human subjects with simple cysts. **b)** Cyst-to- glandular contrast for the six human subjects whose breasts contained enough glandular tissue for measurement. Contrast levels in both cases were similar, and small differences proved to be statistically insignificant.

Contrast and CNR losses can be expected from multiple scattering, discrete reverberations, and clutter in the region of the cyst. These factors will increase the noise signal level in the cyst, decreasing contrast and CNR values. Specifically, cyst fill-in can be caused by multiple scatterers acting in the axial direction proximal to the anechoic cysts [23]. Cysts larger than 200 mm^2 exhibited visible fill-in, whereas smaller cysts appeared to be hypoechoic throughout their entire area. Radiologist interpretations were that the moderate fill-in did not obstruct recognition of the cyst as long as it mostly remained hypoechoic. Multiple scattering effects contributing to cyst fill-in could further

be minimized by employing a lower frequency transducer during scans at the expense of spatial resolution. A t-test performed on contrast and CNR values produced indicated that differences in through-paddle and direct-contact contrast and CNR were not statistically significant ($P > 0.1$).

To determine whether these minor losses had clinical impact, two radiologists were asked to blindly evaluate six randomly chosen, corresponding automated, through-paddle and hand-held, direct-contact scans according to overall image quality and lesion detectability. Images created by both scan types were presented in cineloop format. Of 12 ratings of six cases, the radiologists ranked overall image quality of the through-paddle scans equal to or better than their corresponding direct-contact scan in 83% of the cases. In terms of ease of lesion detectability, the through-paddle scan was rated equal to or better than the direct-contact scan in 75% of the cases. Additionally, the radiologists ranked the image quality of scans individually on a scale from 1-5, with a score of "1" corresponding to "poor" and a score of "5" corresponding to "excellent". The mean rating for the through-paddle images was 3.3 and the mean rating for the radiologist performed direct-contact images was 3.0. Having the automated-through paddle scans sampled finely and uniformly throughout the imaged volumes may have contributed to their perceived higher image quality. Table 3.3 summarizes *in vivo* image quality comparisons of direct-contact and through-paddle images. These results further validated that minor image quality losses observed with this system should not impair detection or characterization of cystic lesions.

Table 3.3: Quantitative and qualitative comparison of hand-held, direct-contact vs. automated, through-paddle *in vivo* ultrasound scans of 10 women with simple cysts.

	Percentage of through-paddle ≥ direct-contact images
Cyst-to-fat tissue contrast	60%
Cyst-to-glandular tissue contrast	67%
Lesion detectability	75%
Overall image quality	83%

Briefly, since this preliminary experiment was conducted, *in vivo* through-paddle image quality results have been less encouraging for several reasons. First, the minor image quality losses experienced by imaging through the TPX paddles led to the removal of the beamforming corrections in future implementations of the software. Additionally, positioning of breast masses has been difficult, with the paddle sometimes restricting visualization of deep masses, masses close to the chest wall, and masses in the areolar region. This study did not evaluate image quality losses due to acoustic coupling materials, such as gel and hairspray, which cause additional attenuation. However, based on the initial results presented in this chapter, through-paddle elastography was explored.

3.4.7. Implications for Through-Paddle Elastography

Minimizing adverse effects of imaging ultrasound through a mammographic paddle is essential to maximize the potential of elasticity imaging with this system. Refraction effects could increase decorrelation by changing speckle characteristics under compression. Excessive attenuation through the paddle could reduce the depth that elastography could explore by reducing the available speckle for the algorithms to track.

Reverberations in the image could be mistaken for speckle, leading to artifacts in the elastogram. The next chapter will explore the utility of elastography through the TPX mammographic paddles.

3.5. Conclusions

The combined system with stable breast compression promises to utilize the synergism between ultrasound and x-ray mammography for more accurate and efficient breast lesion examination. Advanced features such as elasticity imaging, vascular imaging, and tomosynthesis may further increase our ability to discriminate between benign and malignant lesions, as well as to detect changes in lesions over extended periods.

Among those tested, the TPX paddle was judged best overall for ultrasound and mammographic imaging requirements. FWHM and FWTM values in the elevational direction were within 17% of no paddle values and, in lateral and axial directions, were within 5% of no paddle values when beamforming corrections were implemented. These corrections were critical in maintaining resolution levels very close to no paddle values, particularly in the lateral direction and for thicker paddles.

Range lobes due to the TPX paddle were comparable or modestly increased relative to no paddle levels (37 to 40 dB down from maximum signal level). Range lobes can be further minimized by choosing an impedance-matched material. The 6 dB pulse echo signal strength loss due to beam attenuation and reflection through the TPX 2.5 paddle is minor compared with the full dynamic range (72 dB) of gray-scale images and

could be reduced by imaging through a thinner paddle, such as TPX 0.25 mm or 1.0 mm, at the expense of additional paddle deformation.

Human subject movement, comfort and examination time remain targets for further effort with the system. Additional coupling materials should be explored, as well as mechanical alternatives, such as tilting the compression paddle to image closer to the chest wall. A hollow wedge rather than a foam wedge might hold the areolar region of the breast against the paddle well enough to provide adequate contact for anterior breast imaging.

Cysts and lesions near the chest wall are still difficult to image because of the rigid wall of the compression paddle and the designs of the transducer housing and carriage. Imaging in trapezoidal (virtual convex) mode or beam steering at ±20° somewhat alleviates this problem by electronically steering the transducer to image regions-of-interest that would not be seen in a rectangular scan. Though not quantified, the initial images created using these formats (Fig. 3.7) suggest high image quality can be maintained through TPX paddles.

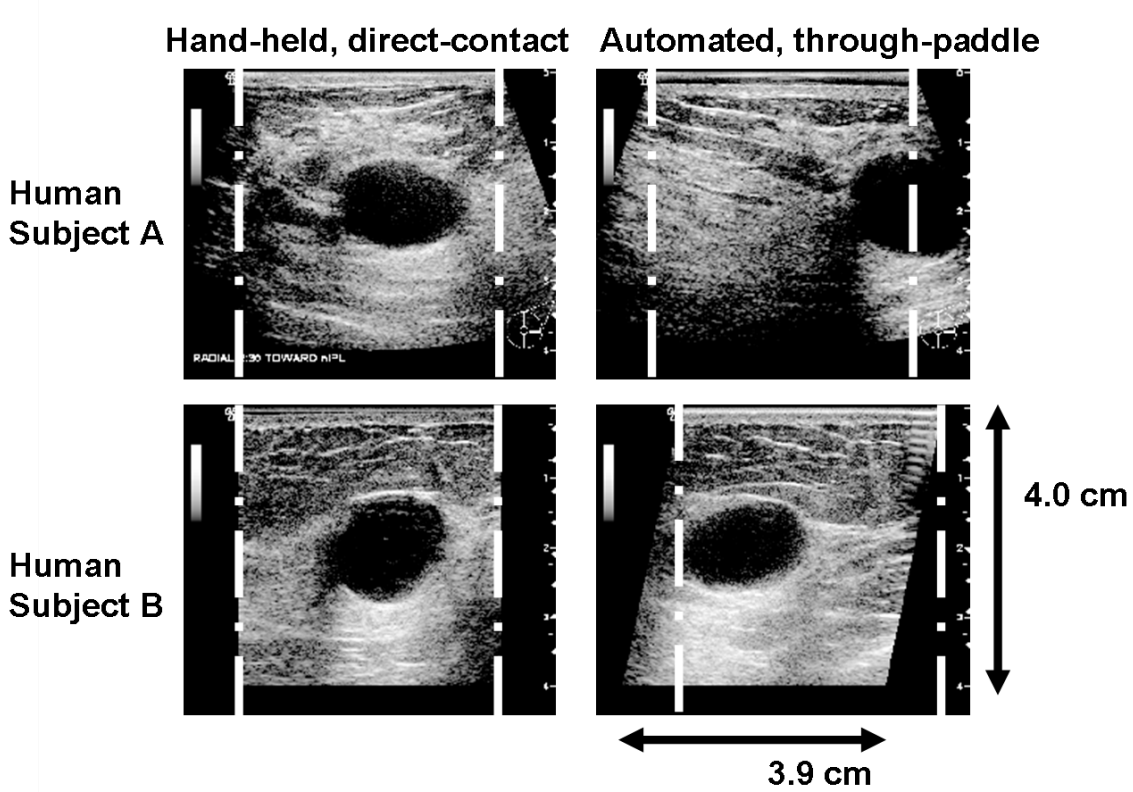

Fig. 3.7: Human subject A: **(left)** hand-held, direct contact scan of cyst and **(right)** automated, through-paddle scan of cyst, both in trapezoidal (virtual convex) mode. Human subject B: **(left)** hand-held, direct-contact scan and **(right)** automated, through-paddle scan with 20° beam steering. White lines indicate the image region of a rectangular scan mode. Changing to different scan modes increases lesion visibility close to the chest wall, which might otherwise be obstructed because the finite transducer housing thickness restricts access at the chest wall.

With the combined system, small relative contrast and CNR loss *in vivo* is possibly due to increased reverberation and multiple scattering signals, LSF degradation and signal loss in the paddle, all of which can be seen in the hypoechoic cysts. These minor contrast losses are approximately consistent with the signal loss (~6 dB) and increased range lobe levels (~2 dB) measured when imaging line targets through the compression paddles. Half the signal loss through the paddles can be compensated for, with no increased ultrasound exposure levels to the human subject, by increasing the power transmitted into the breast to the levels that would have existed with no paddle. In subjective assessments, minor image quality losses did not affect interpretations by

radiologists, reinforcing our belief that the losses in these scans do not have an adverse clinical impact. These minor losses may well be worth the many advantages of 3D, whole breast automated ultrasound scanning and co-registered mammography.

3.6. References

[1] Conway WF, Hayes CS, Brewer WH. Occult breast masses: Use of mammographic localizing grid for US evaluation. Radiology 1991; 181: 143-146.

[2] Taylor KJW, Merritt C, Piccoli C, et al. Ultrasound as a complement to mammography and breast examination to characterize breast masses. Ultrasound in Med. and Biol. 2002; 28(1): 19-26.

[3] Moss HA, Britton PD, Flower CDR, Freeman AH, Lomas DJ, and Warren RML. How reliable is modern breast imaging in differentiating benign from malignant breast lesions in the symptomatic population? Clin Radiology 1999; 54:676-682.

[4] Lister D, Evans AJ, Burrell HC, et al. The accuracy of breast ultrasound in the evaluation clinically benign discrete, symptomatic breast lumps. Clin. Radiology 1998; 53:490-492.

[5] Stavros AT, Thickman D, Rapp CL, Dennis MA, Parker SH, and Sisney GA. Solid breast nodules: Use of sonography to distinguish between benign and malignant lesions. Radiology 1995; 196:123-134.

[6] Jackson, VP, Hendrick RE, Reig SA, Kopans DB. Imaging of the radiographically dense breast. Radiology 1993; 188(2): 297-301.

[7] Bassett LS, Kimme-Smith C. Breast Sonography. AJR 1991; 156**:** 499-455.

[8] Jackson VP. The role of US in breast imaging. Radiology 1990; 177: 305-311.

[9] Novak D. Indications for and comparative diagnostic value of combined ultrasound and x-ray mammography. Eur J Rad 1983; 3 Suppl 1: 299-302.

[10] Kolb TM, Lichy J, Newhouse JH. Occult cancer in women with dense breasts: Detection with screening ultrasound: Diagnostic yield and tumor characteristics. Radiology 1998; 207: 191-198.

[11] Brem RF, Gatewood OMB. Template-guided breast US. Radiology 1992; 184: 872-874.

[12] Lunt LG, Peakman DJ, Young JR. Mammographically guided ultrasound: a new technique for assessment of impalpable breast lesions. Clin Radiol 1991; 44:85-8.

[13] Schütze B, Marx C, Fleck M, Reichenbach J, Kaiser WA. Diagnostic evaluation of sonographically visualized breast lesions by using a new clinical amplitude/velocity reference imaging technique (CARI sonography). Invest. Radiol 1998; 33:341-347.

[14] Richter K. Clinical amplitude/velocity reconstructive imaging (CARI): A new sonographic method for detecting breast lesions. BR. J. Radiol 1995; 68:375-384.

[15] Richter K. et al. Detection of malignant and benign breast lesions with an automated US system: results in 120 cases. Radiology 1997; 205:823:830.

[16] Richter K. Technique for detection and evaluating breast lesions. Ultrasound Med, 1994 13:797-802.

[17] Moskalik AP, Carson PL, Meyer CR, Fowlkes JB, Rubin JM, Roubidoux MA. Registration of three-dimensional compound ultrasound scans of the breast for refraction and motion correction. Ultrasound in Med and Biol. 1995; 21: 769-778.

[18] Kelly-fry E and Jackson VP. Adaptation development and expansion of x-ray mammography techniques for ultrasound mammography., Ultrasound Med. 1991; 10:S-16.

[19] Hoctor RT, Thomenius KE. Focus Correction for Ultrasound Imaging Through Mammography Compression Plate. US Patent No. 6,607,489, Aug. 19, 2003.

[20] Krücker JF, Fowlkes JB and Carson PL. Sound speed estimation using automatic ultrasound image registration. IEEE Trans Ultrason Ferroelectr Freq Control 2004; 51(9): 1095-1106.

[21] Department of Health and Human Services, Food and Drug Administration. Mammography quality standards final Rules. Federal Register Oct. 28, 1997; 68(208): 55852-55994.

[22] Kapur A, Carson PL, Eberhard J, et al. Combination of digital mammography with semi-automated 3D breast ultrasound. Technol Cancer Res. Treat 2004 Aug; 3(4):325-334.

[23] Carson, PL and Oughton TV. A modeled study for diagnosis of small anechoic masses with ultrasound. Radiology 1977; 122(3):765-71.

[24] Sinha SP, Goodsitt MM, Roubidoux MA, Booi RC, LeCarpentier GL, Lashbrook CR, Thomenius K, Chalek CL, Carson PL. Automated ultrasound scanning on a dual-modality breast imaging system: coverage and motion issues and solutions. J Ultras Med. 2007; 26(5):645-55.

[25] Booi RC, Krücker JF, Goodsitt MM, O'Donnell M, Kapur A, LeCarpentier GL, Roubidoux MA, Fowlkes JB, Carson PL. Evaluating thin compression paddles for mammographically compatible ultrasound. Ultras. in Med. and Biol. 2007; 33(3): 472-482.

[26] Booi RC, Krücker J, Goodsitt MM, O'Donnell M, Kapur A, LeCarpentier GL, Roubidoux MA, Fowlkes JB, Carson PL. "Evaluation of thin compression plates for mammographically compatible breast ultrasound." Proceedings of the 2004 IEEE Ultrasonics Symposium; p. 2129-2132.

CHAPTER 4

2D AND 3D ELASTOGRAPHY THROUGH A MAMMOGRAPHIC PADDLE

4.1. Chapter Overview

The purpose of this chapter is to explore the feasibility and utility of 2D and 3D elastography through a TPX mammographic paddle. All experiments in this chapter were conducted on a tissue-mimicking rubber phantom with multiple isoechoic and anechoic inclusions. First, best case imaging parameters were explored in the 2D case. These parameters identified appropriate paddle thickness, transducer frequency, and transducer type to minimize decorrelation due to elevational motion and maximize correlation coefficient values and lesion signal-to-noise ratio (SNR_{ε}). The final 2D through-paddle elasticity results were then compared with their freehand analogues. Next, methodology was extended to 3D and best case imaging parameters were again investigated. Specifically, the best 3D elasticity data acquisition method to minimize scan time and system mechanical backlash was determined. The appropriate number of elevational slices and slice thickness as functions of the 3D speckle tracking algorithms and elevational beamwidth of the transducer were evaluated. The correlation coefficient and lesion SNR as a function of strain step size was compared in the 2D freehand, 2D through-paddle, and 3D through-paddle cases. Portions of the work presented in this chapter have been published in [10] and [11].

4.2. Introduction

Breast elastography has been demonstrated in 1D and 2D using freehand systems [1-3]. In freehand elastography, deformations are created when a skilled operator manually compresses the breast while holding the ultrasound transducer. These studies have shown that freehand elasticity imaging produces comparable sensitivity and CNR to mechanically induced transducer motion [2]. However, freehand elasticity scanning has several major disadvantages: 1) it is difficult to avoid out-of-plane motion during compression, which reduces contrast, and tracking fidelity; 2) the quality of freehand elastography highly depends on operator skill; and 3) it is difficult to accurately obtain consistent, controlled compression steps with manual compression.

Applying external strain with a mammographic paddle as part of a combined 3D US/Digital X-ray system could provide more uniform deformation and breast stability than freehand elastography, offering opportunities to improve technique fidelity. Because the compression process is automated, operator skill will no longer be a major determinate in image quality. Additionally, compression steps can be controlled with great precision and over a wide range of compression steps.

Unfortunately, through-paddle 2D elastography may also pose several challenges. First, because real-time freehand systems can provide feedback to the operator during compression, compression can be optimized during the scan. Imaging through a mammographic paddle restricts the views over which compression can be applied, and thus compression direction cannot be modified after scanning has begun. Additionally, imaging is limited to one of three mammographic views – cranial-caudal (CC), lateral-medial (LM), or lateral-medial-oblique (LMO) – and thus optimal positioning of the

breast lesion (close to the transducer and away from image edges) may not possible with through-paddle elastography. Thus, the first goal of this chapter was to evaluate the performance of 2D through-paddle elastography compared with freehand elastography.

Ultimately, the aim of elastography is to acquire high quality displacement estimates and corresponding strains in all three dimensions to fully characterize tissue and reconstruct the elastic modulus. The control and precision of compression with through-paddle elastography can be easily extended to acquire elasticity data over a 3D volume using a 1D array. Through-paddle 3D elastography may prove especially efficacious over freehand 3D elastography, where it is nearly impossible to manually acquire parallel compression planes over a 3D volume and retrospective warping of the 3D volume is required for accurate analysis [4].

There exist many potential benefits in conducting 3D speckle tracking over a 3D volume compared with 2D tracking over one slice of that volume. First, as demonstrated by Chen et al. (2006), 3D speckle tracking reduces artifacts in strain images by tracking elevational (out-of-plane) motion [5]. This improves tracking accuracy in all three directions, increasing elastogram SNR and correlation coefficient values. Additionally, 3D elastography provides information over an image volume, increasing the robustness of the information that can be extracted from those images.

Research on 3D elastography has been limited thus far. Lindop et al. (2006) applied 1D speckle tracking to a 3D volume obtained from freehand and reported good contrast but problems with robustness [4]. Konofagou et al. (2000) conducted 3D finite element analysis simulations with 1.5D and 2D arrays to demonstrate the feasibility of mapping the full strain tensor [6]. As mentioned previously, Chen et al. (2006) conducted

3D speckle tracking simulations to reduce decorrelation due to out-of-plane motion and increase tracking accuracy in all three directions [5]. Based on these limited but promising results, the second major goal of this chapter was to evaluate the efficacy of 3D through-paddle elastography compared with its 2D analogues.

4.3. Methods

4.3.1. Tissue-Mimicking Breast Phantom

A breast-shaped rubber phantom (model BB-1, ATS Laboratories, Bridgeport, CT, USA), with a 1mm diameter palpable, isoechoic inclusion located 1-2 cm from the transducer face under cranial-caudal compression, was imaged for all phantom experiments (Fig. 4.1). This phantom exhibits fully developed speckle under the ultrasonic imaging conditions applied in this study and speed of sound in the phantom = 1.49 mm/μs.

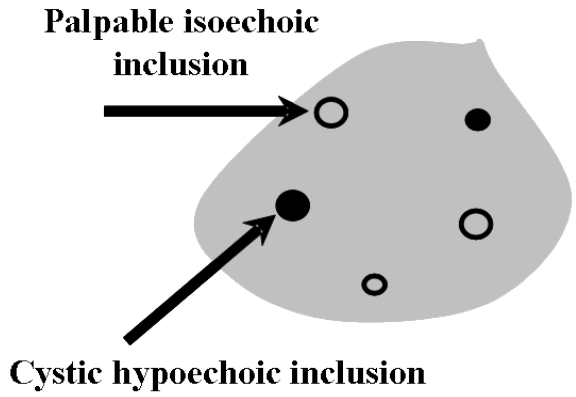

Fig. 4.1: Rubber phantom used in all experiments in this study with multiple palpable isoechoic and cystic hypoechoic inclusions.

4.3.2. Experimental Setup

To allow for fine compression control, all elastography experiments were conducted on a stand alone mammography-mimicking ultrasound unit built by General

Electric Global Research Center (Schenectady, NY, USA) and University of Michigan researchers (Ann Arbor, MI, USA) (Fig 4.2a). This research unit reproduces the through-paddle ultrasound of the combined system, but only images the compressed breast from the cranial-caudal mammographic view. Hardware and software were developed to semi-automatically drive the transducer across the compression paddle, as well as communicate with the LOGIQ 9 ultrasound system to trigger image and data acquisition. Four stepper motors and a transducer carriage which holds the transducer during experiments were attached to the mammography-mimicking stand alone unit (Fig. 4.2b). The motors were actuated via two stepper motor controllers (Velmex, Bloomfield, NY, USA) from a nearby computer; two motors translated the transducer carriage and two translated the upper and lower compression paddles with accuracy up to ± 30 μm [7]. Note that the lower compression paddle was mechanically damped to reduce vibrations associated with its motion during elastography. Additional software (The_Booi_GUI.m, Matlab, The Mathworks, Natick, Massachusetts, USA) was written to control all data acquisition parameters during experiments, including compression speed, deformation step size, total amount of deformation, and, for 3D elasticity, number of slices, slice thickness, and scan orientation (Fig. 4.2c).

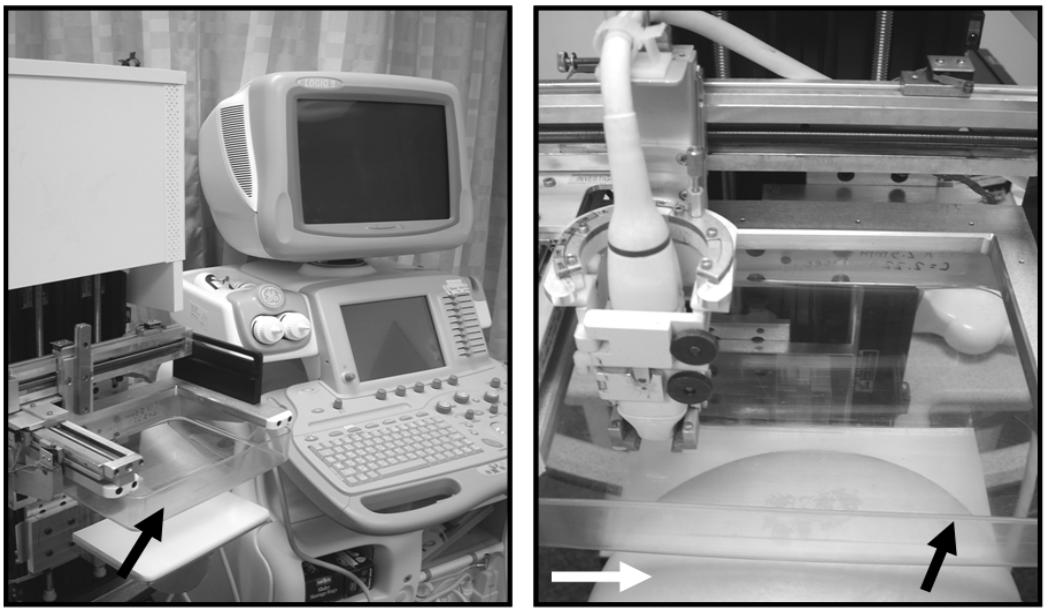

a. b.

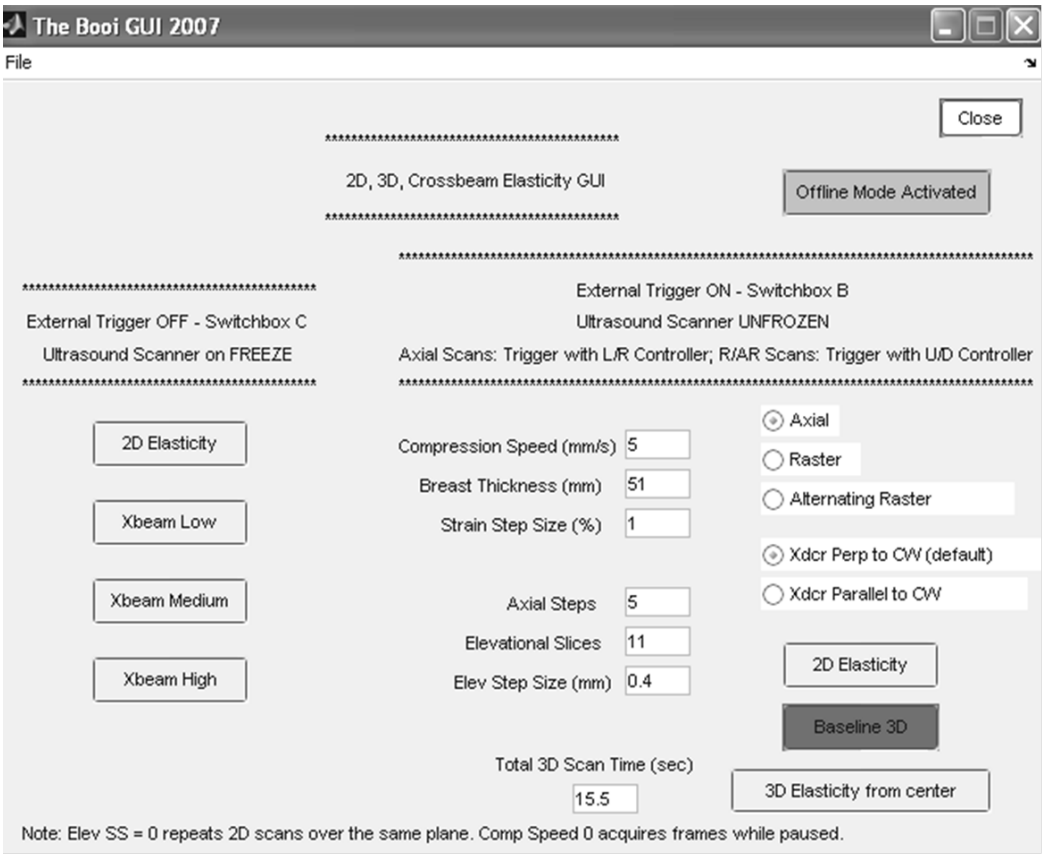

c.

Fig. 4.2: (a) Stand alone mammography-mimicking unit **(left)** with TPX 2.5 mm mammographic paddle attached (black arrow) and GE LOGIQ 9 ultrasound scanner **(right). (b)** Close-up view of phantom (white

arrow) compressed by the mammographic paddle (black arrow) with transducer and carriage attached. **(c)** Screen shot of the graphical user interface (The_Booi_GUI.m) which controlled all experiments.

For consistency, the phantom was initially positioned in the same way for all experiments. First, the phantom was placed on the lower compression paddle and LithoClear gel (Sonotech, Bellingham, WA) was added to provide coupling between the mammographic paddle and the phantom. The ultrasound transducer was attached to its carriage and tap water was poured into the upper compression paddle to provide coupling between the transducer with the paddle. Next, the phantom was compressed until contact was made across the entire ultrasound image. The transducer was manually scanned to the center of the inclusion, which was identified visually and radiofrequency (RF) ultrasound frames for elastography were acquired by continually compressing the lower paddle upward. The resulting radiofrequency (RF) ultrasound images were 4 cm x 3.9 cm. Distinctions between this process for 2D and 3D are described further below.

A schematic of the experimental setup is provided in Fig. 4.3. To acquire RF images for 2D elastography, a graphical user interface (GUI) on a nearby computer sends a signal through Serial Port 2 to raise the lower compression paddle at a speed of 2.5 mm/sec for up to 2 sec, inducing up to 7% strain in the phantom. Simultaneously, through Serial Port 1, the other stepper motor controller sends a signal to the Switchbox, which signals the Freeze/Unfreeze button through the right footswitch input on the LOGIQ 9 scanner at the beginning and the end of compression. In this way, the ultrasound scanner unfreezes when compression begins, continuously collects RF images at a frame rate of 43 Hz during compression, and freezes when compression ends. Thus, the cineloop on the scanner is filled with up to 91 RF images during a single 2D compression scan.

Because the ultrasound cineloop could only collect data over 2 sec before it was full, alternative methods were developed for acquisition of RF frames for 3D elastography. External RF frame triggering was simultaneously employed as the phantom was compressed to ensure data was collected within a reasonable scanning time. As in 2D data acquisition, over the 4 cm imaging depth, one focal spot was set at 3 cm, corresponding to an allowed frame rate of 43 Hz. However, a slightly lower frame rate of 33 Hz was actually utilized with external triggering. All scanning was programmed to start from the center of the inclusion at minimum compression. The details of this scanning procedure will be given for axial scanning acquisitions (described in section 4.3.5), but the methods are analogous for raster and alternating raster scanning. First, a signal was sent through Serial Port 1 to move the transducer elevationally to the position which would correspond to the first slice in the 3D volume. Then, compression was induced as in 2D by sending a signal through Serial Port 2 to the stepper motor controller to raise the lower mammographic paddle for compression. Simultaneously, through Serial Port 1, the other stepper motor controller sent a signal to the Switchbox, which signaled the external triggering on the LOGIQ 9 scanner through its left footswitch input at each desired axial location. Because the compression speed was known, in practice this corresponded to the length of time required to deform the phantom the desired amount. After full axial compression over the first slice, the tissue was decompressed at a speed of 10 mm/sec while the transducer simultaneously moved to the location of the next slice. This process of compression, then decompression, then elevational translation was repeated over the entire 3D volume. In this manner, all axial steps at different elevational locations were triggered at the same location and within a reasonable scanning time.

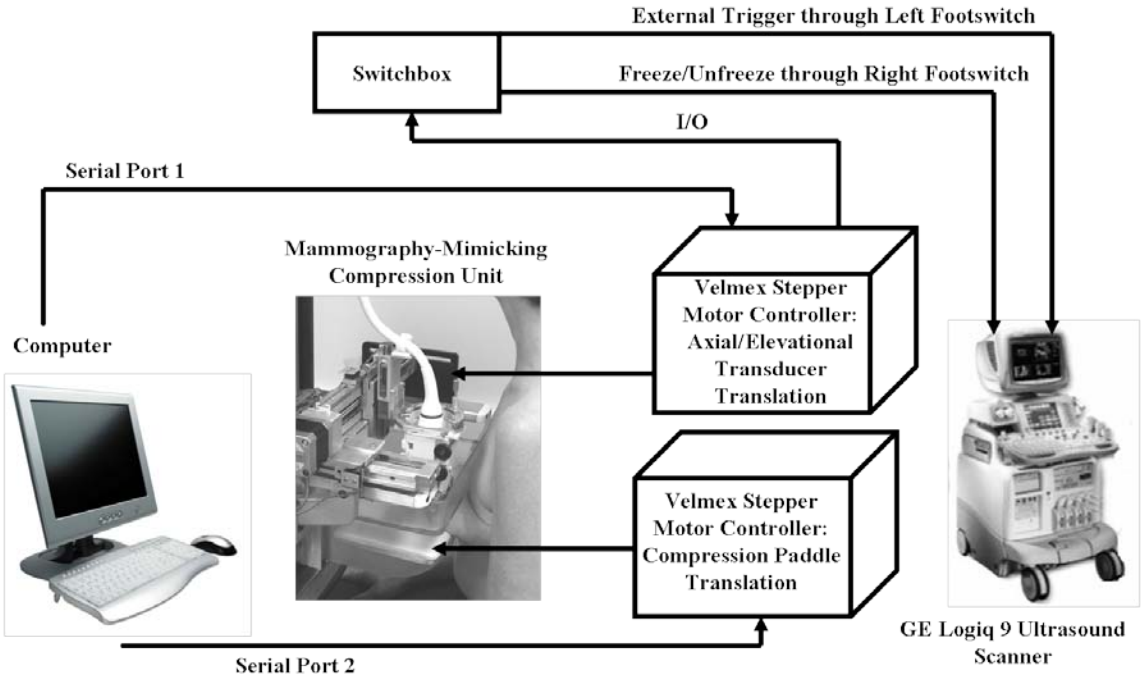

Fig. 4.3: Schematic of experimental setup. For 2D elastography, one stepper motor controller raises the lower compression paddle while the other freezes and unfreezes the LOGIQ 9 ultrasound scanner to allow continuous collection of data over 2 sec. For 3D elastography, as compression is induced over each slice with one controller, the other externally triggers the ultrasound scanner to acquire RF frames at different axial locations. Then, the phantom is decompressed while the transducer is translated elevationally to the position corresponding to the next slice. This process is repeated over the desired 3D volume. External triggering allows for fast and accurate acquisition of RF frames at consistent axial positions over many elevational slices.

4.3.3. 2D, 3D Phase-Sensitive Speckle Tracking

All 2D and 3D elasticity data were processed using conventional 2D and 3D phase-sensitive correlation-based speckle tracking algorithms, described in [5, 8-9] and reviewed in Chapter 2. This processing will be briefly summarized here.

Final outputs of the 2D processing are the lateral displacement $u(x, y)$, axial displacement $v(x, y)$, and magnitude of the correlation coefficient $|\rho(x, y)|$. Analogously, the final outputs of the 3D processing are the axial displacement $v(x, y, z)$, lateral displacement $u(x, y, z)$, elevational displacement $w(x, y, z)$, and magnitude of the correlation coefficient $|\rho(x, y, z)|$. The final axial normal strain image (elastogram) was

produced from the axial derivative of the axial displacement estimates, according to equation 4.1:

$$\varepsilon = \frac{\partial v}{\partial y} \tag{4.1}$$

To directly compare 3D speckle tracking results with their 2D analogues, the center slice from 3D data was extracted and analyzed using traditional 2D speckle tracking. In this way, image quality could be directly compared between 2D and center-slice 3D strain and correlation coefficient images.

Image quality was quantified using the magnitude of the 2D or 3D correlation coefficient and the SNR of the final axial elastogram (SNR_ε), calculated as described in [8]:

$$SNR_\varepsilon = \frac{E[\varepsilon]}{\sigma_\varepsilon} \tag{4.2}$$

where ε is the component of the strain tensor, $E[\varepsilon]$ is the mean strain, and σ_ε is the variance of strain estimates.

4.3.4. Imaging Methods – 2D Through-Paddle Elastography

The goal of the phantom experiments was to determine optimal data acquisition techniques for 2D through-paddle elastography with this system and compare the results with freehand elastography under the same conditions.

Three transducer types (M12L – a 1.5D array - and 10L and 7L – 1D arrays) were evaluated at several frequencies between 5-10 MHz with 3 TPX paddle thicknesses (0.25, 1.0, 2.5 mm) to determine which parameters would prove best for 2D elastography. In

particular, the mean correlation coefficient and SNR_{ε} were compared for varying parameters.

For 2D elastography, out-of-plane motion can be a primary source of decorrelation and error [5]. Thus, out-of-plane motion was measured by translating each transducer across the phantom in 50 μm steps over a 400 μm distance. Each image was correlated to the first in the sequence using conventional 2D phase-sensitive speckle tracking to determine the rate of elevational decorrelation.

After the best parameters for 2D through-paddle elastography were determined, the resulting elastograms and mean correlation coefficient values as a function of step size were compared with their 2D freehand analogues.

4.3.5. Imaging Methods – 3D Through-Paddle Elastography

Similar to the 2D experiments, the objectives of the initial 3D elasticity study were 1) to determine optimal experimental methods for 3D elastographic imaging using a tissue-mimicking phantom and 2) estimate the expected improvements in image quality over 2D through-paddle elastography. The phantom studies in this chapter were designed to mimic the requirements for *in vivo* elastography. One of the most imperative goals of the 3D acquisition process was to collect data within a consistent breathing pattern; otherwise, subject breathing motion and breast slippage could dominate decorrelation when experiments are repeated *in vivo*. Thus, minimizing scan times was an important objective in all parameter selections.

Three strategies for acquiring 3D data were examined in this study, termed axial, raster, and alternating raster (Fig. 4.4). In axial scanning, the phantom was compressed

the full axial distance at each elevational location, decompressed to initial compression, and translated elevationally. This process was repeated until the number of desired elevational slices was acquired. Conversely, raster scanning translated the transducer the full elevational distance at each axial location, returned to the elevational start position, compressed the phantom by one axial step (usually 0.5% strain), and repeated this process until the desired full axial compression was reached (usually 5 times, up to 2.5% total strain). Alternating raster scanning was conducted as in raster scanning but translated the transducer elevationally in both the forward and backward directions. Thus, by never going back to the start position, alternating raster scanning reduced total scan time by a factor of 2. However, alternating raster scanning would be particularly sensitive to mechanical backlash because it acquired frames in multiple directions.

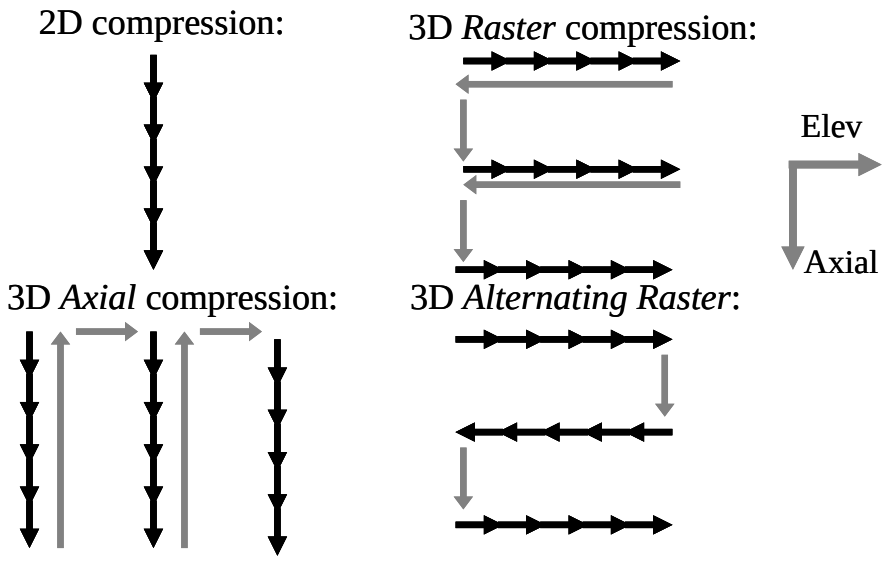

Fig. 4.4: Different scanning techniques to acquire frames for 3D elastography, shown in comparison with the standard acquisition strategy for 2D elastography.

Mechanical backlash was defined as the amount of overshoot or undershoot experienced by the system when the transducer scanning direction was reversed, and was used to quantify the mechanical precision of this system. If there was no backlash, then

there would be perfect correlation (ρ_{3D} = 1.00) between consecutive frames and no elevational or axial translation between start and end positions. However, with any mechanical system there will be some backlash.

Clearly, mechanically precise scanning over a short interval would produce the best 3D elastograms. Therefore, the first phantom experiment evaluated mechanical precision and robustness of the system as it related to each of the three scanning strategies. To verify precision in both elevational and axial directions as a function of distance, the transducer was scanned distances from 1.2 mm to 8.4 mm in steps of 0.4 mm, and frames were acquired at the beginning and end of each scan. Consecutive frames were then cross-correlated to each other using 2D speckle tracking algorithms and mean displacements were calculated. If no backlash existed in the system, then the mean displacement in the experiment would be zero. During scanning, the transducer does not translate laterally and thus mechanical precision in this direction was not quantified.

Another factor affecting system precision is tissue "creep", or relaxation, during axial scanning. If breast tissue has insufficient time to return to its original state before the next slice of data is accessed, then a distorted set of 3D data may be acquired. To conduct this experiment, the phantom was compressed in 15 increments of 0.5% axial strain, and then decompressed. A waiting time was then varied between 0-2 seconds before recompression. Each initial compression level (frames 1 to 15) was compared with its same compression level at 2nd compression time (frames 16 to 30).

Minimum parameters for elevational slice size and number of elevational slices were influenced by elevational beamwidth and number of speckle spots required for the speckle tracking algorithms, respectively. The elevational beamwidth was experimentally

measured from the full-width-half-maximum of the RF autocorrelation function as 1.2 mm. To meet Nyquist sampling requirements, the elevational slice size must be less than half of this distance to be adequately sampled, or $\leq$ 0.6 mm. Thus the slice size was varied between 0.2 mm in 0.2 mm increments to 0.8 mm to evaluate the tradeoff between slice size and image quality.

4.4. Results

4.4.1. Mammographic Paddle Selection for Through-Paddle Elastography

Chapter 3 determined that TPX paddles between 0.25 – 2.5 mm thick were the best choice for through-paddle sonography, only minimally degrading spatial resolution and increasing reverberations. Specifically, which of these paddles would be best suited for through-paddle elastography was investigated. Of the 3 TPX paddle thicknesses evaluated in this study, the TPX paddles 1.0 mm and 2.5 mm thick created strain images with fewer artifacts than the TPX 0.25 mm paddle under the same experimental conditions (Fig. 4.5). This performance was consistent regardless of transducer type or frequency. For a step size of 0.5% strain imaging with the M12L transducer at 10 MHz, the average correlation coefficient was 0.96, 0.96, and 0.97 for the TPX 0.25 mm, 1 mm, and 2.5 mm paddles respectively. Similarly, the inclusion SNR was 3.0, 3.3, and 3.6 in the axial normal elastograms.

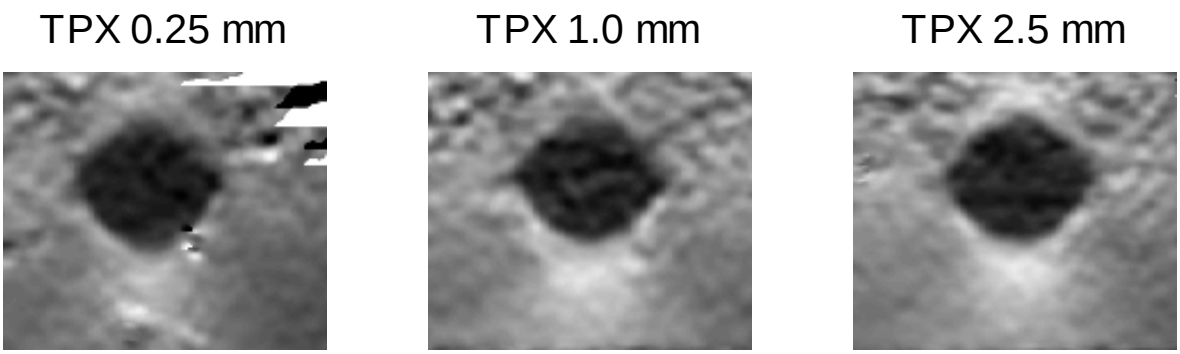

Fig. 4.5: Strain images (mean strain = 0.5%) for varying paddle thicknesses created with the M12L at 10 MHz. Artifacts are present in the elastogram created by imaging through the TPX 0.25 mm paddle, but are absent in the other two elastograms. The mean correlation coefficient was 0.96, 0.96, and 0.97 and inclusion SNR in the elastogram was 3.0, 3.3, and 3.6 for the TPX 0.25 mm, 1.0 mm, and 2.5 mm paddles, respectively.

4.4.2. Evaluation of Transducer Characteristics for Elastography

For high quality 2D elastography, RF images must be created by a relatively high frequency transducer for accurate displacement estimation, resulting elastograms should have high SNR, and correlation coefficients should be minimally affected by out-of-plane motion. Based on these requirements, decorrelation due to elevational translation was investigated first. For each of the 3 transducers tested, decorrelation due to out out-of-plane motion decreased with decreasing frequency. Averaged from 0.75 cm to 3.5 cm depths, the M12L transducer at 10 MHz decorrelated to $\rho = 0.9$ at 450 μm, the 7L at 6 MHz to $\rho = 0.99$, and the 10L transducer at 7.5 MHz to $\rho = 0.97$. At small elevational translations (< 0.3 mm), decorrelation due to out-of-plane is minimal with all transducers, however, imaging with the 10L or 7L would protect against out-of-plane motion should it occur.

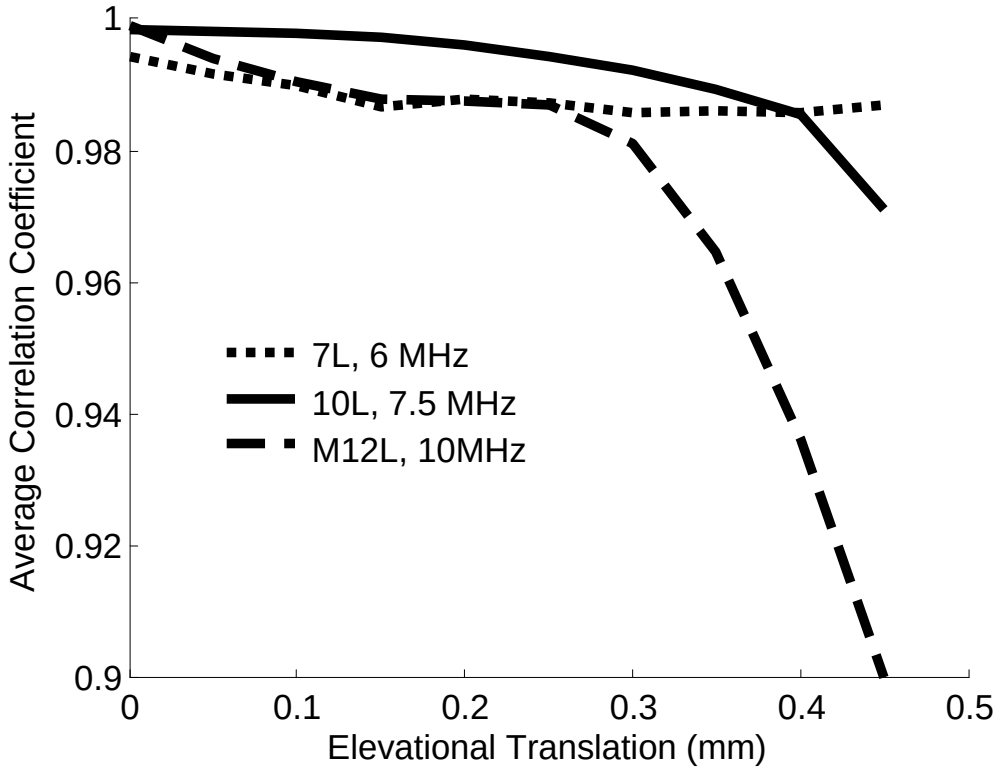

Fig. 4.6: Decorrelation due to elevational (out of plane) translation. For small elevational translations (< 0.3 mm), decorrelation is low regardless of transducer or frequency. However, as elevational translation increases, low frequency transducers maintain higher correlation coefficients.

Next, axial normal elastograms were created for each transducer and frequency by accumulating displacements in 0.5% strain steps up to 3.5% strain through the TPX 2.5 mm paddle (Fig. 4.7). Inclusion SNR was 3.6 in the elastograms created by both the 7L and M12L transducer, and was 4.0 in the elastogram created by the 10L transducer. The increased SNR from the 10L transducer was due to decreased noise in the lesion. Mean correlation coefficient values were approximately the same: $\rho = 0.97$ for the M12L and $\rho = 0.98$ for both the 10L and 7L.

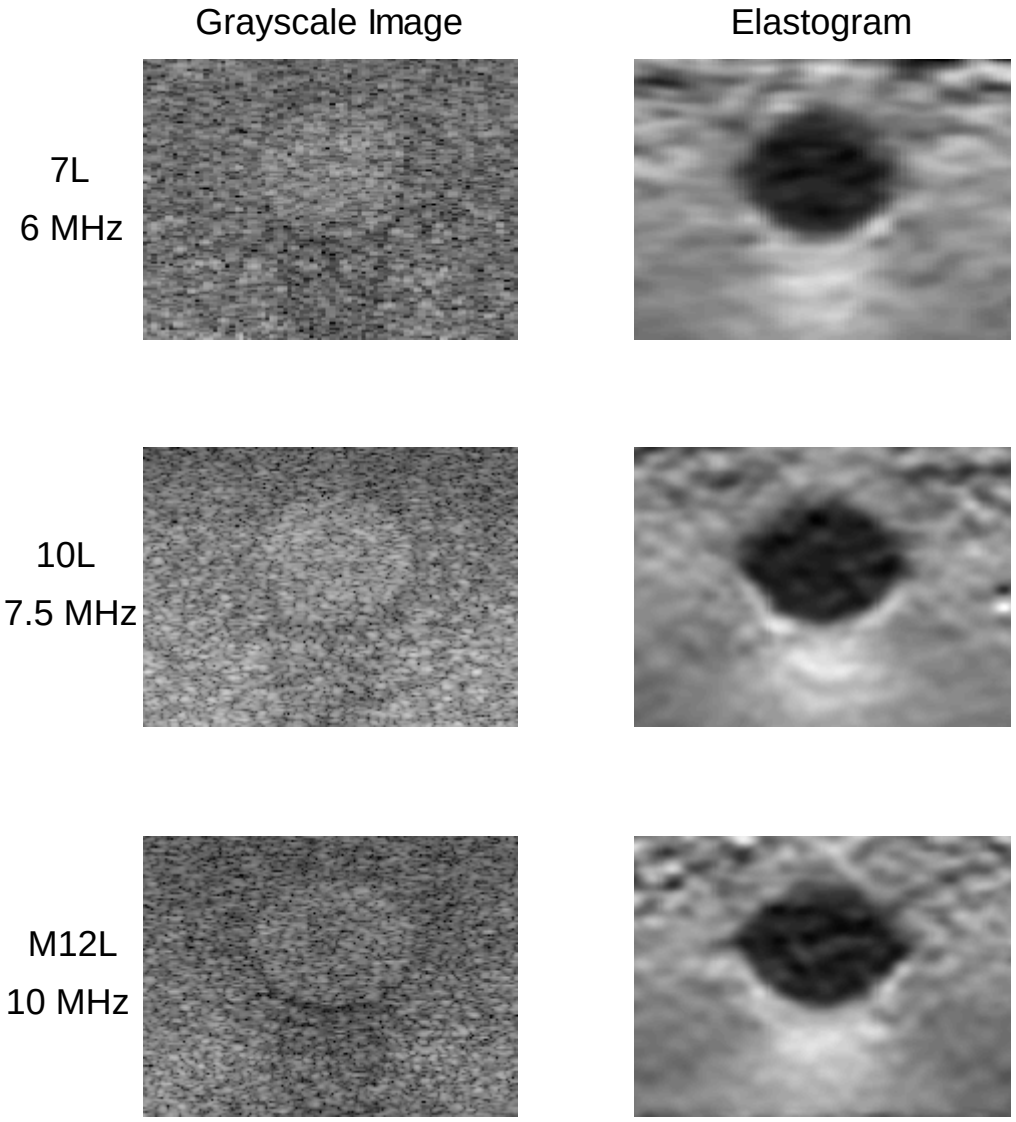

Fig. 4.7: Axial elastogram created from accumulating strain up to 3.5%. Inclusion SNR in the elastogram and mean correlation coefficient values were highest in the images created by the 10L transducer at 7.5 MHz. In the elastogram, stiffer tissue appears "black" and softer tissue appears "white".

Because the 10L transducer at 7.5 MHz produced high correlation coefficient values, little decorrelation due to out-of-plane motion, and high elastographic SNR, all subsequent elasticity scans were conducted using these settings, through the TPX 2.5 mm paddle.

4.4.3. Comparison of Through-Paddle 2D Elastography with Freehand Elastography

Next, the efficacy of through-paddle 2D elastography was compared with 2D freehand elastography. To assess this, mean correlation coefficient values and inclusion SNR as a function of step size were evaluated. Illustrated in Fig. 4.7, at low strain step sizes ($\leq$ 0.5%) correlation coefficients and inclusion SNR are comparable between the imaging techniques. However, as step size increases, through-paddle 2D elastography decorrelates more rapidly than 2D freehand elastography. Additionally, inclusion SNR decreases with increasing step sizes in the through-paddle elastograms, whereas it increases with increasing step sizes in the freehand elastograms, consistent with previous reports [8]. The elastograms created by each of these imaging techniques at different strains are also illustrated in Fig. 4.8.

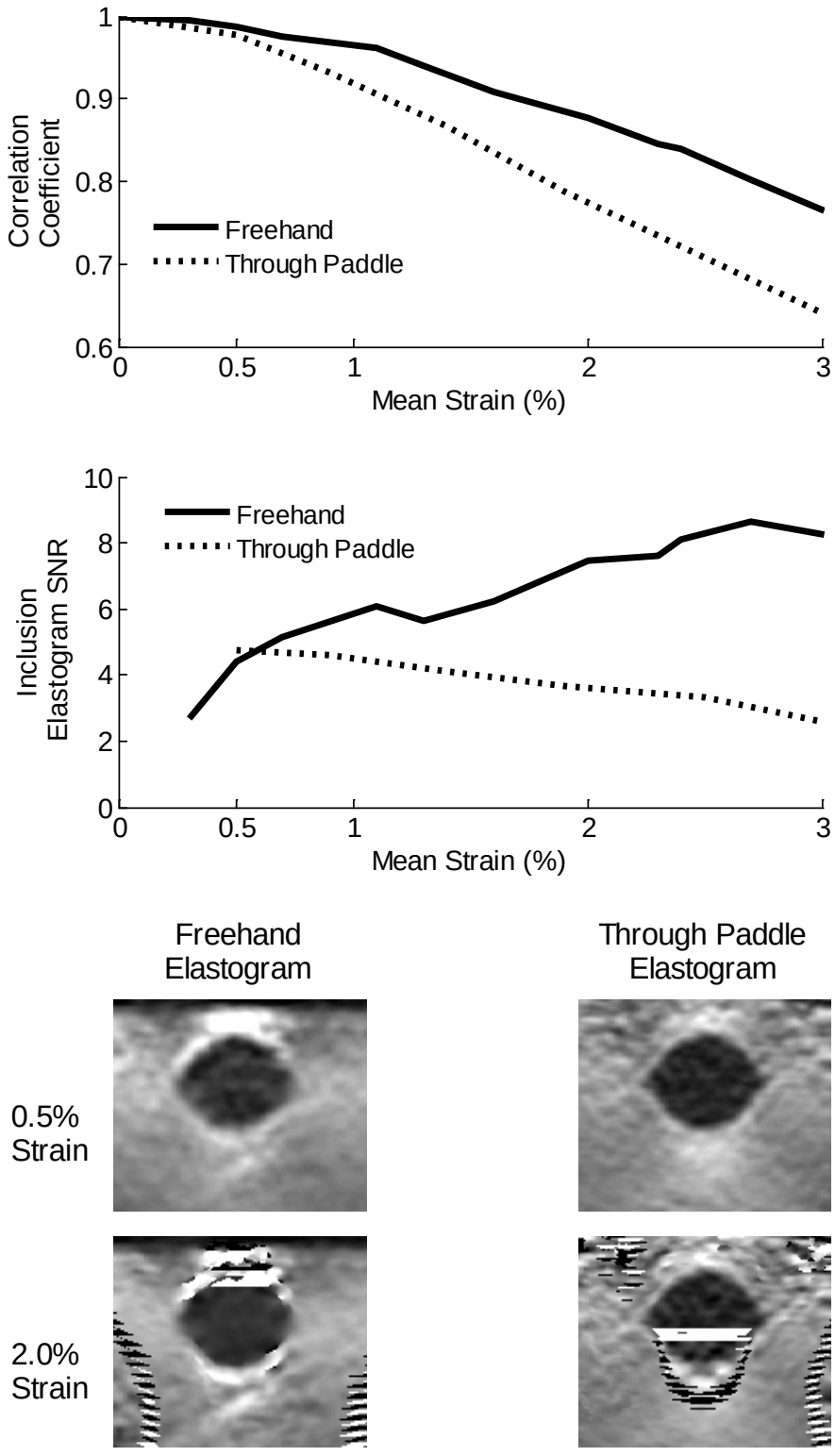

Fig. 4.8: (Top) Correlation coefficient and inclusion SNR as a function of mean strain. At strains $\leq$ 0.5%, these values are comparable between freehand and through-paddle elastography. However, as strain increases, freehand elastography out performs through-paddle elastography. **(Bottom)** Elastograms created by both imaging techniques at low (0.5%) and high (2.0%) strains. Differences in inclusion SNR are clearly visible in these images.

4.4.4. Selection of Slice Number and Size Parameters for 3D Elastography

Based on the promising results for 2D through-paddle elastography, efforts were extended to create high quality 3D through-paddle elastograms.

Two parameters which comprise the 3D volume are slice size and number of elevational slices, which are limited by different constraints. The upper bound on the number of elevational slices is the time it takes to acquire them, and the lower bound is dictated by 3D speckle tracking algorithms which require an elevational spatial distance of two entire speckle spots to be acquired for accurate motion tracking in the elevational direction. The lower bound of the slice size is the smallest distance the stepper motors can travel reliably and the upper limit is 50% of the elevational beamwidth, as required by Nyquist sampling requirements. Ideally, the upper limit of both parameters should be chosen so the largest 3D volume can be acquired.

The elevational beamwidth of the 1D array in this study was experimentally determined using the full width at half maximum of the autocorrelation function and is 1.2 mm. Slice sizes of 0.6 mm, though nominally Nyquist sampled, did not produce optimal elastographic results, but slice sizes of 33% of the beamwidth (0.4 mm) did [9]. Because additionally decreasing the elevational slice size did not improve 3D results, and it was desirable to cover as large of a 3D volume as possible, 0.4 mm slice sizes were used for all subsequent experiments.

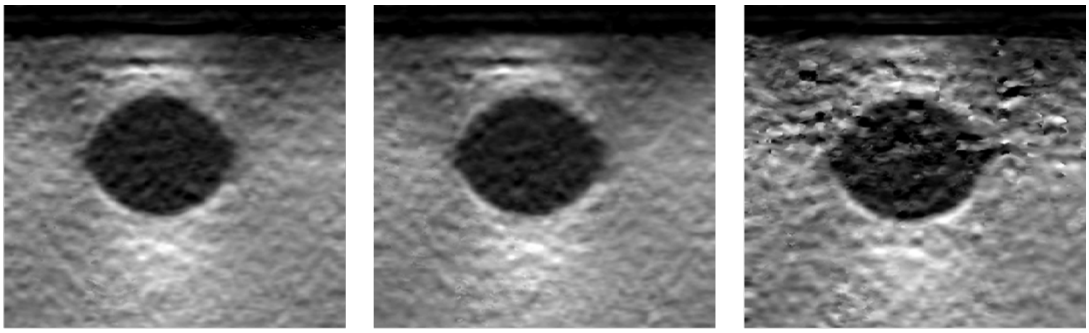

Fig. 4.9: Center slice of 3D elastogram acquired at a 0.5% strain step at **a)** 0.2 mm slice size (17% of the elevational beamwidth), **b)** 0.4 mm slice size (33% of the elevational beamwidth), and **c)** 0.6 mm slice size (50% of the elevational beamwidth). Though nominally Nyquist sampled, the 0.6 mm elevational slice size produces artifacts in the elastogram not seen in the other images. No SNR improvement was observed using slice size of 0.2 mm versus 0.4 mm, and it is desirable to acquire as large of a 3D volume as possible, so all subsequent experiments used the 0.4 mm slice size.

Similarly, the lower bound of the number of elevational slices at a 0.4 mm step size is 11 to ensure that three speckle spots (corresponding to 3.6 mm) are covered. To determine the upper bound on the number of elevational slices, an experiment was conducted to assess the greatest speed which the transducer could be translated without reducing elastogram SNR due to motor vibrations. A 3D volume was collected over 2.5% of axial compression using 11 slices spaced 0.4 mm apart at stepper motor speeds varying between 0 and 5 mm/sec. A speed of "0" corresponded to static data acquisition - pausing the compression while externally triggering RF frames. As expected, as stepper motor speed increased, SNR in the resulting elastograms diminished due to motor-induced vibrations at the greater speeds. However, at a stepper motor speed of 0 mm/sec (equivalent to "static" compression: pausing compression while frames are acquired), the 55 RF frames required for 3D elastography take 60 seconds to acquire, much too long for a subject under compression. A more manageable time is < 15 sec for data acquisition. By compressing the breast at 2.5 mm/sec and decompressing at 10 mm/sec, 11 slices (corresponding to 4.4 mm elevational distance) and 5 axial steps (corresponding to 1.25

mm compression) for a total of 55 frames could be acquired over 13.7 sec. Thus, the upper bound on the number of elevational slices was also 11 slices, and all subsequent experiments used this value.

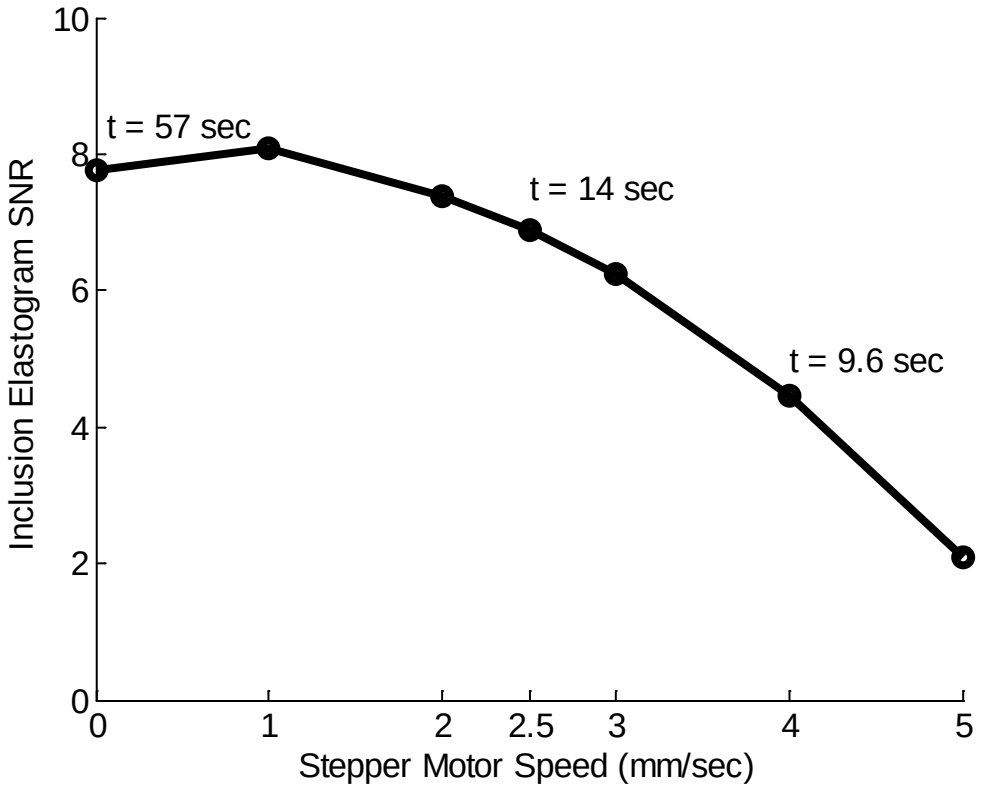

Fig. 4.10: Elastogram SNR as a function of stepper motor speed for a total of 2.5% axial compressions over 11 elevational slices with a 0.4 mm slice size. SNR decreases with increased speed due to increased motor vibrations. Imaging at 2.5 mm/sec limits 3D data acquisition times to 14 sec under these conditions, which is fast enough to acquire data over a consistent subject breathing pattern while maintaining high SNR.

4.4.5. Evaluation of System Robustness to Determine Scan Technique for 3D Elastography

System robustness was evaluated next to determine the severity of the mechanical backlash and determine the best 3D scanning strategy. The mechanical precision in both axial and elevational directions is approximately the same, as expected, and quite small:

backlash measured less than 1.1 μm for 8 mm of travel in either direction, corresponding to $\rho = 0.998$.

A "baseline" 3D raster scan over 11 slices exhibited elevational displacement of 19.3 μm, corresponding to 0.4% backlash for the total 4.4 mm traveled ($\rho = 0.984$). This is slightly greater than multiplying a backlash of 1.1 μm times 11 slices, suggesting that backlash is aggravated as the transducer accelerates and decelerates. Experiments to "overshoot" the full elevational distance and later correlate the middle slices did not alleviate this backlash. Though this backlash is extremely small, it can be circumvented by imaging in the axial mode ($\rho = 1.00$ for an axial baseline scan) rather than raster or alternating raster, where the backlash would be further compounded.

Before axial scanning was implemented, creep during a scan was investigated. A phantom, compressed 8.5% axial strain in 15 compression steps of 0.5-0.6% each, demonstrated that 50 msec were required after this compression for the phantom to return to its original state ($\rho = 0.997$). Note that the 0.003 reduction in the correlation coefficient is actually due to the small mechanical backlash (5μm corresponding to 0.2% of the total compression distance). This rubber phantom is springier than tissue and does not contain fluids and thus creep may be a larger concern *in vivo.* Additionally breast tissue is heterogeneous which also may affect creep. However, these experiments provide a reasonable starting point for what to expect *in vivo.* Thus, in all human subject scans, the breast was compressed to maximum 2.5% strain and a 300 msec waiting period between compressions was applied to minimize tissue creep effects.

Though alternating raster scanning reduced data acquisition times by a factor of two compared with axial and raster scanning, it was most susceptive to mechanical

backlash and thus should not be employed in future experiments. In contrast, data acquisition time with axial and raster scanning was approximately the same. However, for a 3D scan over 5 axial steps (corresponding to 2.5 mm compression) and 11 elevational slices (corresponding to 4.4 mm distance), axial scanning produced less backlash than raster mainly because the transducer traveled further in the elevational direction for this type of scan. The preferred scanning technique would provide the best combination of speed and minimal backlash, and this was determined to be axial scanning.

4.4.6. Comparison of 2D and 3D Through-Paddle Elastography

Image quality between 3D and 2D through-paddle elastography was compared when the previously determined best case imaging strategies were employed. Recall that all 2D data were extracted from the central slice of the 3D volume and analyzed using conventional 2D speckle tracking algorithms so direct comparisons could be made.

The mean correlation coefficient as a function of strain was analyzed in the 2D and 3D case (Fig 4.11). For small strains (< 1%), the correlation coefficient is approximately the same because there is very little out of plane motion at these strains. In fact, the correlation coefficient derived from 3D elastography is slightly lower due to mechanical backlash. However, as strain step size increases, the 3D correlation coefficient decreases less quickly than the 2D correlation coefficient by tracking out-of-plane motion contributing to the decorrelation in the 2D case. The amount of elevational motion calculated from these experiments was also quantified as a function of strain (Fig. 4.11, middle). Surprisingly, there is little out of plane motion when conducting through-

paddle elastography (< 0.4 mm for a 3% strain step). Comparing decorrelation as a function of elevational translation (Fig. 4.11, bottom) with the calculated elevational motion, it is evident that the amount of elevational motion must be approximately 0.35 mm before it begins to strongly affect correlation coefficients in the 2D case. However, this degree of elevational motion does not occur until a 3% strain step, which corresponds to very low correlation coefficients ($\rho = 0.7$) in the 3D case. Thus, it is unlikely that a 3% strain step would produce high quality elastograms, even with 3D imaging.

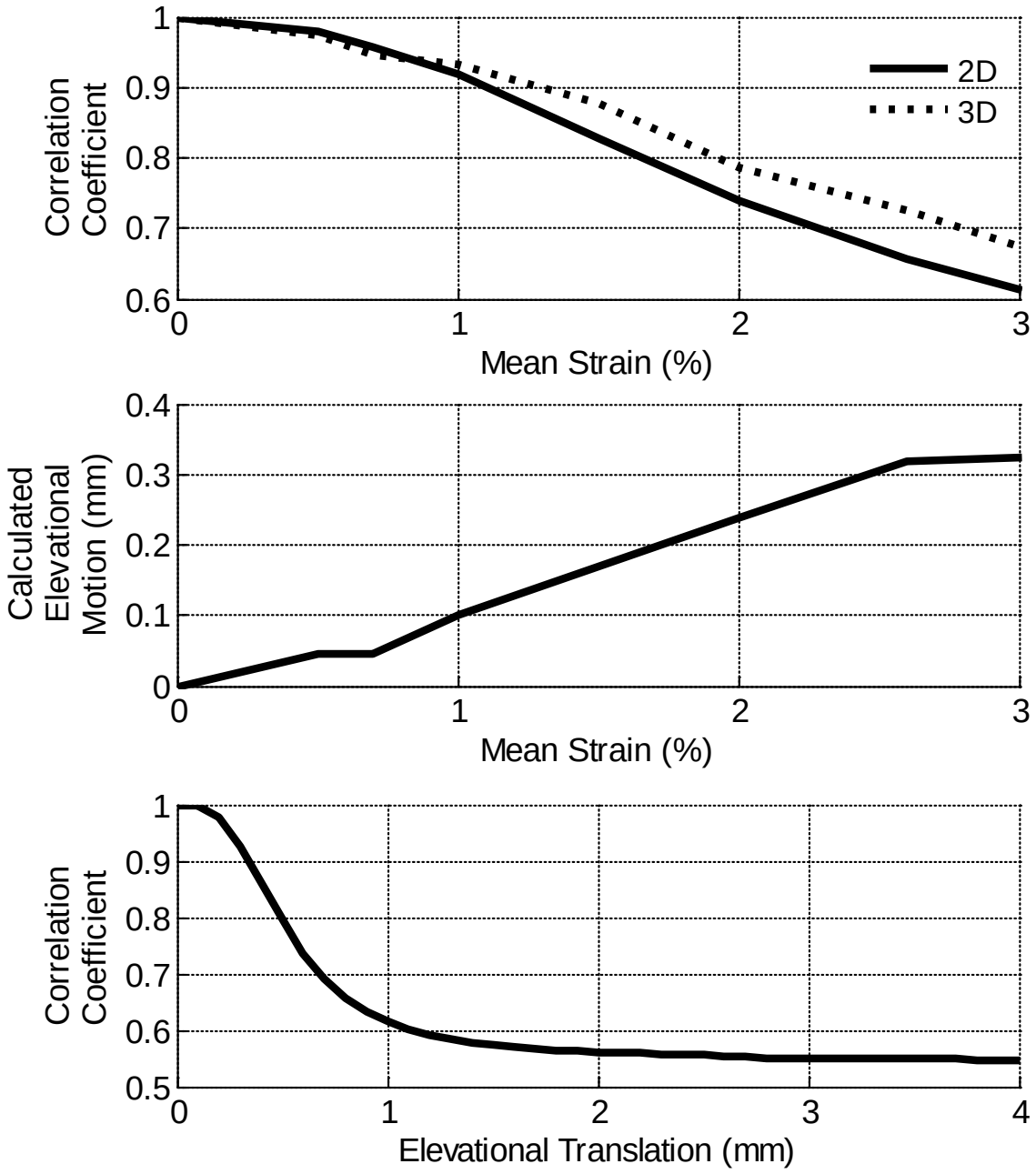

Fig 4.11: (Top) Correlation coefficient as a function of strain step size for 2D and 3D elastography. At low strains (< 1%), correlation coefficients are approximately the same, but as strain increases, the 3D case decorrelates less quickly than the 2D case. **(Middle)** Calculated elevational motion as a function of strain step size. This graph illustrates that at least 0.1 mm elevational motion must occur before 3D correlation coefficients are higher than 2D correlation coefficients. **(Bottom)** Correlation coefficient as a function of elevational translation for the 10L transducer at 7.5 MHz used in all the experiments. Strong decorrelation ($\rho = 0.9$) due to out of plane motion does not occur until there is at least 0.35 mm elevational translation.

Elastogram SNR was also compared between the 2D and 3D cases as a function of strain step size. As observed previously, 2D strain SNR decreases with increasing strain because the paddle slowly pushes the lesion out of plane. However, using 3D elastography increases the SNR with strain up to 3% strain, at which point in-plane decorrelation dominates SNR values (Fig. 4.12). Unfortunately, as observed in the elastograms in Fig. 4.12, the strain step which corresponds to a large jump in strain SNR with 3D elastography also produces small peakhop artifacts in the region of the lesion. As strain increases, the amount of artifacts in the elastogram increases much more in the 2D case than in the 3D (Fig. 4.12, bottom). This is consistent with reports by Chen et al. (2006): tracking elevational motion improves the quality of in-plane strain estimates [5].

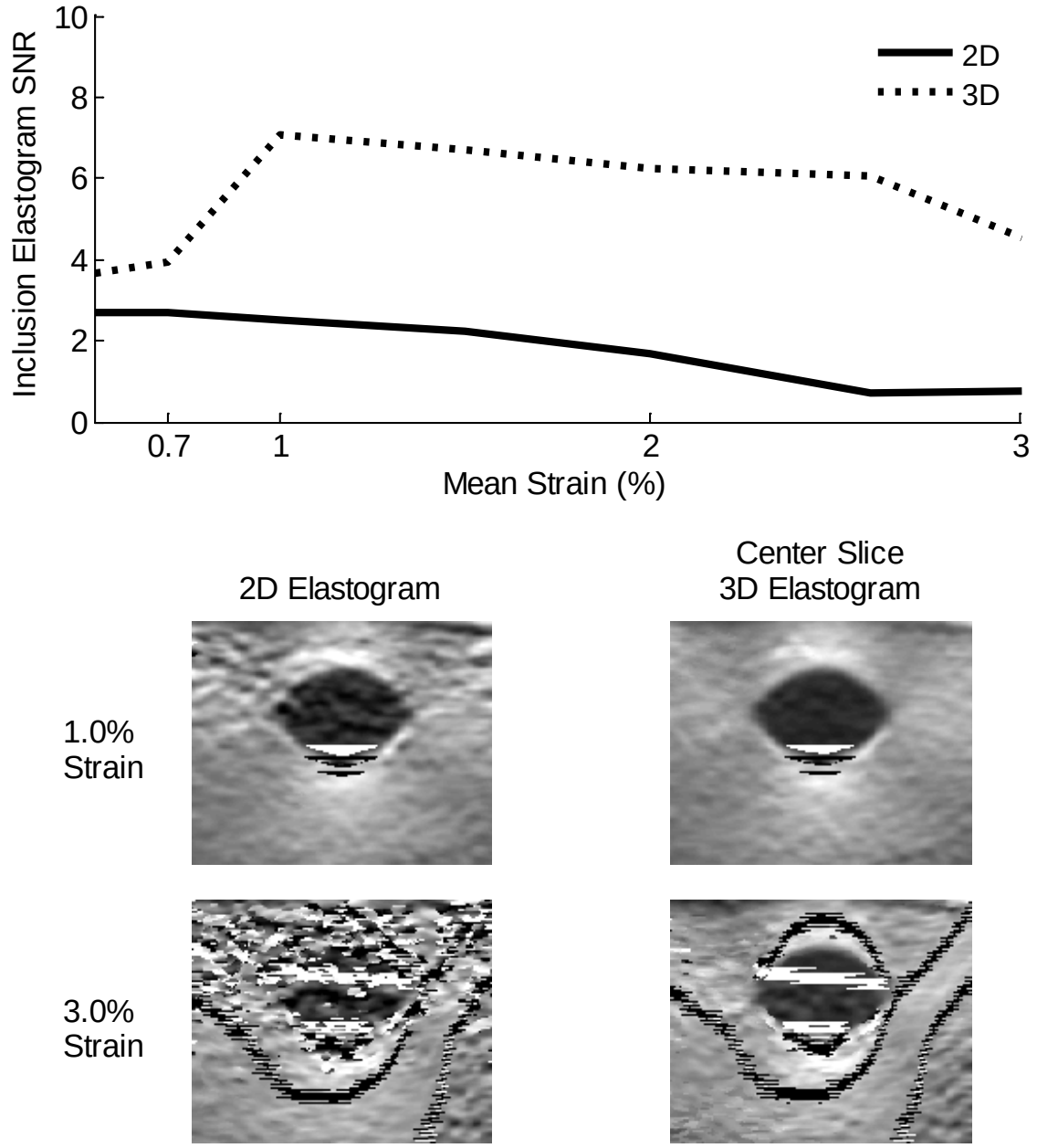

Fig. 4.12: (Top) Elastogram SNR as a function of strain step size for 2D and 3D elastography. Though SNR decrease with step size in the 2D case, it increases with step size in 3D. **(Bottom)** 2D and 3D elastograms for 1.0% and 3.0% strain steps. The greatest SNR improvements with 3D elastography begin at the 1.0% strain step size, though, small artifacts are created in the resulting elastograms. As step size further increases, peakhop artifacts in the center-slice 3D elastograms are much less apparent than in their 2D analogues.

Though the greatest improvements in SNR with 3D elastography compared with 2D elastography occurred at step sizes $\geq$ 1%, these step sizes also produce peakhop

artifacts which might be further aggravated by the low sonographic SNR's observed in breast tissue. Thus, initial efforts to conduct *in vivo* 3D elastography will use step sizes of 0.5% to realize the increased elastographic SNR observed with 3D elastography yet keep peakhop artifacts at a minimum in resulting elastograms. As seen in Fig. 4.13, even with a 0.5% step size, SNR improvements with 3D elastography are visible in elastograms.

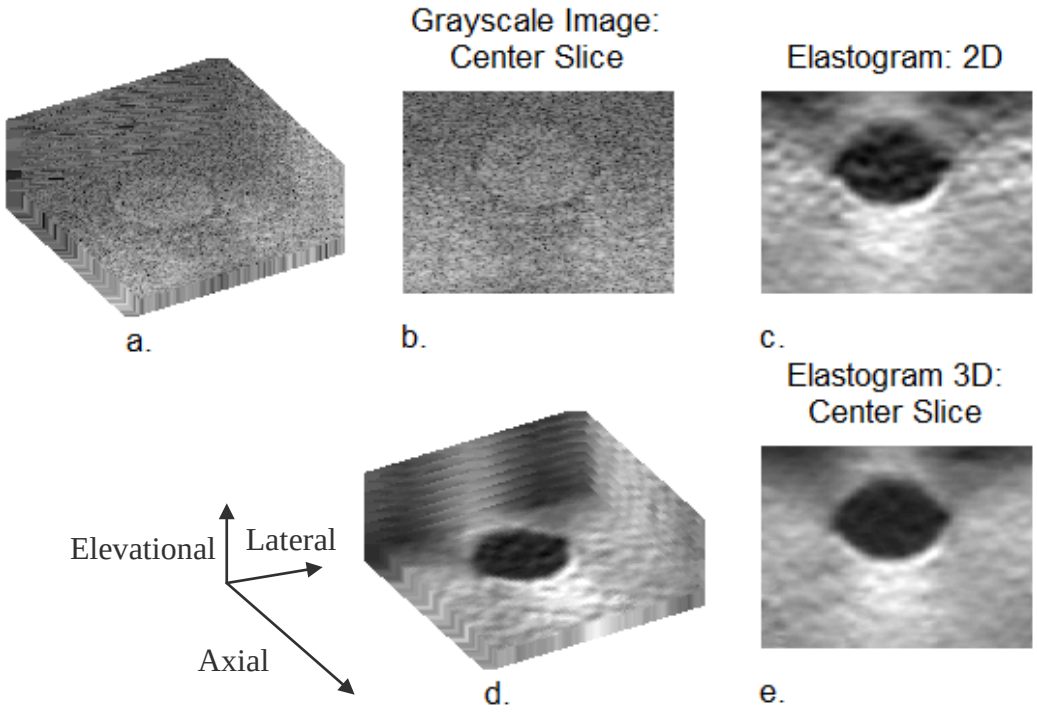

Fig. 4.13: **a)** Grayscale ultrasound volume (40 mm x 39 mm x 4.4 mm, axial x lateral x elevational) of tissue-mimicking phantom imaged with 3D elastography; **b)** center slice of 3D volume from **a)**; **c)** 2D elastogram analyzed from center slice of volume; **d)** elastogram volume analyzed using 3D elastography; **e)** center slice of elastogram volume from **d)**. Improvements in elastographic SNR are clear visible in the 3D center-slice elastogram compared with it's 2D analogue, even at a strain step size of 0.5%.

4.4.7. Summary of 2D and 3D Through-Paddle Elastography Results

Selecting best case parameters for through-paddle elastography is essential to create high quality elastograms and correlation coefficient images. In 2D, imaging with the 10L transducer at 7.5 MHz through the TPX 2.5 mm paddle produced uniform deformations with little out-of-plane motion, high spatial resolution and high strain SNR.

Thus, these parameters were applied to all 3D experiments. In 3D, axial scanning over 11 elevational slices with 0.4 mm slice size produced high quality elastograms with little mechanical backlash and increased SNR over their 2D analogues. Analysis of these results and their implications for through-paddle breast elastography are discussed in the next section.

4.5. Discussion

4.5.1. 2D Through-Paddle Elastography

Because the paddle is the deformation surface for through-paddle elastography, a more rigid paddle would be expected to produce high quality elasticity images as long as additional signal loss by imaging through the thicker paddle does not cause severe decorrelation. TPX paddles 1.0 and 2.5 mm thick both produced 2D elastogram with no peakhop artifacts and similar SNR_{ε}. Thus, the TPX 2.5 mm paddle was chosen for future experiments because it bowed less than thinner paddles under compression, providing a more uniform deformation surface and because it was the paddle chosen for use in the image registration experiments conducted on the combined ultrasound/digital tomosynthesis mammography system. Similarly, high quality elastograms were created using all transducers and frequencies tested in this study. Ultimately, the 10L transducer at 7.5 MHz was chosen for future experiments because it produced better spatial resolution than the 7L and less attenuation and decorrelation due to elevational motion than the M12L.

Comparing the final elastograms produced when these best case parameters were employed with freehand elastograms, through-paddle elastography caused more

decorrelation as a function of step size than freehand elastography. This could be due to two different effects. First, the lesion was being slowly pushed out of plane during compression, causing decorrelation which was only observed at greater step sizes. Second, refraction through the mammographic paddle would be exacerbated at large step sizes, and may have caused additional decorrelation that was not observed at smaller step sizes. Applications which require larger step sizes may benefit more from freehand elastography than through-paddle elastography. However, it should be noted that the best case 2D freehand results were compared with the 2D through-paddle results in this study, and there were many freehand frames which were retrospectively removed from analysis because of their poor elastogram image quality. In contrast, through-paddle elastography produced consistent frame-to-frame results, given a constant step size.

In summary, high quality 2D elastograms and correlation coefficient images can be created with through-paddle elastography using strain step sizes of approximately 0.5%. Additionally, the benefits of conducting through-paddle elastography *in vivo* in the same orientation and at essentially the same time as the clinical tomogram and sonogram may outweigh these losses in image quality at greater step sizes. These promising preliminary results encouraged investigation of 3D elastography with the combined system.

4.5.2. 3D Through-Paddle Elastography

With the ultimate goal of applying through-paddle elastography *in vivo*, 3D scanning parameters were guided by time constraints and bounds on speckle tracking requirements. Ultimately, imaging at 2.5 mm/sec over 11 elevational slices at 0.4 mm

slice size, using axial scanning, and up to 2.5% axial compression produced high quality elastograms quickly enough that the scanning could be conducted within a consistent breathing pattern. Examining the quality of the resulting correlation coefficients and elastograms against their 2D analogues, mean correlation coefficients from 3D elastography were higher for a given step size than their 2D analogues at strains $\geq$ 1%. This was also the smallest step size that corresponded to a large increase in SNR in 3D elastograms compared with 2D elastograms, because 1% strain step was the minimum axial compression required to induce enough out-of-plane motion (0.1 mm) to cause decorrelation in 2D which would be successfully tracked in 3D. However, even in phantom experiments, this step size produced minor peakhop artifacts in the strain images. Though these could be retrospectively removed, these artifacts are likely to be exacerbated when imaging *in vivo* because ultrasound SNR in breast tissue is low. SNR improvements from 3D elastography at 0.5% strain steps (35% improvement over 2D), though not optimal, were visually noticeable in elastograms and thus these initial parameters will be applied to explore the fidelity of 3D elastography *in vivo*.

4.6. Conclusions

The feasibility of through-paddle elastography has been successfully demonstrated in a tissue-mimicking phantom in both two dimensions and three dimensions. Imaging through the TPX 2.5 mm mammographic paddle with a linear 1D array (10L) at 7.5 MHz produced high correlation coefficients and axial elastograms with high SNR. Through-paddle elastography produced comparable results compared with best case 2D freehand elastography at low strains ($\leq$ 0.5%). This is likely the best strain step to image breast tissue *in vivo* using 2D elastography because ultrasound SNR in

breast tissue is quite low, and it is likely that imaging at strain steps greater than 0.5% would create peakhop artifacts in strain images and extra decorrelation. Extending this technique a 3D volume extending 4.4 mm elevationally (corresponding to 11 elevational slices), produced axial elastograms with increased correlation coefficients and elastographic SNR 35%-750% greater than their 2D analogues when mechanical backlash was minimized and scan times were restricted to the length of a subject's breathold. Future work should explore implementation of these methods on other phantoms, which may mimic the elastic properties of tissue more closely than the ATS phantom used in these experiments [12-13]. However, these early successes indicate that using through-paddle elastography with the combined system can create high quality elastograms which might aid in the characterization of breast lesions.

4.7. References

[1] Hall TJ, Zhu Y, Spalding CS. In vivo real-time freehand palpation imaging. Ultras Med Biol 2003; 29:427-435.

[2] Doyley MM, Bamber JC, Fuechsel F, Bush N. A freehand elastograhic imaging approach for clinical breast imaging: system development and performance evaluation. Ultras Med Biol, 2001; 27: 1347-1357.

[3] Hiltawsky K, Kruger M, Starke C, Heuser L, Emert H, Jensen A. Freehand ultrasound elastography of breast lesions: clinical results. Ultras Med Biol 2001; 27: 1461-1469.

[4] Lindop JE, Treece GM, Gee AH, Prager RW. 3D elastography using freehand ultrasound. Ultras Med Biol 2006; 32(4):529-45.

[5] Chen X, Xie H, Erkamp R, et al. 3-D correlation-based speckle tracking. Ultrason Imaging 2005; 27(1):21-36.

[6] Konofagou EE and Ophir J. Precision estimation and imaging of normal and shear components of the 3D strain tensor in elastography. Phys Med Biol 2000; 45: 1553–1563.

[7] Kapur, P. Carson, J. Eberhard, M et. al. Combination of digital mammography with semi-automated 3D breast ultrasound. Technol Cancer Res 2004; 3(4): 325-334.

[8] Lubinski M, Emelianov S, O'Donnell M. Speckle Tracking Methods for Ultrasonic Elasticity Imaging Using Short-Time Correlation. IEEE Trans Ultrason Ferroelectr Freq Control 1999; 46:82-96.

[9] Kaluzynski K, Chen X, Emelianov SY, Skovoroda AR, O'Donnell M. Strain rate imaging using two-dimensional speckle tracking. IEEE Trans Ultrason Ferroelectr Freq Control 2001; 48:1111-1123.

[10] Booi RC, O'Donnell M, Knoth MM, Xie H, Hall AL, Rubin JM, Carson PL. "3D breast elastography with a combined ultrasound/tomography system." Proceedings of the 2006 IEEE Ultrasonics Symposium; p. 2056-2059.

[11] Booi RC, Carson PL, Erkamp RQ, Xie H, Kapur A, LeCarpentier GL, Roubidoux MA, Fowlkes JB, O'Donnell M. "Applying *in vitro* elasticity imaging results to optimize *in vivo* breast lesion characterization using a combined 3D ultrasound/digital x-ray system." Proceedings of the 2005 IEEE Ultrasonics Symposium; p. 727-730.

[12] Browne JE, Ramnarine KV, Watson AJ, Hoskins PR. Assessment of the acoustic properties of common tissue-mimicking test phantoms. Ultras Med Biol 2003; 29(7): 1053-1060.

[13] Madsen EL, Hobson MA, Frank GR, Shi H, Jiang J, Hall TJ, Varghese T, Doyley MM, Waver JB. Anthromorphic breast phantoms for testing elastography systems. Ultras Med Biol 2006; 32(6): 857-874.

CHAPTER 5

IN VIVO ELASTOGRAPHY FOR IMPROVED BREAST MASS CHARACTERIZATION

5.1. Chapter Overview

Current limitations in diagnostic breast imaging provide the motivation to investigate whether elastography can improve breast mass characterization. The collection of *in vivo* studies in this dissertation tested the role of elastography in conjunction with different ultrasound modes and digital tomosynthesis mammography, all conducted in the same imaging view, in characterizing breast masses. These studies can be categorized as follows: 1) evaluation of the effects of subject breathing motion and breast stability on 2D and 3D through-paddle breast elastography, 2) analysis of the differential correlation coefficient in breast masses for improved cystic/solid mass discrimination, and 3) assessment of the clinical utility of breast elastography as part of a combined x-ray tomography/3D ultrasound system, evaluated in a reader study performed by 2 radiologists. Portions of the work presented in this chapter have been published in [39] and [40].

5.2. Introduction

In the current diagnostic breast imaging environment, standard clinical practice includes mammography, occasionally supplemented by sonography, to characterize

breast masses. This approach yields at least 5% false-negative rates and 70-90% of biopsies are benign [1-3]. In dense breasts, the false negative rates in routine practice are 25-40% using screening mammography alone [19]. These shortcomings drive the main clinical goal of this dissertation - to improve breast lesion characterization with through-paddle elastography in conjunction with a combined tomosynthesis/ultrasound system. Freehand elastography has demonstrated potential for improved breast mass characterization, and the efficacy of the technique may be maximized when conducted in the same imaging view as x-ray tomosynthesis and ultrasound images. However, one potential limitation of through-paddle elastography is that chest wall and cardiac motion could increase decorrelation and produce artifacts in the resulting strain images. Therefore, one goal of this study was to evaluate how chest wall motion affects correlation coefficient values and strain images in elastography and to reduce these effects to realize the full potential of this technique.

One noteworthy original contribution of this thesis is its efforts to characterize breast cysts more reliably with elastography than with tomography and ultrasound alone. Breast ultrasound is well respected for its ability to differentiate simple cysts from solid lesions with 98-100% accuracy [4-7]. For a cyst to be characterized as “simple”, it must exhibit all four of the following criteria: anechoic, well circumscribed, imperceptible wall, and posterior acoustic enhancement [5, 8-10]. Terminology of cysts which meet some but not all of these criteria varies, but includes complicated cysts, complex cysts, cluttered microcysts, cystic lesions with a thick (perceptible) wall and/or thick (> 0.5 mm) septations > 50% cystic, and predominantly solid lesions with eccentric cystic foci [5, 9-11]. Mendelsen et al. describe a complicated cyst as containing homogeneous low-

level echoes that otherwise meet the criteria for a simple cyst, but state that they can also be circumscribed with imperceptible walls and fluid-debris levels [11]. Venta et al. groups all non-simple cysts into the category of "complex", and identifies complex cysts as those which have internal echoes, thin septations, an intracystic lesion, perceptible wall, or the absence of definitive posterior-wall enhancement [10]. Stavros also identifies any cyst not meeting all the criteria of a simple cyst as "complex" [9]. However, Berg et al. reserves the identification of a "complex cyst" as those cysts which contain some discrete solid component, consistent with the American College of Radiology (ACR) ultrasound breast imaging reporting and data system (BI-RADS) lexicon [8, 12]. The ACR ultrasound BI-RADS system also standardizes complicated cysts as containing homogeneous low-level internal echoes and fluid-fluid or fluid-debris levels which can shift as the patient's position [12]. The cysts analyzed in this preliminary study will be termed "non-simple" because they only met some or none of the requirements for simple cysts, but did not have solid components.

Non-simple cysts are common, and the percentage of cysts being classified as non-simple is increasing [9-10, 13-14]. In a recent study, Berg et al. classified only 11% (16 of 150) of cystic lesions as "simple" [8]. This increase in clinically observed non-simple cysts is at least partly due to the use of high quality ultrasound scanners which can both image small particulate matter and create artifacts, including reverberations, clutter, and sidelobes, in the cysts [9-10, 13-14]. An *in vitro* study by Helvie et al reported that cyst fluid almost always exhibited internal echoes when imaged with high quality equipment, demonstrating that cysts are rarely anechoic and thus rarely simple, by

definition [15]. Therefore, finding a reliable imaging method to differentiate benign non-simple cysts from solid lesions is of great clinical importance.

Variability exists in how non-simple cysts should be managed, with management options including 6-month or 1-year imaging follow-up, aspiration, aspiration with possible core biopsy, and excisional biopsy [10-11]. Simple cysts are easily classified as benign using sonography, and often can be managed with imaging follow-up, though if the cyst is tender or palpable, aspiration may occur [5, 8, 10]. In contrast, management of non-simple cysts varies according to sonographic findings (many have suspicious sonographic appearances which can overlap with appearances of solid masses), patient risk factors for breast cancer, and patient anxiety [10, 16]. Berg et al. reported a malignancy rate of 23% (18 of 79) for the complex cysts they imaged which contained some degree of discrete solid components, stating that biopsy would be required for these lesions [8]. In contrast, the National Comprehensive Cancer Network (NCCN) reports that aspiration is the standard of care for non-simple cysts which do not contain solid components [17]. Reports of cysts which do not meet the strict criteria of simple cysts, but do not have a solid component show very low malignancy rates between 0 – 1.4% (3 of 744 total cysts, or 0.4% on average) [8, 10, 18-20]. This low malignancy rate reveals that non-simple cysts with no solid components could be characterized as probably benign and managed with follow-up imaging rather than aspiration or biopsy when accurately identified [8, 10]. It may be possible to circumvent follow-up entirely if these cysts could be characterized with certainty. Because many patients have multiple cysts in each breast, needle aspiration, biopsy, or close follow up cannot be performed on each cyst.

Methods used to improve the characterization of non-simple cysts include decreasing dynamic range, using tissue harmonic imaging, and using spatial compounding [8]. Several groups have reported that the presence of internal echoes in a cyst precludes it from being classified as “simple”, however echoes which surround the anterior of the cyst are usually recognized as reverberations [10]. Spatial compounding has been successfully used to reduce speckle and other noise in cysts, but it can also reduce posterior acoustic enhancement and its benefits decrease with increasing depth [21].

Ultrasound elastography may prove to be a more viable tool to identify internal echoes created by noise and artifacts, as well as fluid-debris and particulate matter. Elastography is a diagnostic method that evaluates the viscoelastic properties of tissue, as changes in tissue elasticity are usually related to an abnormal, pathological process. During breast elastography, a surrogate to manual palpation, tissue is externally deformed to create internal displacements. Displacements are estimated by tracking speckle movement in the ultrasound images before and after compression. The gradient of these displacements in the direction of the compression is then calculated to create an elastogram which displays the relative induced strain in the image region.

Though breast elastography has demonstrated clinical utility in studies by Garra et al. and Hall et al., visualization of cysts in elastograms is often difficult and recent studies attempting to characterize cysts with elastograms have had limited, and sometimes conflicting, results [22-23]. Garra et al. reported easy visualization of only 37% (3 of 8) of cysts in their study, and even when visible, those cysts had ill-defined margins [22]. Garra et al. described three different elastographic patterns in the eight cysts studied: 1) a

darker (stiffer) area with a brighter (softer) center, 2) a uniformly dark area, and 3) an area with both bright and dark regions [22]. Using a Siemens ultrasound scanner, Barr reported that both simple and complicated cysts appeared dark (stiffer) in elastograms with a brighter, "bulls-eye" appearance in the middle of the cyst [24]. Hall et al. described that because cysts rapidly decorrelate, they can appear relatively stiff or soft in elastograms, often depending on how much strain is applied [23]. In a study conducted by Lyshchik et al., 5 of 6 cysts imaged in the thyroid produced considerable noise in their resulting elastograms, preventing the authors from identifying any elastographic characteristics of these lesions [25]. From these findings it is evident that cysts can demonstrate a variety of appearances in elastograms, depending on the ultrasound scanner used, percent compression and pre-compression, and type of signal processing.

In response to this problem, our study evaluated whether the high decorrelation rate initially observed by Hall et al. associated with cysts in cross-correlation imaging could be used directly to distinguish cysts from solid masses. Because most cysts are primarily composed of fluid, random noise, reverberations, sidelobes, and clutter they decorrelate quickly when compressed for elastography. Therefore, cysts may be consistently and clearly visible in the correlation coefficient image, providing direct diagnostic information that cannot be achieved by looking at the appearance of cysts on elastograms. Because the elastogram cannot be reliably used in cyst characterization, the correlation coefficient derived from data acquired for elastography becomes an increasingly valuable tool in differentiating cysts from solid masses.

This study aims to exploit the rapid decorrelation of non-simple cysts observed in elastography as a way to differentiate them from solid breast lesions. Because cysts are

filled with fluid, they contain little speckle which can be tracked for elastography. Thus, the correlation coefficient in that region will be markedly lower than in the rest of the tissue. One caveat is that signal from surrounding tissue, including reverberations, clutter, and sidelobes can contribute to signal in the cyst, increasing the correlation coefficient. Additionally, some breast cancers and fibroadenomas are highly hypoechoic, and the signal-to-noise ratio (SNR) in breasts is often low. This could cause these lesions to decorrelate as quickly as non-simple cysts. The extent to which non-simple cysts decorrelate relative to surrounding tissue in comparison with other breast lesions is explored. Whether improved cyst/solid mass differentiation could impact clinical management of non-simple cysts by allowing follow-up imaging rather than intervention is discussed.

5.3. Methods

5.3.1. Human Subject Selection and Recruitment

This study was approved by the institutional review board and informed consent was obtained on all human subjects. The study was compliant with the Health Insurance Portability and Accountability Act. Subject confidentiality was protected at all times.

For the initial 2D breathing motion study, 7 healthy volunteers were recruited over a 2 month period (02/01/2005 – 04/01/2005). The remaining *in vivo* studies were conducted on different subsets of 28 consecutive human subjects recruited in two groups over a 15 month period (02/01/2006 to 05/01/2007). The first group (N=18) were imaged immediately before core biopsy with lesions classified as BI-RADS assessment category 4 or 5 [12]. The second group (N=10) were subjects with known, benign lesions,

diagnosed from previous biopsies (solid lesions) or previous clinical mammograms/ultrasounds (cysts). Participants in this study were required to have had previous clinical mammograms and all solid lesions were pathologically diagnosed. After imaging, 8 subjects were excluded from final analysis due to limitations introduced by our imaging system or post-processing technique, described at the end of this section. The final 20 lesions comprising the case group for differential correlation coefficient analysis and elastography reader study were characterized as 8 cysts, 4 cancers, and 8 fibroadenomas. Two cancers were diagnosed as invasive ductal carcinomas and two were lobular carcinomas. All cysts were classified as benign and 63% (5 of 8) were managed using previous mammogram(s) stability with 12-month imaging follow-ups while 37% (3 of 8) were aspirated. No cysts in this study contained solid components. Cysts were classified as “non-simple” based on their sonographic appearance at the time of imaging using the definitions of simple cysts described in section 5.2. Table 5.1 lists the sonographic features of these cysts.

Table 5.1: Sonographic characteristics exhibited by the non-simple cysts analyzed in this study (marked with an "X"). Cysts must exhibit all four characteristics to be classified "simple".

Cyst	*Anechoic*	*Well-circumscribed*	*Imperceptible wall*	*Posterior acoustic enhancement*
1		X	X	X
2				
3				
4		X		X
5		X		
6		X	X	X
7		X		
8		X		X

Of these 20 subjects, 15 (6 cysts, 5 fibroadenomas, 4 cancers) were imaged with tomosynthesis and through-paddle ultrasound in addition to elastography. Our study criteria limited this research tomosynthesis imaging to subjects older than 40 years, which excluded 3 of the subjects. The remaining two subjects declined the tomosynthesis component of this study because they did not want to be subjected to additional radiation (~1.5 times that of a single view mammogram).

A subset of 9 subjects with masses (4 cysts, 4 fibroadenomas, 1 cancer) was imaged with 3D elastography in this study. The number was limited by time and imaging constraints. Additionally, one healthy volunteer was imaged on two occasions 9 months apart and one subject with a fibroadenoma was imaged over a region of healthy tissue to test the 3D data acquisition process. In total, 12 subjects were imaged with 3D elastography for this study.

A summary of the breast masses exhibited by human subjects analyzed in each component of this study is provided in Table 5.2.

Table 5.2: Summary of human subjects and their corresponding breast masses analyzed in each study.

Mass	***Breathing Motion***	***3D Elastography***	***Differential Correlation Coefficient***	***Reader Study***
Cyst	0	4	8	8
Fibroadenoma	0	4	8	8
Cancer	0	1	4	4
None	7	3	0	0
Total	7	12	20	20

5.3.2. Exclusion Criteria for Human Subjects in this Dissertation

Due to limitations introduced by our imaging methods and post-processing techniques, as well as pathology results which were only available after recruitment for this study, some examinations were retrospectively excluded from analysis. Lesions deeper than 4 cm when compressed were excluded because the SNR at those depths with this transducer is too low for the speckle tracking algorithms to work reliably (N=1). Lesions compressed to < 1% total additional strain during the exam were also excluded from analysis because the deformation was too small (N=2) [26]. Finally, because the goal of this research is to assess differences between the most common breast masses, subjects whose pathology results did not characterize their lesions as a fibroadenoma, cancer, or cyst were excluded from final analysis (N=5).

5.3.3. Experimental Setup

The experimental setup for elastography data acquisition through a mammographic paddle has been described in detail in Chapter 4. The phantom studies from that chapter were designed to mimic the requirements for *in vivo* elastography. Thus, the experimental setup for 2D and 3D elastography remains the same for *in vivo* studies as for phantom studies, as intended. The integration of elastography as part of the larger study to combine x-ray/tomosynthesis and through-paddle ultrasound is described below. Specific details of the elastography data collection techniques for each component in this study are provided later in this section.

All human subject scans proceeded in the following way. Subjects were seated throughout the entire exam. A radiologist with 16 years of breast imaging experience initially located the lesions by manually scanning the transducer over the non-compressed breast and obtaining a 3D volume over the region-of-interest (ROI) using grayscale sonographic imaging. (This scan was later used to assess the sonographic appearances of the cysts in the differential correlation coefficient study.) After initial localization, the subject's breast was compressed in the combined x-ray tomosynthesis/ultrasound system in the cranial-caudal (CC) position and hairspray (Got2BGlued, Schwarzkopf & Henkel, Irvine, CA, USA) was spread between the breast and the paddle, serving the dual purpose of coupling between the paddle and breast with minimal signal degradation and stabilizing the breast during the scans [27]. Next, 21 x-ray projections, corresponding to 60 degrees rotation over 8 sec, were acquired for the 3D x-ray (tomosynthesis) reconstruction. Water was then added to the mammographic paddle to acoustically couple the ultrasound transducer to the paddle and the ultrasound transducer was scanned across

the entire breast to produce a full-field 3D ultrasound volume of the breast. Total acquisition time for the ultrasound scan was 45 seconds per sweep, and 1-3 sweeps were performed on each subject, depending on the size of the breast.

All elastography experiments were conducted on the stand alone mammography-mimicking unit built by University of Michigan researchers from components of earlier General Electric Global Research Center prototypes. Unlike the combined system, the upper and lower compression paddles on the stand alone unit could be controlled precisely with stepper motor control. Thus, after tomosynthesis and ultrasound images were collected, subjects were moved to the stand alone unit for elastography data acquisition. Subject breasts were compressed in the same manner as in the combined system to allow direct comparison of results. Extra attention was paid to the amount of preload, or pre-compression, applied to the breast directly before elasticity scans. Preload was manually adjusted to minimize chest wall motion in the radiofrequency (RF) ultrasound images acquired during elastography.

The typical progression of experiments in the human subject scans in this study is shown in Fig. 5.1.

Fig 5.1: Pictorial representation of the progression of experiments conducted during a typical human subject scan in this study. Top left: First, a radiologist conducts a direct contact hand scan to initially localize the breast mass and compare image quality with through-paddle ultrasound scan. Top right: Subject's breast is compressed in the combined tomosynthesis/ultrasound system for acquisition of x-ray tomosynthesis images. Middle: While the breast is still compressed, the ultrasound transducer is scanned across the entire breast to obtain a full-field 3D volume of the breast in the same orientation and at essentially the same time as the tomosynthesis image. Bottom: The subject is moved from the combined system to the stand alone mammography-mimicking unit for precisely controlled through-paddle elastography.

5.3.4. 2D, 3D Phase-Sensitive Speckle Tracking

All 2D and 3D elasticity data were processed using conventional 2D and 3D phase-sensitive correlation-based speckle tracking algorithms, described in [30-31, 34] and reviewed in Chapter 2. This processing will be briefly summarized here.

Final outputs of 2D processing are the lateral displacement $u(x,y)$, axial displacement $v(x,y)$, and magnitude of the correlation coefficient $|\rho(x,y)|$. Analogously, the final outputs of 3D processing are the axial displacement $v(x,y,z)$, lateral displacement $u(x,y,z)$, elevational displacement $w(x,y,z)$, and magnitude of the correlation coefficient $|\rho(x,y,z)|$. All estimated displacements were accumulated over the total deformation range [32]. The final axial strain image (elastogram) is then produced from the axial derivative of the accumulated axial displacement estimates, according to Equation 1:

$$\varepsilon = \frac{\partial v}{\partial y} \tag{5.1}$$

To directly compare 3D speckle tracking results with their 2D analogues, the center slice from the 3D data was extracted and analyzed using traditional 2D speckle tracking. In this way, image quality could be directly compared between 2D and 3D strain and correlation coefficient images for the same slice.

Image quality was quantified using the magnitude of the 2D or 3D correlation coefficient and the SNR of the final axial elastogram (SNR_ε), calculated as described in [31]:

$$SNR_\varepsilon = \frac{E[\varepsilon]}{\sigma_\varepsilon} \tag{5.2}$$

where ε is the component of the strain tensor, $E[\varepsilon]$ is the mean strain, and σ_ε is the variance of strain estimates.

5.3.5. Imaging Methods – 2D, 3D Breathing Motion and Breast Stability

To quantify the extent of breathing motion during elasticity data acquisition, both breasts of 7 healthy volunteers were imaged using the M12L array at 10MHz as they breathed shallowly, held their breath, breathed deeply, and talked. The 91 RF frames acquired over 2 seconds on these subjects were correlated to the first frame in the RF sequence to measure how much movement occurred and the resulting decorrelation due to this motion. Note that no additional compression was applied during this motion study. The average correlation coefficient was measured as a function of time, depth, and distance from chest wall and was compared between each breathing technique and between right and left breasts.

To acquire high quality 3D elasticity data *in vivo*, data acquisition must be conducted within a consistent breathing pattern; otherwise, subject breathing motion could dominate decorrelation. To achieve this, all compression was induced quasistatically and the 3D scanning procedure, described in Chapter 4, collected 5 axial steps over 11 elevational slices with 0.4 mm slice size within 14 sec. External triggering of RF images was simultaneously employed as the breast was compressed to ensure all axial steps at different elevational locations were triggered at the same axial location within a reasonable scan time. Over the 4 cm imaging depth, one focal spot was set at 3 cm, corresponding to an allowed frame rate of 43 Hz. However, a slightly lower frame rate of 33 Hz was actually utilized with external triggering.

To determine whether patient breathing motion was affecting efficacy of the 3D elastography, a “baseline” 3D scan was conducted on each subject. To mimic a full 3D elastography scan, baseline scans collected 5 RF frames of data over each of 11 elevational slices, but without the compression and decompression between frames. This allowed decorrelation due to breathing motion to be separated from decorrelation due to compression or backlash.

Based on preliminary results, it was noted that extra precompression might be required for 3D elastography compared with 2D elastography because of the much greater scan time which was more sensitive to patient motion. This was not ideal because previous studies have noted that fibroadenoma contrast in strain images decreases with increased precompression because fibroadenomas exhibit a different non-linear stress-strain relationship than healthy tissue [23]. Thus, 4 subjects were imaged at multiple compressions to investigate the tradeoff between precompression for stability and its potential decrease in mass visibility in strain images.

5.3.6. Imaging Methods – Differential Correlation Coefficient Study

In this study, all RF images were acquired using a 1D linear array operating at 7.5 MHz through a TPX (a polymethyl pentene: speed of sound (c) = 2.22 mm/μs) 2.5 mm thick mammographic paddle [28-29]. Compression for the 2D elastography in the differential correlation coefficient and reader studies was induced by automatically raising the lower compression paddle, which was mechanically damped to minimize vibration artifacts. This process was supervised from a nearby computer communicating through its serial port to a VXM stepper motor controller (Velmex, Bloomfield, NY,

USA) connected to the paddle. In this manner, 90 RF images for 2D elastography were continuously acquired by compressing at 2.5 mm/s for up to 2 sec and 7% strain. Based on the results of the breathing motion studies, subjects were instructed to hold their breath during all elasticity scans.

A preliminary experiment was conducted to determine whether the differential correlation coefficient was approximately constant over the strain step size of 0.3-0.6% in this study. Data were decimated off-line to fall in this range. After 2D speckle tracking and accumulation of displacement estimates, the final correlation coefficient image was used to calculate differential correlation coefficient values.

To calculate the correlation coefficient in the lesion, the lesion was manually segmented in the grayscale ultrasound image, at least 1 mm within its border to minimize boundary effects and ensure that outside tissue minimally contributed to calculated lesion correlation coefficients. Fat and glandular tissue were not independently calculated due to the dependence of depth on the correlation coefficient in fat tissue and the lack of sufficient glandular tissue in older breasts for a reliable measurement. Background tissue was considered to be all tissue in the image outside the lesion ROI. The differential correlation coefficient was calculated according to:

$$\textit{Differential correlation coefficient (\%)} = \frac{\mu_{\rho,background} - \mu_{\rho,lesion}}{\mu_{\rho,background}} * 100\,\%, \qquad \textbf{(5.3)}$$

where $\mu_{\rho,background}$ is the mean correlation coefficient in the background ROI, and $\mu_{\rho,lesion}$ is the mean correlation coefficient in the lesion ROI. Note that according to Equation 5.3, the *greater* the differential correlation coefficient (DCC) value, the more the mass has decorrelated in response to compression.

Because this study aims to directly compare the correlation coefficient in the mass to the correlation coefficient in the background tissue, differential correlation coefficient images were created to standardize all results. To create these images, Equation 3 was modified and applied to each pixel in the image, according to:

$$\textit{Differential correlation coefficient (i, j) (\%)} = \frac{\mu_{\rho,background} - \rho_{i,j}}{\mu_{\rho,background}} * 100\,\%, \qquad \textbf{(5.4)}$$

where *(i, j)* is the pixel location in the 2D correlation coefficient image and ρ is the correlation coefficient value at that location. In this manner, each pixel in the differential correlation coefficient image is presented as a percent change in the average correlation coefficient in the image. In these images, black is the lower bound and corresponds to correlation coefficients which were more than 15% below the average, and white is the upper bound, corresponding to pixels which had correlation coefficients at or above the image average.

5.3.7. Statistical Analysis of Differential Correlation Coefficient Values

Due to the high variability of data included in the differential correlation coefficient study, it could not be assumed that data followed a normal statistical distribution. Thus all statistical analysis was conducted using a Mann Whitney U-test because of its non-parametric assumptions in its calculations. Additionally, because this study had a small sample size, we chose to report an exact p-value given by the Mann Whitney test, based on a finite sample distribution. $P < 0.05$ was considered to indicate statistical significance. For completeness, a 2-sample student t-test with unequal variances was also conducted, and confirmed statistical results in all cases. It should be

noted, however, that the sample size of the study might be too small to observe some differences which may exist.

5.3.8. Organization of Reader Study of 2D Elasticity Data

There were two main goals for the clinical reader study: 1) to determine if elasticity imaging of this quality has promise of clinical utility when presented with high quality tomosynthesis and through-paddle ultrasound images, and 2) to evaluate the appearances of different breast masses in elastograms and differential correlation coefficient images and compare results with the literature. With these goals in mind, the reader study was designed to have two sections and results were interpreted by 2 radiologists with 16-18 years of mammography and sonography breast imaging experience.

First, on 15 subjects with one breast mass of interest each, a complete case consisted of 1) the reconstructed tomosynthesis image, 2) the full cineloop of the through-paddle ultrasound image, and 3) the elastogram and differential correlation coefficient image over the center of the mass. The comparison with tomography rather than digital mammography was chosen because of the likelihood that tomography will soon become popular in clinical practice and because of the improved image quality of tomosynthesis images over conventional mammograms, which test the true utility of an adjunct imaging mode such as elastography in future clinical settings. All readers were asked to first review the tomosynthesis images and provide a BI-RADS score (on a scale from 0-5) and percent likelihood of malignancy (on a 0-100% scale) for the mass of interest. Immediately following the tomosynthesis reading of each case, readers were

presented with the through-paddle ultrasound image, and asked to give a modified BI-RADS score and percent likelihood of malignancy based on the information they could extract from the combination of the two modalities. Finally, readers were provided with the differential correlation coefficient image and axial strain image from the elasticity component of the study, and again asked to provide a BIRADS score and percent likelihood of malignancy. This structure was chosen because it mirrored a clinical setting of a diagnostic reading.

All readers were trained in the use of the forms just before interpreting the cases. For training, readers were provided with examples from previous literature reports and masses imaged with this system but excluded from the final study [22-24, 33]. Additionally, readers were provided with structured assessment forms of appearances of masses in the elastogram and differential correlation coefficient image to facilitate consistent reporting of elasticity findings (Table 5.3, 5.4). The elasticity characteristics provided in the forms were compiled from previous literature reports and the training summarized those findings [22-24, 33]. Readers described the appearances of the 15 masses from the first part of the study, plus 5 additional masses. Additionally, readers manually segmented the mass of interest in the grayscale ultrasound image, differential correlation coefficient image, and elastogram provided in the reader study. From these segmentations, relative lesion size and mean differential correlation coefficient were calculated and displayed for the readers to aid in their characterization.

Readers were informed that all cases in this study contained one mass of interest and each mass fell into one of three categories: cyst, fibroadenoma, or cancer. Because the purpose of this study was the diagnostic efficacy of elastography with the combined

system, and not screening efficacy, the mass of interest was identified for each reader in each imaging mode.

Table 5.3: Elastogram characteristics of breast masses reviewed by radiologists in the reader study.

Elastogram Characteristic	***Possible Values***
Lesion Visibility	Contaminated by Artifacts Not visible Poorly visible Visible Very visible Highly visible
Lesion Size Comparison: Elastogram to Sonogram	Smaller in elastogram Similar in elastogram Larger (> 1.2x) in elastogram
Relative Stiffness	Much harder (stiffer) Harder Same as surrounding tissue Softer Much softer
Margin regularity	Smooth and round Irregular Combination
Margin definition	Sharp Somewhat sharp or slightly indistinct Indistinct
Elastographic pattern	Uniform Heterogeneously softer and stiffer Complex
Boundary Flow	Present Absent

Table 5.4: Correlation coefficient characteristics of masses reviewed by radiologists in the reader study.

Differential Correlation Coefficient Image Characteristics	***Possible Values***
Lesion Visibility	Not visible Poorly visible Visible Very visible Highly visible
Correlation coefficient comparison	Much lower in lesion (< -15%) Lower in lesion (-5% to -14.9%) Similar to surrounding tissue (-5% to 0%) Higher in lesion (0% to 5%) Much higher in lesion (> 5%)
Lesion size comparison: differential correlation coefficient image to sonogram	Smaller in DCC image Similar in DCC image Larger in DCC image

5.3.9. Analysis of Reader Study of 2D Elasticity Data

The small sample size of subjects in the reader study precluded statistical significance analysis of the results. Instead, the percentage of benign masses which appeared more benign after the elastography reading and the percentage of malignant masses which appeared more malignant after the elastography reading were compiled. Trends in the appearances of the different breast masses were also summarized and compared to previous literature reports.

5.4. Results

5.4.1. 2D, 3D Breathing Motion and Breast Stability Analysis

The 2D motion study was conducted to determine the amount of decorrelation due to chest wall motion over the typical 2 sec scan time, how to minimize this motion, and whether this decorrelation affected the quality of resulting strain images.

Breathing motion was evident in correlation plots for all four breathing patterns: shallow breathing, deep breathing, holding breath, and soft talking (Fig. 5.2). Over the 2 second scan in both breasts, deep breathing quickly decorrelated to $\rho < 0.8$, whereas holding breath, shallow breathing, and talking remained approximately at $\rho \geq 0.9$ for the entire scan.

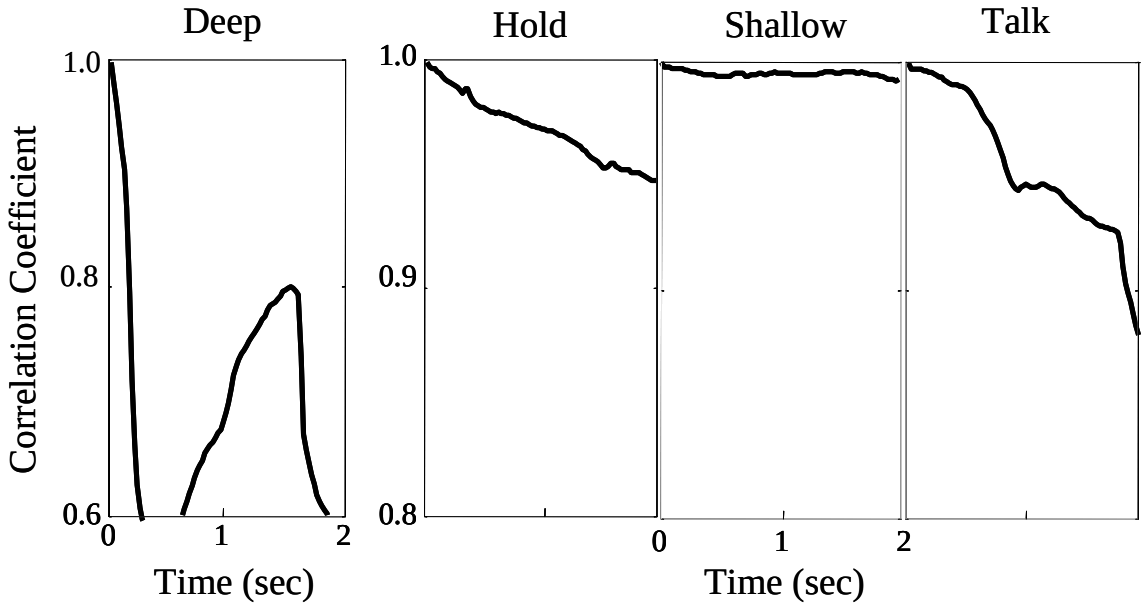

Fig. 5.2: Plots of the average correlation coefficient over the entire image and over all subjects for each breathing pattern as a function of time. Deep breathing caused quick decorrelation; however, holding breath, shallow breathing, and talking maintained correlation coefficients above 0.9 over the 2 sec scan.

Additionally, correlation coefficients quickly decreased at depths greater than 3.7 cm, due to poor SNR in the images at these depths. These trends were consistent regardless of breast or breathing technique. Increased decorrelation also occurred within

about 5 mm of the chest wall, which could be due to poor paddle contact with the breast or boundary effects from speckle tracking. These trends are represented graphically in Fig. 5.3. Thus, keeping the lesion away from boundaries and close to the transducer is critical in preventing extra decorrelation and artifacts in elasticity imaging using the combined system.

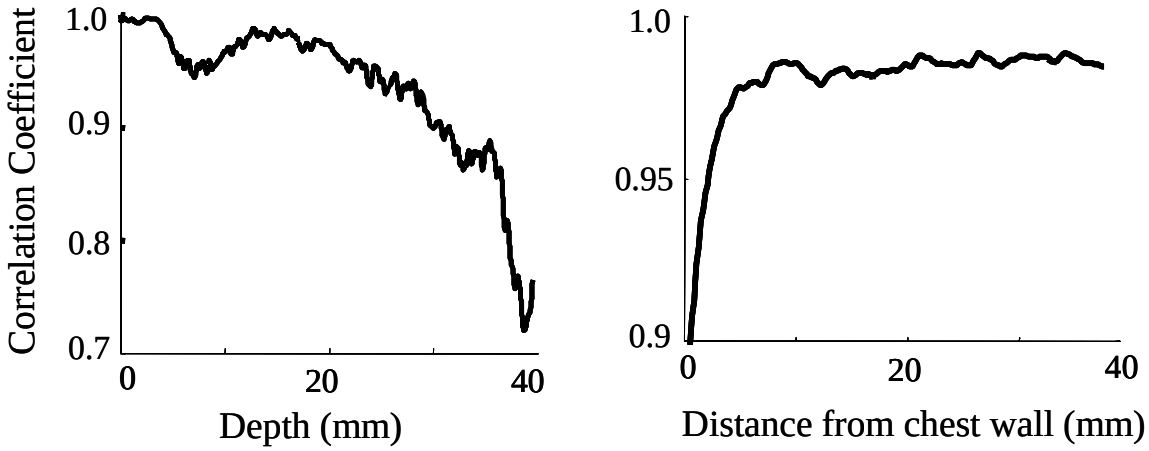

Fig. 5.3: (Left) Representative correlation coefficient plot as a function of depth. At depths greater than 37 mm, the correlation coefficient begins to drop off quickly due to low signal-to-noise ratio at those depths. **(Right)** Representative correlation coefficient plot as a function of distance from the chest wall (CW). Within 5 mm of the chest wall, there is substantial decorrelation. In summary, these two plots demonstrate depth and location limitations of the masses for future human subject scans.

Averaged over the entire image region, shallow breathing maintained the highest correlation ($\rho = 0.96$) and deep breathing was the worst ($\rho = 0.73$). However, holding breath and talking also had relatively high correlation coefficient values ($\rho = 0.93$ and 0.87, respectively). The average correlation coefficient for all breathing patterns in the right breast was $\rho = 0.88$ and in the left breast was $\rho = 0.89$. A Wilcoxon two-sample statistical test determined that these correlation coefficient differences between each breast were not statistically significant ($P >> 0.1$). Differences in correlation coefficient values for shallow breathing, holding breath, and talking were statistically significant from deep breathing ($P << 0.05$), but not from each other ($P >> 0.1$). Average correlation coefficient values for each breathing pattern in each breath are illustrated in Fig. 5.4.

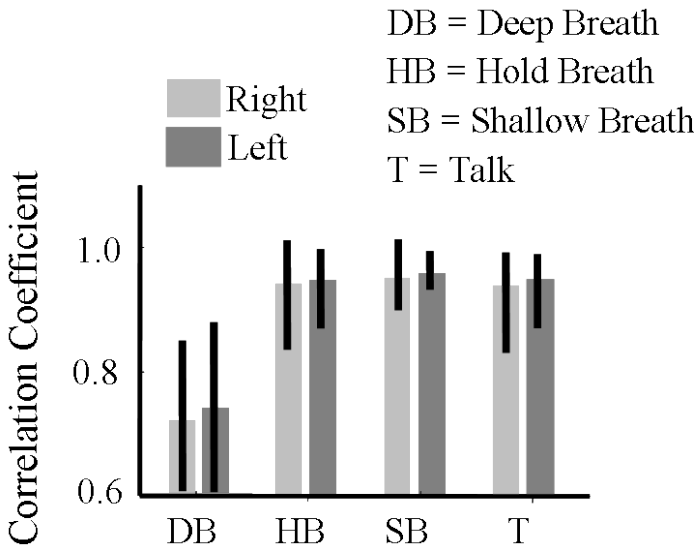

Fig 5.4: Comparison of correlation coefficient values in the right and left breasts averaged over all imaging depths and all subjects. Black lines represent error bars. The small differences demonstrated in this plot are not statistically significant (P >> 0.1).

In summary, asking subjects to breathe shallowly or hold their breathing during 2D through-paddle elasticity scans should minimize decorrelation, and thus artifacts in elastograms, due to chest wall motion. Chest wall motion could be further minimized by keeping lesions away from boundaries and only imaging lesions shallower than 3.7 cm.

After chest wall motion was determined to be a minimal concern in 2D through-paddle elastography, the next step was to evaluate whether subjects could maintain a consistent breathing pattern over the 13.7 sec data acquisition required for a 3D elasticity scan. This was measured by conducting a baseline scan in 6 subjects a total of 12 times. The phantom experimental results presented in Chapter 4 revealed that 3D scans with no axial compression and elevational translation of the transducer in just one direction yielded a correlation coefficient of 1.00, as expected. Therefore, any reduction in this value under the same conditions *in vivo* could be attributed to tissue relaxation or subject chest wall motion.

Though the combination of hairspray and minimal precompression with shallow breathing or holding breath sufficiently stabilize the breast for a 2 sec elasticity scan, the longer data acquisition time for 3D elasticity introduces additional difficulties when imaging through a mammographic paddle. On average, chest wall motion created a 0.8% ± 0.5% reduction in the correlation coefficient in the baseline scans. The minimum reduction was 0% and the maximum reduction was 3%. The main consequence of this motion was that the 3D elastogram of 2 of the 12 subjects (17%) exhibited artifacts that were not present in the 2D elastogram (Fig. 5.5).

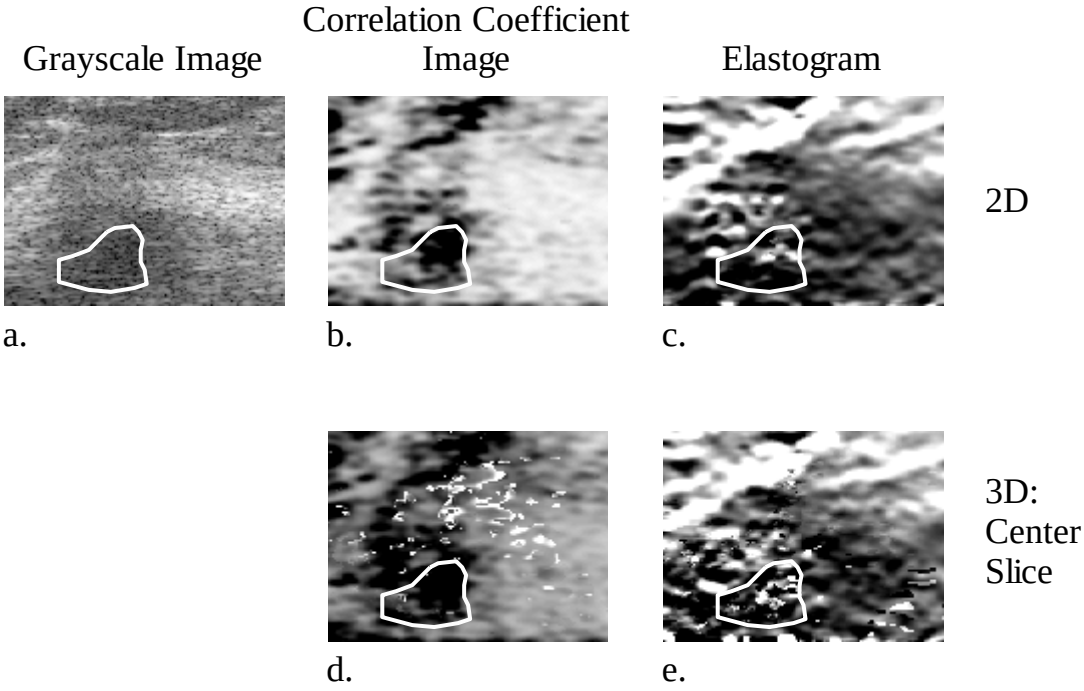

Fig 5.5: a) Grayscale ultrasound image of a hypoechoic cancer, **b)** correlation coefficient image created using 2D speckle tracking algorithms on the center slice of the 3D elasticity data, plotted from 0.8-1.0, **c)** corresponding axial elastogram created using 2D speckle tracking algorithms on the center slice of the 3D data, **d)** correlation coefficient image of the center slice of the 3D elasticity data, created using 3D speckle tracking algorithms, and **e)** axial elastogram of the center slice of the 3D elasticity data, created using 3D speckle tracking algorithms. The white artifacts in **(d)** and resulting black and white streaks in **(e)** are a consequence of subject chest wall motion during the 14 sec 3D scan.

To determine if additional preload could reduce or eliminate breathing motion effects by additionally stabilizing the breast, 4 of the 12 subjects (33%) were imaged at multiple preload levels and the resulting elastograms were compared (Fig. 5.6). Fig. 5.6 illustrates the tradeoff that can sometimes occur between reduced motion artifacts with increased preload and reduced elastogram lesion contrast. It is unlikely that an ideal pre-compression range for imaging with this system exists, as different compositions of breast tissue and different locations of the lesions will affect how much pre-compression is required to stabilize the breast. However, imaging at multiple pre-compression levels will allow the elastogram with the least artifacts and greatest contrast to be retrospectively chosen.

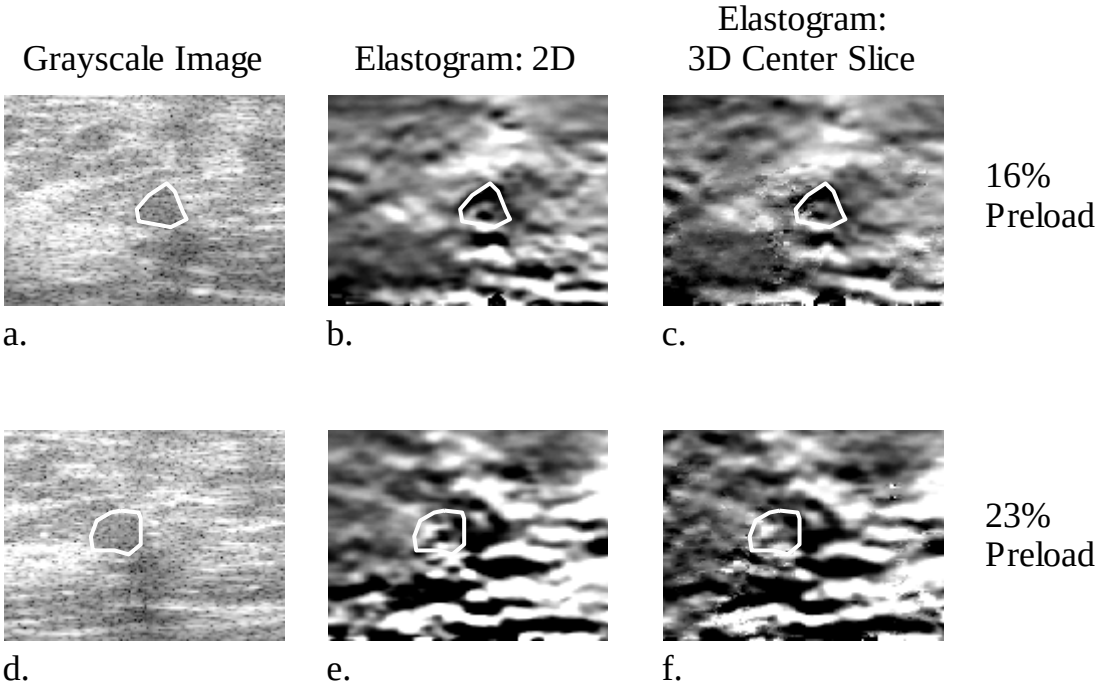

Fig. 5.6: Fibroadenoma imaged with 2D and 3D elastography at 16% preload **(a,b,c)** and 23% preload **(d,e,f)**. With the additional 7% compression, artifacts in the 3D elastogram from chest wall motion are reduced, but so is mass contrast in the elastogram.

It should be noted that the majority of the subjects imaged with 3D did not have a problem with maintaining a consistent breathing pattern over the scan. In those cases, the SNR improvements observed in phantom experiments in Chapter 4 translated *in vivo*. These improvements were most evident when the lesion was solid, visible, in a high quality region of the B-mode image, and chest wall motion was minimal. Demonstrated in Fig. 5.7, improved SNR in the 3D elastogram improves lesion visibility as well as boundary definition. The natural extension of this automated scanning to multiple, parallel slices of the same lesion would give better statistical sampling of this boundary phenomenon as well as other diagnostic criteria.

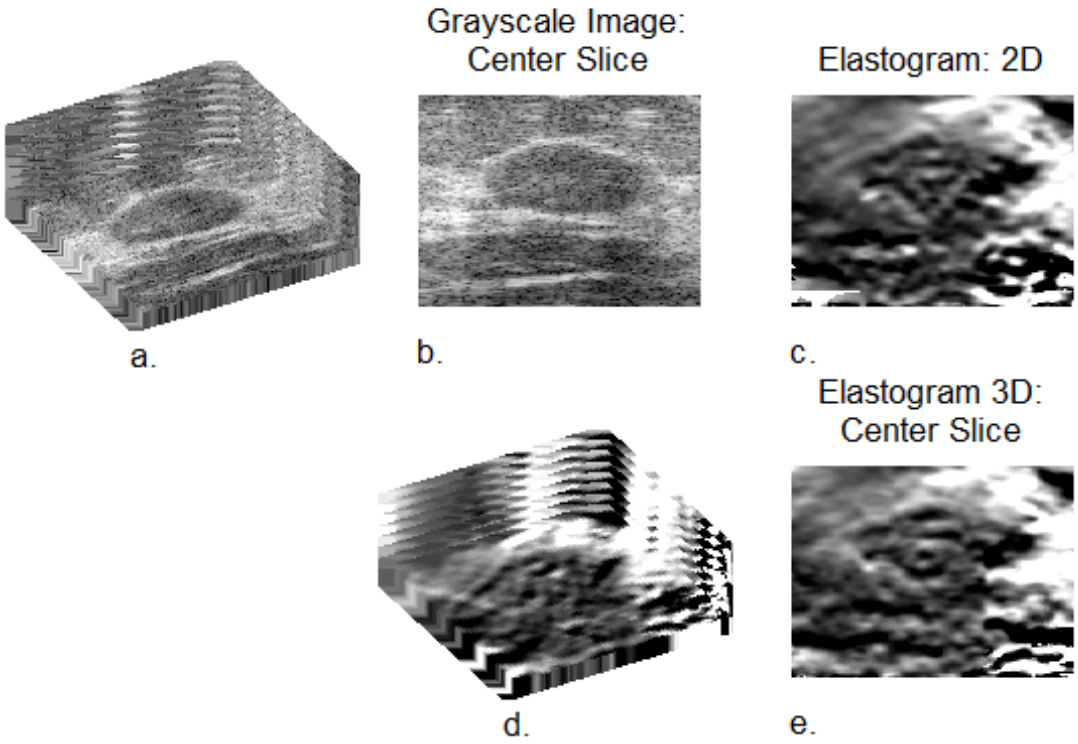

Fig. 5.7: a) Grayscale ultrasound volume (40 mm x 39 mm x 4.4 mm, axial x lateral x elevational) of fibroadenoma imaged with 3D elastography; **b)** center slice of 3D volume from **a)**; **c)** 2D elastogram analyzed from center slice of volume; **d)** elastogram volume analyzed using 3D elastography; **e)** center slice of elastogram volume from **d)**. *In vivo* 3D elastography improved visualization of the fibroadenoma over its 2D analogue, particularly in the lower boundary.

For the remainder of this chapter, all *in vivo* results will be from 2D elastography, as there was insufficient 3D data for quantitative clinical studies.

5.4.2. Characterization of Cysts using Differential Correlation Coefficient Values from 2D Breast Elastography: Preliminary Study

As previously described, appearances of cysts in elastograms can vary according to image processing factors, rather than biological factors. Previous reports have shown cysts with varying elastographic appearances: 1) noisy, 2) not visible, and 3) containing both dark (stiffer) and bright areas, respectively [22-25]. In contrast to the variability of cyst appearances in elastograms, cysts are consistently visible in correlation coefficient images, appearing "black" due to their low correlation coefficients. The term "differential correlation coefficient" in this study describes the percent difference in the average correlation coefficients in masses versus their background tissue in an effort to quantify differences in decorrelation.

Mean and standard deviation of the differential correlation coefficients between surrounding tissues and cysts, fibroadenomas, and cancers were 27.5 ± 11.4%, 5.9 ± 6.1% ($P = 0.0003$), and 3.8 ± 2.9% ($P = 0.004$), respectively (Fig. 5.8). Overall, much lower correlations (12-41% below tissue) were observed in cysts than in surrounding tissue, as expected. No cyst exhibited a higher correlation coefficient than the background in this study, though one fibroadenoma did (DCC = -5.6%).

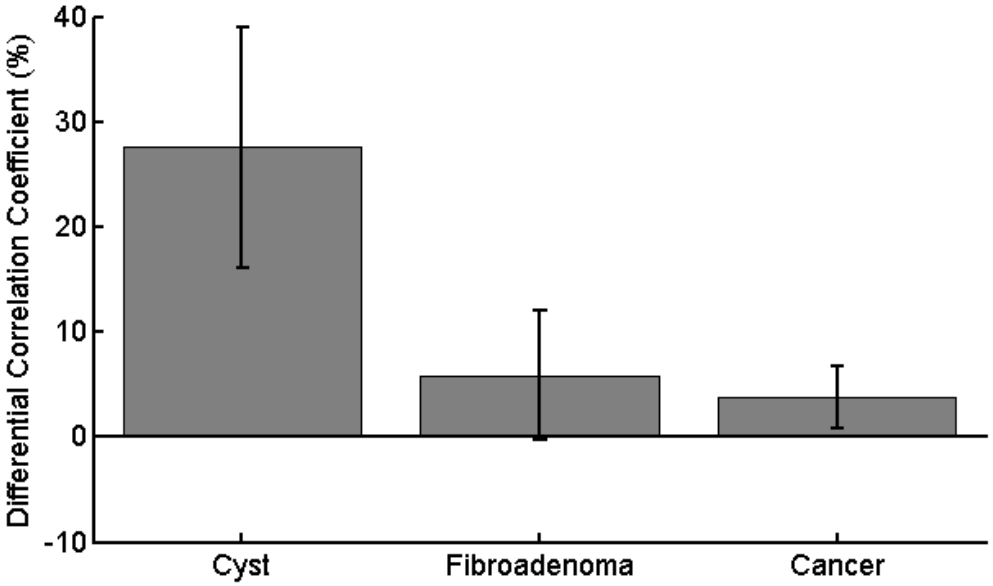

Fig. 5.8: Absolute value of mean and standard deviation differential correlation coefficient (DCC) values for each lesion classification. A Mann Whitney U-test (confirmed with a student t-test with unequal variances) verified that differences were significant between cysts and each of the other groups.

Fig. 5.9a compares DCCs for three depth groups: <15 mm, 15-25 mm, and >25 mm. Lesion depth was measured as the distance from the transducer to the center of the lesion, when the breast was under compression. Though the size of these sub-groups is too small for statistical comparison, the smallest difference between DCCs is in the >25 mm depth range where solid masses appear more hypoechoic due to low SNR in the ultrasound image. To assess the effect of lesion size on DCC values, lesions were grouped into 3 regions based on their diameter: < 10, 10-20, and > 20 mm (Fig. 5.9b). Lesion diameter was calculated from the grayscale ultrasound image of the compressed breast as the average of the transverse and longitudinal dimensions of the lesion. Though not enough lesions fell into each group to be statistically evaluated, relative DCC values between lesion groups were fairly consistent with respect to size.

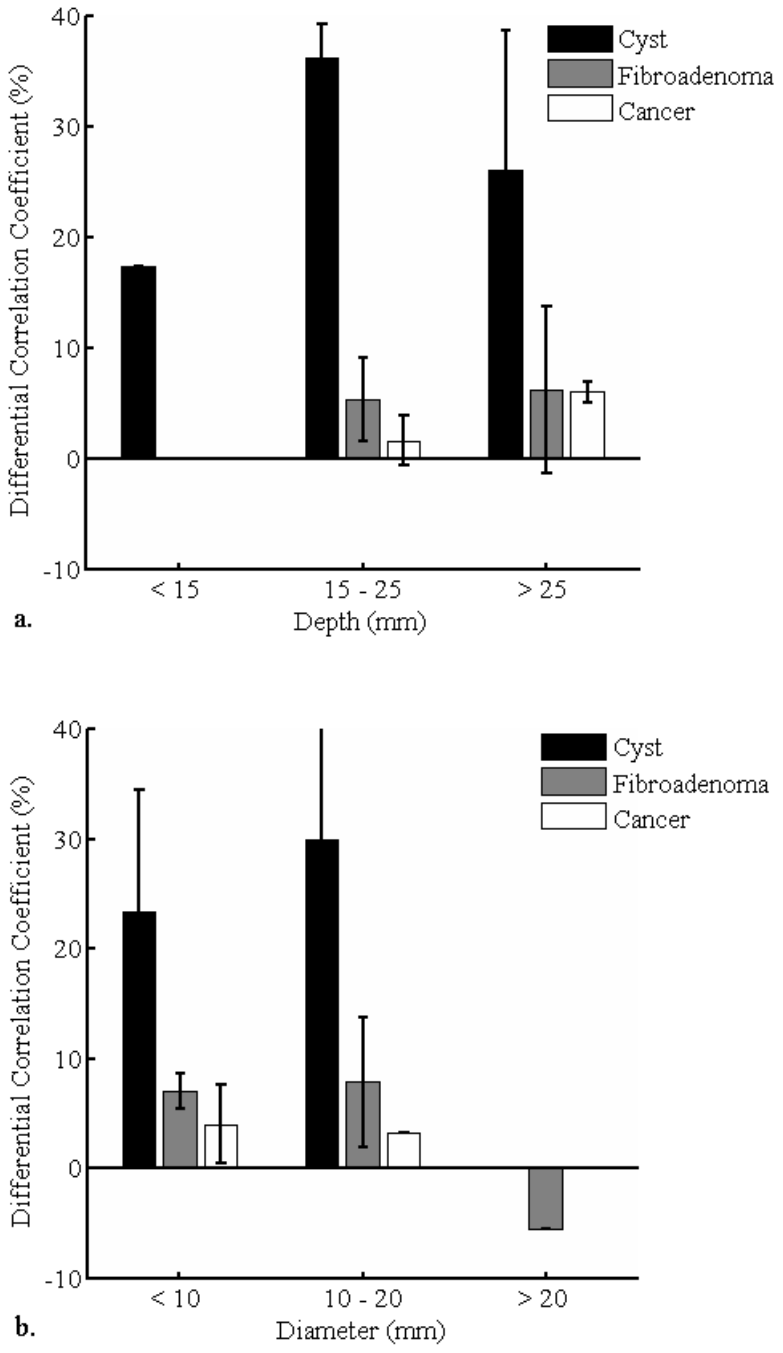

Fig. 5.9: Analysis of differential correlation coefficient (DCC) values grouped according to lesion depth **(a)** and diameter **(b)**. Statistical comparison was not possible due to the low number of lesions in each group. The most overlap between lesion types occurred at the greatest depths analyzed in this study, most likely due to the decorrelation being dominated by the low signal-to-noise (SNR) in the lesions. Characterization of small (< 10 mm) lesions should not be adversely affected by this technique, as long as partial volume averaging and sidelobe "fill in" do not dominate DCC values in this sample.

The appearance of the lesions in the DCC image, scaled such that "black" corresponds to > 15% below image mean and white corresponds to image mean value up to a correlation coefficient of 1, also varied with lesion type. The DCC in the cysts appeared mostly uniform and black (low) in those images with some random scattering of low DCC values in their interior (Fig. 5.10). Only one cyst in this study exhibited a DCC less than 15% below the image mean (DCC = 12%); this cyst was both small and deep.

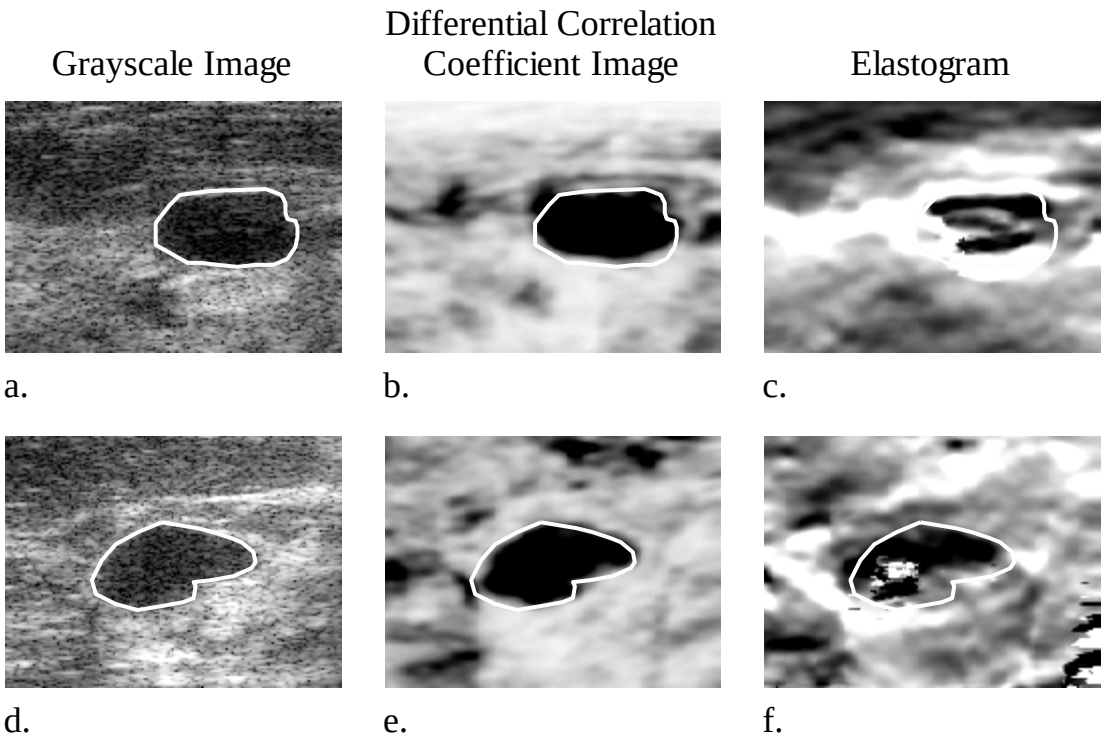

Fig. 5.10: Representative cyst grayscale **(a, d)** and corresponding 2D differential correlation coefficient (DCC) **(b, e)** images and 2D elastograms **(c, f)**, respectively. Cysts might be classified in DCC images according to their mainly black appearance, with some higher correlation around the boundaries due to partial volume averaging effects on the boundaries. The cyst shown in **(a,b,c)** was 1.8 cm deep (DCC = 34%), and the cyst shown in **(d,e,f)** was 2.7 cm deep (DCC = 24.5%). In contrast, the appearances of the cysts in the elastograms are different, with the top cyst appearing black (stiffer) with a softer region in the middle, and the bottom cyst exhibiting both stiff and soft regions. Differential correlation coefficient images are plotted on a scale from minimum possible value (-6.4% in (**b**), -7.5% in (**e**)) to a maximum 15%. Black represents high DCC values in the image (highly decorrelating tissue), and white represents low DCC values. Image sizes are 25 mm x 25 mm.

Two of the fibroadenomas (25%) exhibited DCC values ≤ 2%. Both of these were classified as "classic" fibroadenomas in their grayscale images: demonstrating characteristics such as wider than tall, elliptical in shape, and encapsulated by a thin, echogenic capsule [9]. The DCC in the remaining 6 (75%) fibroadenomas was 5.3-15.4%. Representative grayscale, differential correlation coefficient, and strain images of the fibroadenomas in this study are shown in Fig. 5.11.

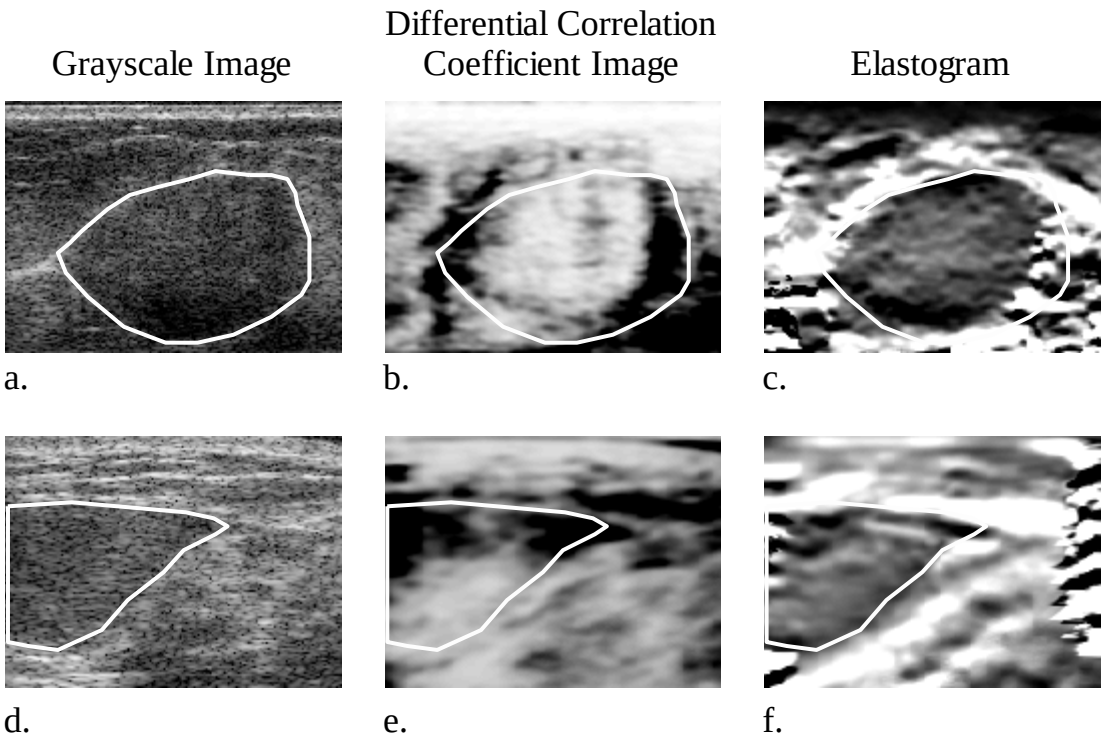

Fig. 5.11: Representative fibroadenoma grayscale **(a, d)** and corresponding 2D differential correlation coefficient (DCC) **(b, e)** images and elastograms **(c, f)**, respectively. The classic fibroadenoma in **(a,b,c)** exhibited a DCC = 3.2%. The fibroadenoma in **(d,e,f)** was 1.9 cm depth (DCC = 6.6%). Both fibroadenomas appear somewhat harder (dark gray) in the elastograms, as expected. DCC images are plotted on a scale from minimum possible value (-7.5% in (**b**), -9.9% in (**e**)) to a maximum 15%. Black represents high DCC values in the image (highly decorrelating tissue), and white represents low DCC values. Image sizes are 25 mm x 25 mm.

The DCC values from all 4 cancers analyzed in this study, two of which are shown in Fig. 5.12, were more homogeneous and more closely matched to the

background tissue correlation coefficient than observed in the fibroadenomas (DCC = 0.0 – 6.7%). These measures were consistent between carcinoma types.

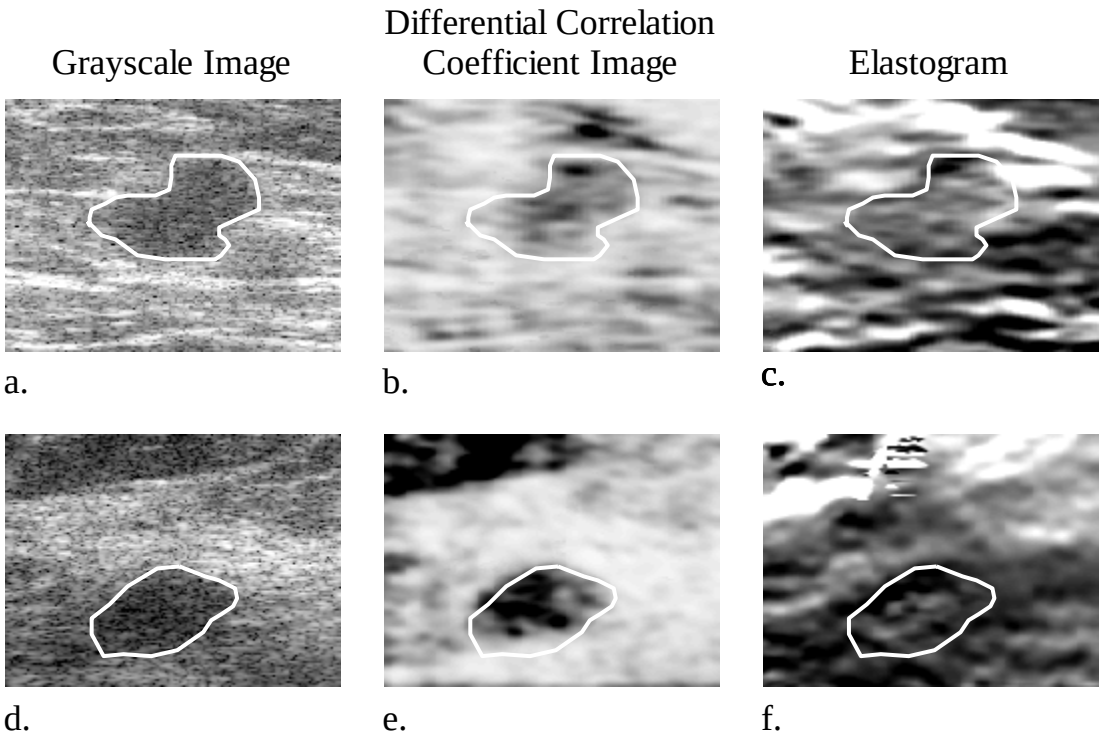

Fig. 5.12: Representative cancer grayscale **(a, d)** and corresponding 2D differential correlation coefficient (DCC) **(b, e)** images and elastograms **(c,f)**, respectively. Cancers might be classified in DCC images according to both their lower mean DCC values and lower standard deviations as evidenced in **(b)** (DCC = 3.2). The cancer in **(d)** (DCC = 6.7%) was initially characterized clinically as a "complex cyst" Pathology results confirmed it was a carcinoma, Bloom-Richardson grade 2. DCC images are plotted on a scale from minimum possible value (-7.5% in (**b**) and (**e**)) to a maximum 15%. Black represents high DCC values in the image (highly decorrelating tissue), and white represents low DCC values. Image sizes are 25 mm x 25 mm.

5.4.3. Reader Study: Efficacy of 2D Breast Elastography as part of a Combined Ultrasound/Tomography System

The reader study in this dissertation was designed to analyze the clinical utility of the techniques from the available data in this dissertation and was read by 2 radiologists in the Breast Imaging department at the University of Michigan. The study was broken into 2 parts. The goal of Part 1 (15 subjects) was to assess whether elasticity could be a

useful adjunct to x-ray tomography and ultrasound in characterizing the likelihood of malignancy for a lesion. Part 2 (the 15 subjects from Part 1 plus 5 additional subjects) was designed to evaluate the appearance of different masses in elastograms and differential correlation coefficient images to find trends which might help characterize mass types in using those images.

Of 2 readings of 15 subjects with one mass each (6 cysts, 5 fibroadenomas, 4 cancers), the judged percent likelihood of malignancy decreased in 50% of cysts and 20% of fibroadenomas after reviewing the elasticity results (Fig. 5.13). The decreased likelihood of rating of malignancy in the cysts was entirely attributed to their high differential correlation coefficient values (low correlation), which increased reader confidence that the mass of interest was a complicated cyst rather than a solid mass. Elasticity decreased the likelihood of malignancy in one cancer, which was diagnosed as an invasive ductal carcinoma which was not visible on the elastogram. In this case, the percent likelihood of malignancy reduced from 90% after the tomosynthesis and ultrasound readings to 75% after the tomosynthesis, ultrasound, and elasticity readings. However, the BI-RADS score remained a “4c” corresponding to “moderate suspicion” and the DCC value was 7.3%, which is well below the threshold for characterizing a mass as a cyst. Only 25% (2 of 8) of malignant lesions appeared more malignant after reviewing elasticity images. These masses were classified as more malignant based on the lesion size comparison parameter first introduced by Garra et al. and Hall et al. [22-23]. No cyst in this study appeared more malignant, again due to the high differential correlation coefficient scores which increased reader confidence that the mass of interest was a cyst, even when the cyst appeared stiffer in the elastogram. The 50% of cysts

which exhibited no change in likelihood of malignancy in this study were given a BI-RADS score of 2 (Benign) and percent likelihood of malignancy of 1% after reviewing the tomosynthesis and ultrasound images, and thus elastography was not needed to improve characterization in these cases. Of 9 of 12 cysts which were scored a BI-RADS score of 3 or 4, and thus biopsy would have been expected, 4 of the 9 (44%) were lowered to a non-biopsy certainty level (BI-RADS = 2) by analysis of the DCC image. (Two of the cysts were reduced from BI-RADS = 4 to BI-RADS = 2, and two were educed from BI-RADS = 3 to BI-RADS = 2). Note that no fibroadenoma or cancer was given a BI-RADS score less than a 3 for any modality or by any reader, and thus all fibroadenomas and cancers would be sent to biopsy regardless of the addition of information from ultrasound or elasticity images.

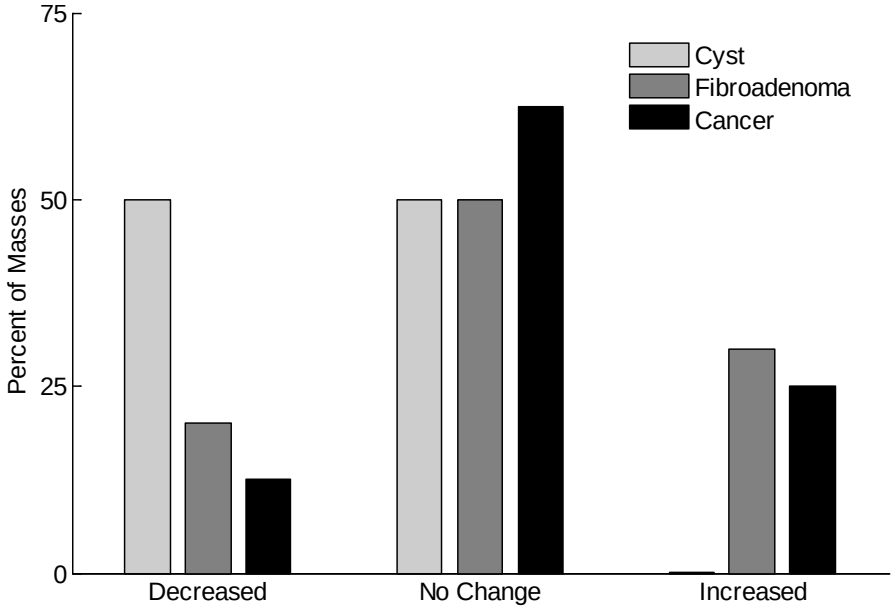

Fig. 5.13: Change in likelihood of malignancy of different breast masses after reviewing elasticity results. In total, 36% (8 of 22) benign masses appeared more benign when using elastography as an adjunct to tomography and conventional grayscale ultrasound for characterizing the likelihood of malignancy of the masses. The greatest contributor to this increase in benignity was the differential correlation coefficient image, which increased reader confidence that a mass was a complicated cyst. Reassuringly, no malignant masses appeared more benign in this study. Only 25% (2 of 8) cancers appeared more malignant in this study, suggesting that elastography may play a greater role in reducing biopsies of benign masses than distinguishing malignant from benign.

Mean BI-RADS scores were quantified for all readings, assigning each category a numerical value, such that categories 0-3 were scored 0-3, categories 4 a,b,c were scored "4", and so on (Table 5.5). Mean BI-RADS score for cysts decreased as additional information was provided to the readers, with elasticity reducing the mean BI-RADS score to 2.8 ± 0.9. In contrast, the mean BI-RADS score for fibroadenomas increased after the addition of ultrasound because some fibroadenomas can exhibit sonographic characteristics similar to cancers. The addition of elastography slightly reduced the BI-RADS score for these fibroadenomas, but not enough to change management options. Cancers in this study exhibited a modified BI-RADS score of 4.0 after reviewing the tomosynthesis image, with 3 of 8 given a score of "4c", 2 of 8 given a score of "4b", and 3 of 8 given a score of "4a". Supplementing ultrasound images increased these score, but no change was observed after elastography.

Table 5.5: Mean and standard deviation BI-RADS score for all readings.

BI-RADS score	***Cyst***	***Fibroadenoma***	***Cancer***
X-ray Tomosynthesis	3.4 ± 0.8	3.4 ± 1.0	4.0 ± 0.0
X-ray Tomosynthesis + Ultrasound	3.2 ± 0.8	3.8 ± 0.4	4.3 ± 0.5
X-ray Tomosynthesis + Ultrasound + Elasticity	2.8 ± 0.9	3.7 ± 0.5	4.3 ± 0.5

In Part B of the reader study, radiologists were asked to characterize the appearances of the breast masses in the elastograms and differential correlation coefficients, given guidelines and examples summarized from previous literature reports. For each case, each reader segmented the mass in the grayscale image from which the

elasticity results were produced, the differential correlation coefficient image, and elastogram. In this manner, differential correlation coefficient values and lesion sizes were quantified and displayed for the readers. Good agreement existed between lesion sizes and differential correlation coefficients calculated from reader segmentations. As illustrated in Fig 5.14, the differential correlation coefficient values exhibited by cysts are nearly separable from solid masses. Setting a threshold at DCC = 20%, two cysts would be misidentified as solid masses, and only one solid mass (a fibroadenoma) would be misidentified as a cyst.

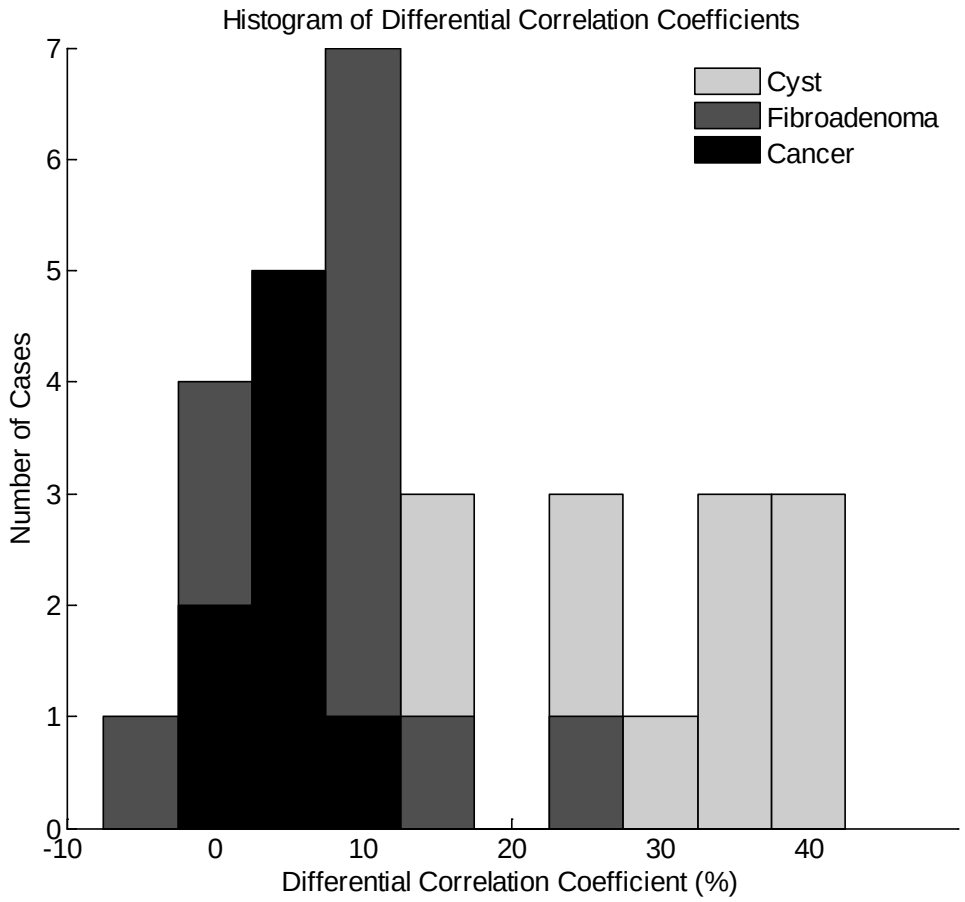

Fig. 5.14: Histogram of differential correlation coefficients calculated from reader segmentations of masses in the reader study. Setting a threshold at DCC = 20%, values are nearly separable between cystic and solid masses. Most importantly, no cancers would be mistaken for cysts.

One characteristic evaluated in the reader study was lesion visibility in the elastogram. Previous studies reported > 90% fibroadenomas and cancers were visible in elastograms, while 75% cysts were visible [22]. In this study, 8 of 16 cysts were not visible, 4 of 16 fibroadenomas were not visible, and 5 of 8 cancers were not visible. There exist several possible explanations for this low visibility. First, a cyst dominated by artifacts in the elastogram due to high decorrelation was characterized as “not visible.” Second, the high preload levels (15-20%) required for breast stabilization may have reduced visibility of fibroadenomas, as their elastogram contrast decreases with preload [23]. Third, one cancer appeared solely as a shadow in the ultrasound image, which was not ideal for elastography. Finally, experimental setup instability – particularly a transducer which was nonparallel to the compression surface or which was not stabilized properly - resulted in low quality raw data and reduced lesion visibility in one cancer. However, when visible in elastograms, further efforts were made to characterize mass appearances.

The relative stiffness of a breast mass to its surrounding tissue has been previously reported to differ between mass types [22]. Garra et al. reported that cancers generally appeared much stiffer (much darker) in elastograms than healthy tissue, whereas fibroadenomas appeared stiffer [22]. Both Garra et al. and Hall et al. reported that cysts can appear stiffer or softer in elastograms, sometimes depending on how much compression is applied [23]. In this study, 7 of 8 cysts which were visible on elastograms were described to be harder or much harder than surrounding tissue, along with 8 of 12 fibroadenomas, and 1 of 3 cancers. Because of this, readers had much difficulty in using relative stiffness to distinguish between mass types.

One of the most promising indicators of malignancy in elastography, according to previous literature, has been the size of the mass in the elastogram compared with the size of the mass in the sonogram [23-24, 33]. Previous studies have attributed this characteristic to a property called desmoplasia – the infiltration of cancers into surrounding tissue results in the stiffening of those tissues [23]. Using the threshold that a mass with area 1.2 times greater in the elastogram is malignant has produced 97-100% sensitivity, but 25-75% specificity in previous studies conducted by other researchers [24, 33]. However, in the very small sample of this study, only 33% (1 of 3) of cancers visible in elastograms fell above this threshold, whereas 42% (5 of 12) of fibroadenomas fell above this threshold. This greatly contributed to the 30% of fibroadenomas which appeared more malignant after reviewing elasticity results. One explanation for the high number of false positives is the poor visibility of some of the fibroadenomas in the elastograms, which may have made it difficult to ascertain where their true boundaries were. Application of 3D elastography may improve this in the future. Because the sample size of the cancers in this study was so small, it may not be possible to conclude much from these results. However, it should be noted that one of the cancers was a malignant complex cyst which may not have this property

In contrast to the tissue infiltration observed in many carcinomas, because fibroadenomas are typically stiffer than surrounding tissue but do not infiltrate, they experience a degree of mobility under compression [38]. This can create boundary flow in the elastogram – a region of high strain (soft tissue) surrounding one or more sides of the fibroadenoma [38]. In this study, no cancer exhibited boundary flow (a region of high strain (soft tissue) surrounding one or more sides of the mass), as expected, though 3 of 8

cysts (38%) and 4 of 12 (33%) fibroadenomas did. One caveat of this characteristic is that approximately 2% of circumscribed masses are cancerous, and thus boundary flow could produce false negatives. The efficacy of this characteristic in characterizing breast masses should be further explored.

Neither elastographic pattern nor mass size in the differential correlation coefficient image demonstrated unique trends for different mass types. Most of the cysts (7 of 8) and fibroadenomas (8 of 12) which were visible in elastograms appeared harder or much harder than surrounding tissue. This could increase confusion regarding whether this characteristic is reliable in distinguishing malignant from benign masses. After examining margin regularity in elastograms, 75% (6 of 8) cysts exhibited smooth and round margins, compared with irregular margins judged in 58% (7 of 12) fibroadenomas and 100% (3 of 3) cancers. Margin definition was also sharp in the cysts, though it varied in fibroadenomas and cancers.

These characteristics are summarized in Table 5.6.

Table 5.6: Reader study summary of 2D elastography characteristics exhibited by each mass type.

Elasticity Characteristic	***Cyst***	***Fibroadenoma***	***Cancer***
Elastogram Visibility	7/16 had artifacts 1/16 not visible	3/16 not visible 7/16 at least visible	5/8 not visible 2/8 poorly visible
Lesion Size Comparison: Elastogram to Sonogram	8/8 smaller or similar	5/12 larger	1/3 smaller 1/3 similar 1/3 larger
Relative Stiffness	7/8 harder or much harder	8/12 harder or much harder	1/3 harder 2/3 same as tissue
Margin Regularity	6/8 smooth & round	7/12 irregular	3/3 irregular
Margin Definition	7/8 sharp	5/12 sharp 6/12 indistinct	1/3 in between 2/3 indistinct
Boundary Flow	3/8 flow	4/12 flow	0/3 flow
Correlation coefficient in mass	10/16 much lower 6/16 lower	3/15 much lower 7/15 lower	0/8 much lower 4/8 lower

5.5. Discussion

5.5.1. Effect of Subject Breathing Motion on Decorrelation

Though elasticity imaging has shown great promise to be a valuable diagnostic tool, it is very sensitive to breathing motion. This motion causes extra frame-to-frame decorrelation which produces peakhop artifacts, which obscure lesion visibility. Minimizing breathing motion is needed to create high quality strain images with the combined tomosynthesis/ultrasound system.

Shallow breathing correlations remained steady over time and distance, yielding an $\rho > 0.9$ ($\rho_{avg} = 0.96$) in all but one acquisition. When subjects held their breath, the mean correlation coefficient was 0.93 with slow decrease over time due to chest/diaphragm relaxation. Deep breathing would make elasticity imaging with this system unrealistic ($\rho < 0.81$). Talking was most variable ($\rho = 0.82$-0.99), depending on speech volume and frequency. In some cases, more motion was observed less than 5 mm from the chest wall. This is most probably due to an edge effect caused by hairspray contact between the breast and the paddle, which may have led to some breast slippage. Comparable motion occurred bilaterally, indicating that left breast cardiac motion is not an additional problem in this geometry. Thus, in 2D, breathing motion can be minimized by breathing shallowly or holding breath and keeping lesions away from image boundaries and close to the transducer. The combination of these motion-minimizing efforts yields good quality 2D through-paddle elastograms.

Extending elastography to 3D adds complexity to the data acquisition process as scan times are much longer than in 2D (14 sec versus 2 sec), increasing the difficulty of imaging over a consistent breathing pattern and the likelihood of resulting motion artifacts. In baseline scans, subject chest wall motion reduced the 3D correlation coefficient by a modest 0.8% +/- 0.5%. Pre-compression levels play a strong role in the visibility of lesions, and a tradeoff exists *in vivo* since increasing pre-compression increases breast stabilization at the expense of SNR_{ε}. Imaging the subject at multiple compression levels could allow partial optimization of this tradeoff by retrospectively choosing the elastogram with greatest lesion contrast and least breathing motion. However, this should not be a major concern with this system, as only 17% (2 of 12) *in*

vivo scans resulted in modest artifacts in the 3D elastogram which were caused by breathing motion and not present in the 2D elastogram. As demonstrated in Fig. 5.7, when breathing motion is minimized, efficacy of full 3D tracking is realized, and the resulting improved SNR in the 3D elastogram improves lesion visibility as well as boundary definition. Because previous literature studies have demonstrated that lesion size in the elastogram could distinguish malignant from benign solid masses, 3D elastography may improve the reliability of that technique by increasing margin sharpness.

5.5.2. Non-simple Cyst Characterization Using the Differential Correlation Coefficient Derived from 2D Elastography

The high DCC values (12-40%) observed in the cysts in this study were due to the decorrelating nature of the noise, artifacts, fluid-debris, and particulate matter in the interior of cysts. All of these move randomly or more quickly under compression than actual tissue thus cannot be tracked using conventional elastography. Due to partial volume averaging, sidelobes, specular reflection, and multiple scattering, cyst edges stayed somewhat correlated between frames, “filling in” the cyst in the DCC image. In larger cysts, this effect had little impact on the overall DCC. This finding might have diagnostic utility, being the reverse of cancers which reportedly frequently look larger in elasticity images than in grayscale [23]. Lesion depth appeared to impact DCC values more than lesion size, most likely because lower SNR at greater depths reduces the efficacy of speckle tracking. The spotty and random highly correlated regions in the cyst were caused by particulate matter and reverberations which did not completely

decorrelate. Sources of the reverberations were often easy to identify in the original grayscale ultrasound image, however, so these regions could be retrospectively removed from the original ultrasound images or the resulting DCC images.

The differential correlation coefficients measured in both fibroadenoma and cancer images were significantly lower than in cyst images. This was as expected because in most cases, even hypoechoic solid lesions contain more true speckle than cysts with no discrete solid components. These structures are solid so they have real, discernable elastic properties, which keep the speckle correlated. The high variability of DCC values in fibroadenomas is consistent with reports that fibroadenomas exhibit both soft and hard regions in elastograms, which can decorrelate to varying degrees [23].

The technique we have presented here is similar to the acoustic streaming method investigated by Nightingale et al. [36]. That study successfully used high intensity ultrasound to move low level internal echoes in cysts and detect them with Doppler methods to differentiate them from solid lesions. Our differential correlation coefficient technique should not require the high intensities used in that study and is responding to different tissue properties. It may be additionally efficacious in cysts which contain cells too large to be moved solely by the energy of the ultrasound beam, such as red blood cells, white blood cells, epithelial cells, and apocrine cells [9]

An additional advantage to this technique is that it should be independent of preload. Though tissue elasticity contrast decreases with preload due to the nonlinearity of tissue, the correlation coefficient in a cyst will be low regardless of preload. This is because preload effects are a manifestation of the non-linearity of Young's modulus and cysts have a zero Young's modulus. Any speckle in a cyst is either noise or moves

randomly when compressed, independent of the level of pre-compression and thus strain measured in a cyst must be noise.

This preliminary study had several limitations. First, imaging with our stand alone mammography-mimicking system limited visualization of breast lesions to the CC view, which sometimes increased the imaging depth of the lesions. Solid masses which are highly hypoechoic exhibit greater differential correlation coefficients (more decorrelation) and smaller cysts exhibit lower differential correlation coefficients because partial volume averaging would play a greater role. These masses are not ideal for this imaging technique. Deeper solid masses also decorrelate more quickly because of low ultrasound SNR at greater depths, an effect sometimes emphasized in this study by imaging through the mammographic paddle rather than the position which placed the lesion closest to the transducer. However, use of a horizontal rotational axis as on standard mammographic systems and our combined ultrasound/mammography system or use of free-hand ultrasound, as would generally be done clinically on a real-time elastography scanner would eliminate this limitation for cases in which the CC mammographic view is not ideal. In addition, freehand scanning would be expected to only increase the amount of available signal in solid masses, thus improving the discrimination between cyst and solid beyond what we have detected. In some sense, we have defined, within statistical limitations, a lower bound for the differentiation between cystic and solid masses.

As a preliminary study, we did not preferentially select any of the lesions for analysis. But future studies could preferentially select human subjects with cancers which are cystic in appearance (round, non-spiculated cancers) and hypoechoic to assess the full

utility of this cyst/solid differentiation technique. An additional limitation of this preliminary study was that only 30% of the cysts analyzed were aspirated. Because some complex cysts can have solid components, future studies should also aspirate and/or biopsy all cysts after imaging to fully understand the DCC values in fluid versus mixed fluid/solid lesions.

In the future, this technique could be applied with multi-slice full 3D elastography. This should further reduce the correlation coefficient in the cysts while maintaining the background correlation coefficient, thus causing the overall DCC in cysts to increase. Both the increased kernel size and the increased scanning time inherent in 3D imaging would contribute to these increased values.

The goal of this technique, and of most clinical importance, is whether it can differentiate non-simple cysts from cancerous lesions. This differentiation could result in a reduction in the number of cysts that require aspiration or biopsy and could be especially efficacious in women with multiple lesions. Coupled with the potential to reduce interventions in benign masses is the opportunity to reduce costs and time associated with those procedures. Because localized breast sonography is ¼ the cost of cyst aspiration, this could tremendously reduce clinical costs [5].

Even with a small study size (N=20), the DCC differences between cysts and cancers are statistically significant. Based on these values, a threshold between benign and malignant lesions could be set for future studies to DCC = 20%. Because the greatest DCC value exhibited by a cancer in this study was 6.7%, there is no evidence that false-negatives would be created with this technique. Only one cyst fell below this threshold (DCC = 12.1%).

Based on this promising preliminary data, which demonstrates the feasibility of this technique, this study will hopefully lead the way toward larger, dedicated clinical trials. Additional factors of cyst characterization, such as signal level and increased through-transmission, could be combined with differential correlation coefficient values for improved cyst identification.

5.5.3. Reader Study Evaluation of the Clinical Utility of Elastography

The results of the reader study in this dissertation also suggest that elastography may play a greater clinical role in increasing the likelihood that a benign mass is benign, rather than distinguishing a malignant mass from a benign mass. Of 9 of 12 cysts which were given a BI-RADS score of 3 or 4, the score was reduced to BI-RADS = 2 in 4 of the 9 (44%) which would eliminate the need for biopsy or aspiration of those cysts. In contrast, no fibroadenoma or cancer was given a BI-RADS score less than a 3 for any modality or by any reader, and thus all fibroadenomas and cancers would be sent to biopsy regardless of the addition of ultrasound or elastography to the readings. Only 25% (2 of 8) of malignant lesions appeared more malignant after reviewing elasticity images. This was partly due to the fact that the cancers in this study did not appear markedly stiffer than their surrounding tissue, as some previous literature studies had reported [22-23]. However, this was also due to the fact that mass stiffness is a characteristic that can overlap between mass types, with some cysts, many fibroadenomas, and most cancers appearing stiffer than healthy tissue [22]. Thus, the readers were not confident in characterizing breast lesions based on the characteristic of stiffness alone. Additionally,

comparing the lesion size in the elastogram versus the sonogram produced mixed results for malignant lesions, and produced a false positive result in 5 of 12 fibroadenomas.

In contrast, after reviewing elasticity results, the BI-RADS score for cysts fell from 3.2 to 2.8. This was entirely due to the readers using the differential correlation coefficient to measure whether a mass was cystic or solid. These results are particularly encouraging because a mass with a BI-RADS score < 3 can often be managed with follow-up rather than intervention, reducing clinical costs and time. Reader study results were consistent with quantitative measures, which was also encouraging.

5.6. Conclusions

Cysts, fibroadenomas, and carcinomas are the most common masses in the female breast and reliable differentiation of these masses is of great clinical importance [5, 37]. When breathing motion is sufficiently minimized, high quality 2D and 3D elastography can be achieved *in vivo.* In 3D, increases in breast lesion elastogram contrast improved lesion detectability and boundary visibility. Recent 2D breast elastography studies have indicated that many invasive cancers can appear larger in the elastogram than the grayscale image, due to the desmoplasia associated with the mass [23]. However, lesion boundaries are not always well defined. Thus the potential for this means of lesion characterization could be enhanced with 3D elastography.

The low malignancy rate of non-simple cysts which contain no solid components suggest that they can be monitored through 6-month or 1-year follow up imaging studies, rather than intervention when reliably characterized [10]. As the number of non-simple cysts observed clinically continues to increase due to increased sensitivity of ultrasound

imaging to small debris in the fluid, non-invasive methods to distinguish these cysts from solid breast lesions, including cancers and fibroadenomas, will become increasingly valuable.

The differential correlation coefficient exploits the decorrelating nature of noise, artifacts, and particulate matter found in non-simple cysts to differentiate them from solid lesions or cystic lesions with solid components. In contrast, solid tissue components, in solid masses or in cysts with solid components, contain true speckle which will stay correlated even when external compression is applied. This technique is essentially an independent imaging method for confirming a breast mass is a cyst. Though the sonographic appearance of non-simple cysts can overlap with that of solid breast lesions, the DCC values in cysts are statistically different from solid lesions. Thus, differential correlation coefficient measures should increase confidence that a lesion is 1) a cyst and 2) that it does not contain solid components. This increase in confidence could reduce aspiration of non-symptomatic complicated cysts and change management options toward follow-up imaging.

The following is a summary of the elastographic appearance of the different masses in this study, according to the results of the reader study.

Cysts appeared harder or much harder in elastograms when they were not dominated by peakhop artifacts due to their lower correlation coefficient values. This is consistent with our experience in palpation. They were always smaller or similar in size in the elastogram compared with the sonogram. They exhibited sharp, smooth and round margins and occasional boundary flow (increased tissue motion at the boundary under

changing compression). They consistently had a correlation coefficient much lower than in the surrounding tissue.

Fibroadenomas were mostly harder or much harder than surrounding tissue and occasionally larger in elastograms than sonograms. They had primarily irregular borders and varying margin definition. They occasionally exhibited boundary flow. They mostly exhibited differential correlation coefficients slightly lower or lower than in surrounding tissue.

The small number of cancers in this study exhibited highly variable elastographic appearances, appearing both larger and smaller in elastograms than sonograms and both harder and similar stiffness compared with surrounding tissue. However, they always exhibited irregular borders and mostly had indistinct margins. They never exhibited boundary flow.

In all, the results of these studies suggest that elastography might play a greater role in improving confidence that a benign lesion is benign, particularly in cases of benign cysts, rather than distinguishing malignant from benign masses. Of greatest potential seems to be the differential correlation coefficient measure, which can distinguish complicated cysts from solid masses.

5.7. References

[1] Gisvold JJ, Marin JK Jr. Prebiopsy localization of nonpalpable breast lesions. AJR 1984; 143:477-481.

[2] Rosenberg AL, Schwartz GF, Feig SA, Patchefsky AS. Clinically occult breast lesions: localization and significance. Radiology 1987; 162: 167-170.

[3] Bassett LW, Liu TH, Giuliano AI, Gold RH. The prevalence of carcinoma in palpable vs impalpable, mammographically detected lesions (comment). AJR 1992; 158: 688-689.

[4] Bassett LW, Kimme-Smith C. Breast sonography. AJR Am J Roentgenol 1991; 156:449-455.

[5] Hilton SV, Leopold GR, Olson LK, Willson SA. Real-time breast sonography: application in 300 consecutive patients. AJR Am J Roentgenol 1986; 147:479-486.

[6] Jackson VP. The current role of US in breast imaging. Radiol Clin North Am 1995; 33:1167-1170.

[7] Sickles EA, Filly RA, Callen PW. Benign breast lesions: ultrasound detection and diagnosis. Radiology 1984; 151:467-470.

[8] Berg WA, Campassi CI, Ioffe OB. Cystic lesions of the breast: Sonographic-pathologic correlation. Radiology 2003; 227:183-191.

[9] Stavros AT. Sonographic evaluation of breast cysts. In: Breast Ultrasound. Philadelphia, PA: Lippincott Williams & Wilkins, 2004; 276-350.

[10] Venta LA, Kim JP, Pelloski CE, Morrow M. Management of complex breast cysts. AJR Am J Roentgenol 1999; 173:1331-1336.

[11] Mendelson EB, Berg WA, Merritt CR. Toward a standardized breast ultrasound lexicon, BI-RADS: ultrasound. Semin Roentgenol 2001; 36:217-225.

[12] American College of Radiology (ACR). Breast imaging reporting and data system (BI-RADS). Reston, VA: American College of Radiology; 2003.

[13] Jackson VP. The role of US in breast imaging. Radiology 1990; 177:305-311.

[14] Parker SH, Jobe WE. Percutaneous breast biopsy, 1st ed. New York: Raven, 1993: 111-114.

[15] Helvie MA, Bude RO, Joynt L, Naylor B, Rubin JM. In Vitro Sonographic Evaluation of Aspirated Hypoechoic and Anechoic Breast Cyst Fluid. Breast Dis 1996; 9:15.

[16] Stavros AT, Thickman D, Rapp CL, Dennis MA, Parker SH, Sisney GA. Solid breast nodules: use of sonography to distinguish between benign and malignant lesions. Radiology 1995; 196:123-134.

[17] National Comprehensive Cancer Network (NCCN). Breast cancer screening and diagnosis; 2007.

[18] Buchberger W, DeKoekkoek-Doll P, Springer P, Obrist P, Dunser M. Incidental findings on sonography of the breast: clinical significance and diagnostic workup. AJR Am J Roentgenol 1999; 173:921-927.

[19] Kolb TM, Lichy J, Newhouse JH. Occult cancer in women with dense breasts: etection with screening US – diagnostic yield and tumor characteristics. Radiology. 1998; 207:191-199.

[20] Louie L, Velez N, Earnest D, Staren ED. Management of nonpalpable ultrasound-indeterminate breast lesions. Surgery 2003; 134:667-673.

[21] Merritt C, Piccoli C, Forsberg F, Wilkes A, Cavanaugh B, Lee S. Real-time spatial compound imaging of the breast: clinical evaluation of masses (abst.) Radiology 2000; 217:491-492.

[22] Garra BS, Cespedes EI, Ophir J, Spratt SR, Zuurbier RA, Magnant CM, Pennanen MF. Elastography of breast lesions: initial clinical results. Radiology 1997; 202:79-86.

[23] Hall TJ, Zhu Y, Spalding CS. In vivo real-time freehand palpation imaging. Ultrasound Med Biol 2003; 29:427-435.

[24] Barr RG. Clinical applications of a real time elastography technique in breast imaging. Proceedings of the 5th International Conference on the Ultrasonic Measurement and Imaging of Tissue Elasticity. 2006; p. 112.

[25] Lyshchik A, Higashi T, Asato R, et al. Thyroid Gland Tumor Diagnosis at US Elastography. Radiology 2005 237: 202-211.

[26] Rubin JM, Xie H, Kim K, Weitzel WF, Emelianov SY, Aglyamov SR, Wakefield TW, Urquhart AG, O'Donnell M. Sonographic elasticity imaging of acute and chronic deep venous thrombosis in human. J Ultrasound Med 2006; 25:1179-1186.

[27] Sinha SP, Goodsitt MM, Roubidoux MA, Booi RC, LeCarpentier GL, Lashbrook CR, Thomenius K, Chalek CL, Carson PL. Automated ultrasound scanning on a dual-modality breast imaging system: coverage and motion issues and solutions. J Ultras Med. 2007; 26(5):645-55.

[28] Booi RC, Krucker JF, Goodsitt MM, O'Donnell M, Kapur A, LeCarpentier GL, Roubidoux MA, Fowlkes JB, Carson PL. Evaluating thin compression paddles for

mammographically compatible ultrasound. Ultrasound Med Biol 2007; 33(3):472-482.

[29] Kapur A, Carson PL, Eberhard J, Goodsitt MM, Thomenius K, Lokhandwalla M, Buckley D, Roubidoux MA, Helvie MA, Booi RC, LeCarpentier GL, Erkamp RQ, Chan HP, Fowlkes JB, Thomas JA, Landberg CE. Combination of digital mammography with semi-automated 3D breast ultrasound. Technol Cancer Res Treat 2004; 3:325-334.

[30] Kaluzynski K, Chen X, Emelianov SY, Skovoroda AR, O'Donnell M. Strain rate imaging using two-dimensional speckle tracking. IEEE Trans Ultrason Ferroelectr Freq Control 2001; 48:1111-1123.

[31] Lubinski M, Emelianov S, O'Donnell M. Speckle Tracking Methods for Ultrasonic Elasticity Imaging Using Short-Time Correlation. IEEE Trans Ultrason Ferroelectr Freq Control 1999; 46:82-96.

[32] O'Donnell M, Skovoroda AR, Shapo BM, and Emelianov SY. Internal displacement and strain imaging using ultrasonic speckle tracking. IEEE Trans Ultrason Ferroelectr Freq Control 1994; 41:314-325.

[33] Regner DM, Hesley GK, Hangiandreou NJ, et al. Breast lesions: evaluation with ultrasound strain imaging – clinical experience of multiple observers. Radiology 2006; 238(2): 425-437.

[34] Chen X, Xie H, Erkamp R, et al. 3-D correlation-based speckle tracking. Ultrason Imaging 2005; 27(1):21-36.

[35] Bilgen, M. Target detectability in acoustic elastography. IEEE Trans on Ultras, Ferro, and Frequency Contr 1999; 46:1128-1133.

[36] Nightingale KR, Kornguth PJ, and Trahey GE. The use of acoustic streaming in breast lesion diagnosis: a clinical study. Ultrasound Med Biol 1999; 25:75-87.

[37] Harper P. Ultrasound mammography. Baltimore: University Park Press, 1985.

[38] Jiang J and Hall TJ. A novel lateral motion tracking algorithm and its application in shear strain imaging: a feasibility study. Proceedings of the 5th International Conference on the Ultrasonic Measurement and Imaging of Tissue Elasticity. 2006; p.107.

[39] Booi RC, Carson PL, O'Donnell M, Richards MS, Rubin JM. Diagnosing cysts with correlation coefficient images from 2D freehand elastography. Journal of Ultrasound in Medicine 2007 *(in press)*.

[40] Booi RC, Carson PL, O'Donnell M, Roubidoux MA, Hall AL, Rubin JM. Characterization of cysts using differential correlation coefficient values from 2D and 3D elastography. Ultrasound in Medicine and Biology 2007 *(in press).*

CHAPTER 6

CONCLUSIONS AND FUTURE WORK

6.1. Experimental Conclusions: 2D and 3D Mammographically-Compatible Ultrasound Elastography

The primary goals of the research in this dissertation were to conduct 2D and 3D ultrasound elastography through a mammographic paddle, to assess the quality of the resulting elastograms and correlation coefficient images, and to determine the utility of through-paddle elastography in conjunction with a combined ultrasound/digital tomosynthesis mammography system for improved breast lesion characterization.

Original contributions of this dissertation are summarized below:

Contribution 1: Sonographic imaging through a mammographic paddle with favorable acoustic properties produces only mild degradations in image quality, and these degradations have minimal clinical impact. Under these best case conditions, through-paddle elastography is feasible. Sonographic image quality through nine mammographic paddles of varying materials (lexan, TPX, mylar, and polyurethane) and thicknesses (0.25 mm – 2.5 mm) were compared with direct-contact (no paddle) image quality in the areas of spatial resolution, sidelobe levels, range lobe levels, contrast, and signal strength. TPX paddles $\leq$ 2.5 mm thick performed best in virtually all areas, resulting in < 5% spatial resolution reduction, no increase in range lobe levels, < 3 dB contrast loss, and < 6 dB signal strength loss. Some of the signal loss could potentially be recovered since the

acoustic output is ultimately limited by FDA guidelines and the losses on transmission could be compensated by increasing output. When imaging through these paddles *in vivo*, 83% of cases produced image quality as good as or better than their direct-contact analogues. One limitation of the study in this chapter is that it did not incorporate signal losses due to the hairspray adhesive which was used in future *in vivo* studies. This limitation, plus the removal of the beamforming corrections in future implementations of the software, as well as general positioning and coupling issues have resulted in less promising results from more recent studies.

It should be noted that there probably exist other mammographic paddles which would also produce high quality ultrasound images besides those tested, depending on the desired applications and future paddle options should be explored. However, the performance of the TPX paddles was well suited with the multitude of imaging modalities – tomosynthesis, B-mode ultrasound, elastography, and ColorFlow Doppler – employed with the combined system.

Results of this work are published in [1] and [2].

Contribution 2: When employed with appropriate transducer type, frequency, through the TPX 2.5 mm paddle, at depths < 4 cm, and with high quality acoustic coupling, 2D through-paddle elastography produces correlation coefficient images and elastograms comparable to freehand elastography for strain step sizes < 0.5%. As with most engineering endeavors, there are tradeoffs between through-paddle elastography and freehand elastography, and the choice of which to use will depend on the goal. Correlation coefficient values for freehand elastography degrade more slowly as a function of strain step size than for through-paddle elastography at step sizes > 0.5% in

phantom studies, and strain SNR increases with step size up to the 3% strain step tested. It is likely that the small degradations in beam quality due to imaging through the mammographic paddle reduce elastography image quality more profoundly than conventional ultrasound image quality. However, the utility of freehand elastography advantages may not be realized *in vivo* with breast imaging because of the low SNR in breast ultrasound images. Thus, it is likely that through-paddle elastography will be more than adequate for clinical breast imaging requirements. Additionally, 2D through-paddle elastography consistently produced high quality strain images at these lower step sizes, regardless of operator skill.

Because compressions are automated, optimal step size can be induced at each frame-to-frame compression. In contrast, compression with freehand elastography must be conducted by an experienced operator and frame-to-frame compressions of poor tracking, from too large a frame-to-frame step size or unintentional transducer rotation during compression, must be retrospectively removed from analysis. Through-paddle elastography also allows a natural extension from the 2D technique to the 3D technique, and direct comparison of elastography results with tomosynthesis and B-mode ultrasound images which can be acquired at essentially the same time and in the same orientation with the combined system to maximize the information obtained from each imaging mode and modality.

Results of this work are published in [3].

Contribution 3: High quality, through-paddle 3D elastography can be conducted using a 1D array translated over a small 3D volume via stepper motor control. The resulting 3D elastograms have increased SNR, reduced decorrelation, and reduced image

artifacts compared with their 2D analogues. Extending elastography to three dimensions is a necessary step to realize the full potential of this novel diagnostic technique and for final, accurate elastic modulus reconstruction. In the future, 3D elastography can and should eventually be conducted using a 2D array; 1D arrays are currently less expensive and more available. Out-of-plane motion is small (< 0.4 mm for a 3% strain step) when the breast is pre-compressed for through-paddle elastography, but even this small amount of elevational motion degrades strain images and correlation coefficients. Implementing 3D elastography improved elastogram SNR over its 2D analogue, which may be especially efficacious for imaging poorly visible breast masses.

Results of this work are published in [4].

Contribution 4: This dissertation introduced the elasticity characteristic "differential correlation coefficient" for distinguishing between complicated cysts and solid masses. The differential correlation coefficient is defined as the difference in correlation coefficient values between a mass and its surrounding tissue for 0.3%-0.6% step sizes and exploits the severe decorrelation observed in most cysts under compression. In the small clinical study conducted in this thesis, this characteristic has demonstrated potential to reduce the BI-RADS score of a complicated cyst, suggesting it could be managed with imaging follow-up rather than biopsy or aspiration. Preliminary work has shown that the correlation coefficient in cysts is 27% lower than surrounding tissue on average, compared with 5.9% lower in fibroadenomas, and 3.8% lower in cancers. Setting a differential correlation coefficient threshold at 20% in this study produced one cyst which appeared solid, and one fibroadenoma which appeared cystic. Because there were no false-negatives, these preliminary results are encouraging. In the

future, real-time elasticity display formats could be modified to combine the complementary information produced by the differential correlation coefficient image and elastogram. During a reader study of the 2D data, of 9 of 12 cysts which were scored a BI-RADS score of 3 or 4, and thus biopsy would have been expected, 4 of the 9 (44%) were lowered to a non-biopsy certainty level (BI-RADS = 2) by analysis of the DCC image. Note that no fibroadenoma or cancer was given a BI-RADS score less than a 3 for any modality or by any reader, and thus all fibroadenomas and cancers would be sent to biopsy regardless of the addition of ultrasound or elastography to the readings.

Results of this work are published in [5] and [6].

Contribution 5: Appearances of the most common clinically observed breast masses (cysts, fibroadenomas, and cancers) have been evaluated and compared with previous literature results and potential characteristic appearances have been identified. Based on readings by 2 trained radiologists, most masses, regardless of type, were identified as stiff as or much stiffer in elastograms than the surrounding tissue. Thus, this may not be the best characteristic to distinguish malignant and benign masses. Most cysts exhibited smooth, round, and sharp margins, whereas most fibroadenomas and all cancers exhibited irregular margins. No cancers exhibited boundary flow but several fibroadenomas and cysts did. Additionally, as previously described, the differential correlation coefficient was much lower or lower in all cysts, a characteristic not observed in fibroadenomas or cancers.

Limitations of the work conducted in this dissertation have been discussed in previous chapters, but will be reiterated here. Most importantly, the full clinical utility of through-paddle elastography and the differential correlation coefficient measure for

distinguishing cystic/solid masses should be explored in a larger clinical trial than was available for this dissertation. Additional subjects with carcinomas of varying severity should be recruited and the elastographic characteristics of their masses should be explored. Ultimately, specificity, sensitivity, and area under the Receiver Operating Characteristic curve (ROC curve) should be determined, particularly for differential correlation coefficient values, to test true clinical utility.

Though ultrasound image quality is minimally degraded by imaging through the mammographic paddle, one of the greatest remaining imaging challenges with this system is the way it restricts access to different parts of the compressed breast. Masses close to the chest wall and in the areolar region are particularly difficult to image, and sometimes cannot be visualized at all. Additionally, because imaging can only be conducted over 5 views (lateral-medial (LM), medial-lateral (ML), cranial-caudal (CC), lateral-medial-oblique (LMO), and medial-lateral-oblique (MLO)), often the mass of interest is located deeper in the through-paddle image than in the direct-contact ultrasound image. A current limitation of the stand-alone mammography-mimicking unit used in elasticity studies is that it can only image in the CC view. Because signal attenuation is more pronounced with increased depth, this contributes more to reduced image quality than the small degradations created by the mammographic paddle itself. Minimizing or circumventing these effects is especially critical for through-paddle elastography, as a number of subjects had to be excluded from analysis because of these restrictions. Future work should include modifying this unit to permit rotation of the paddle to image from additional views.

In conclusion, quality 2D and 3D through-paddle elastography has been conducted both in a tissue-mimicking phantom and *in vivo*. Breast mass information has been extracted from both the resulting correlation coefficient images and elastograms, and has shown potential as an adjunct to x-ray tomosynthesis and ultrasound in the breast imaging environment. Potential future directions of this research are discussed below.

6.2. Future Experimental Directions

6.2.1. Crossbeam Elastography for Improved Lateral Displacement Estimates

A disadvantage of current elasticity imaging is that only the axial component of the strain tensor is used to produce the elastogram. This is because lateral displacement measurements are much less accurate than axial ones due to the anisotropy in spatial frequencies associated with diffraction limited ultrasonic imaging [1]. However, for clinical elastography, lateral displacements cannot be ignored because tissue motion inevitably occurs in three directions. Additionally, the conical shape and heterogeneous fatty and fibroglandular structure of many breasts creates significant lateral motion while the breast is being compressed. Thus, shear strains may provide additional elastographic information regarding the mass of interest. Accurate lateral displacement measurements would be required for shear strain imaging, suggesting improvements in lateral displacement estimates are needed.

Methods to improve lateral displacement estimates with 2D speckle tracking algorithms have been proposed in the past [7]. Alternatively, crossbeam elastography could be applied to estimate lateral and shear tensor components while improving SNR_{ε}

and reducing noise artifacts [8-10]. Crossbeam elastography acquires displacement vectors from different insonification angles, then separates the estimated displacements into vector components along the original axial and lateral directions. As in conventional elastography, these displacement estimates can then be accumulated and converted into strain images. Analogous to B-mode compounding, the proposed data acquisition for this technique is illustrated in Fig. 6.1 [8-10].

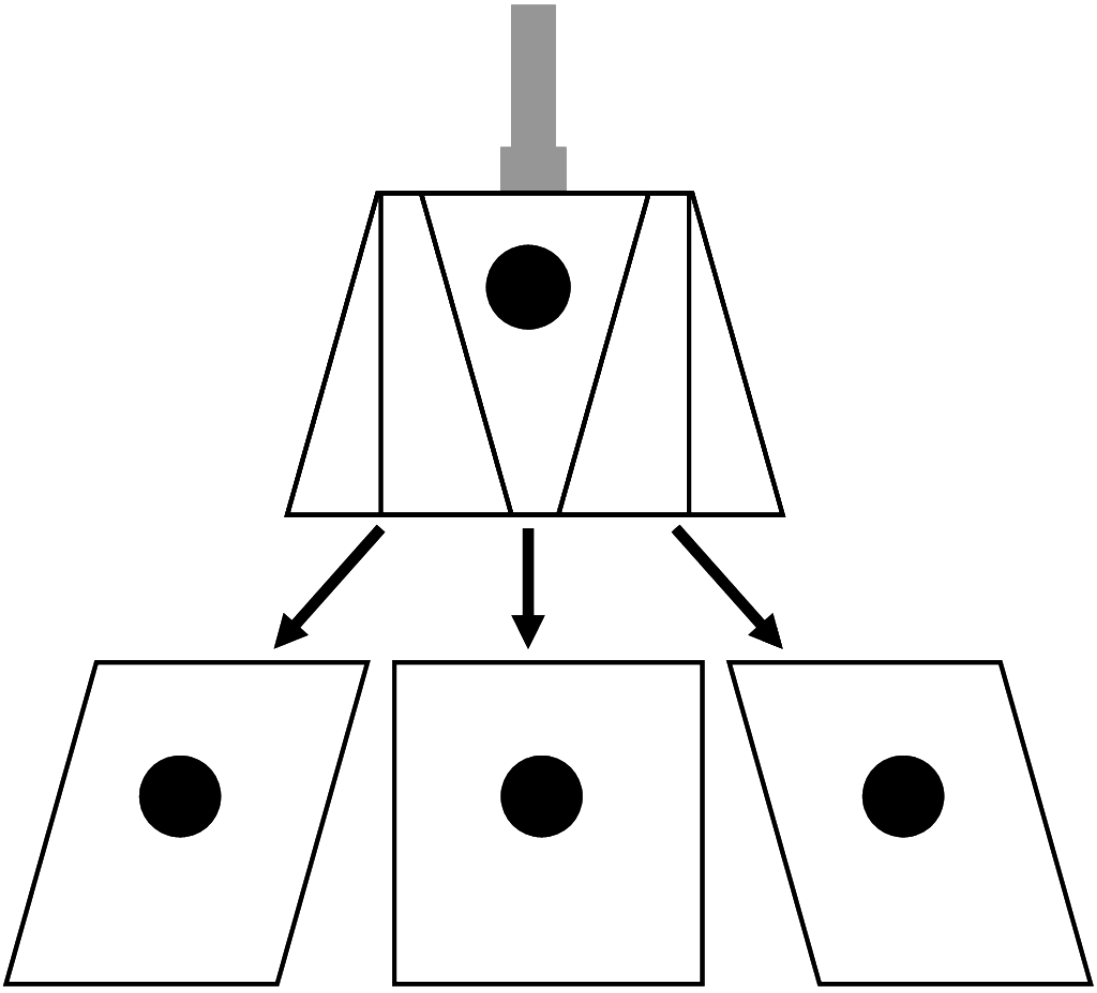

Fig. 6.1: Crossbeam elastography data acquisition for three different insonification angles. Displacements estimated from these angles could be scan converted to original lateral and axial directions. Then, the displacements will be converted to strains, creating a final image with improved CNR_{ε} and reduced noise errors.

Assuming perfect beamforming, the "crossover angle" – the minimum angle required to reduce the variance in the lateral displacement estimates – can be calculated

as function of F-number (the ratio of depth to the size of the transducer aperture) according to the equation:

$$\frac{\sigma_{lateral}^2}{\sigma_{axial}^2} = \cot^2(\theta) < 40\, fnum^2 \qquad \textbf{(6.1)}$$

where $\sigma_{lateral}^2$ and σ_{axial}^2 are the variance of the lateral and axial displacement estimates, respectively, θ is the crossover angle (degrees), and *fnum* is the F-number of the system. The 10L transducer at 7.5 MHz has an *fnum* = 1.1, and thus under these imaging conditions, the crossover angle is 8.2°. Crossover angle as a function of F-number (F#) is displayed in Fig. 6.2.

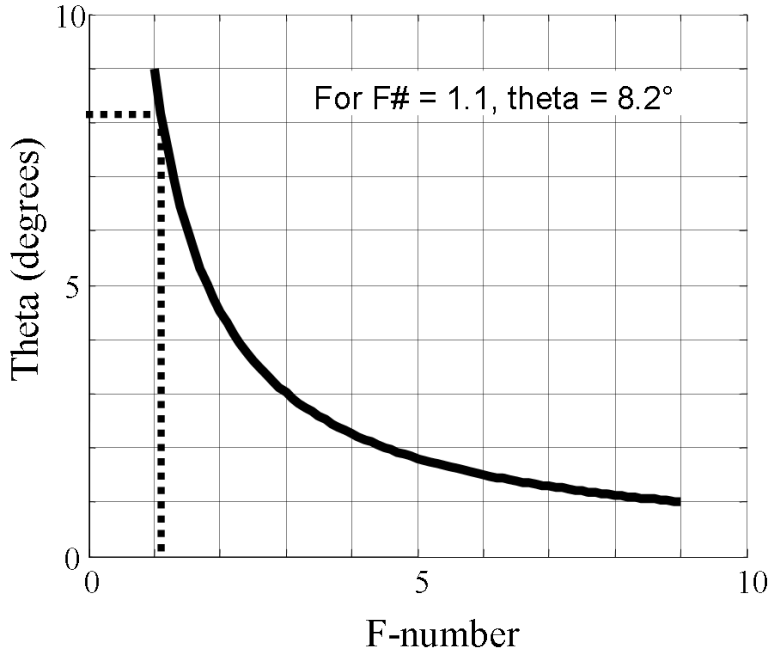

Fig. 6.2: Minimum insonification angle for which variance of lateral displacement estimates from crossbeam imaging is lower than for conventional ultrasound elastography, as a function of F-number.

To initially investigate the potential of through-paddle crossbeam elastography with the combined system, beam steering was implemented on the GE LOGIQ 9 ultrasound scanner using 3-7 insonification angles from -20° to 20°, corresponding to crossbeam "low", "medium", and "high" (Table 6.1). Beam steering is a better and more

efficient approach than mechanically angling the transducer, which could create reverberations through the mammographic paddle and degrade image quality. Additionally, it maintains more uniform compression than mechanically angling the transducer. These insonification angles also correspond to the angular ranges (12-18.75°) described in [10] as providing the biggest improvements in CNR_{ε}.

Table 6.1: Available beam steering angles for each crossbeam level on GE LOGIQ 9 scanner.

Crossbeam Level	***Available Beam Steering Angle (°)***						
Low		-15		0		15	
Medium	-20		-10	0	10		20
High	-20	-15	-10	0	10	15	20

Initial experiments were conducted on a tissue-mimicking breast phantom (model BB-1, ATS Laboratories, Bridgeport, CT, USA) using the 10L transducer at 7.5 MHz through the TPX 2.5 mm paddle, as these were the parameters determined in Chapter 4 to be most suitable for through-paddle elastography. Similar to the data acquisition for 2D through-paddle elastography, 2D crossbeam elastography data was acquired by continuously compressing the phantom at 2.5 mm/sec for 2 sec and up to 7.5% strain and continuously acquiring IQ data during that time. At each compression location, an ultrasound image at a different insonification angle was acquired (Fig. 6.3). In this way, if a total of 100 IQ images were acquired for crossbeam “medium” setting (which uses 5 insonification angles), then 20 IQ images were actually acquired for each of the 5 insonification angles.

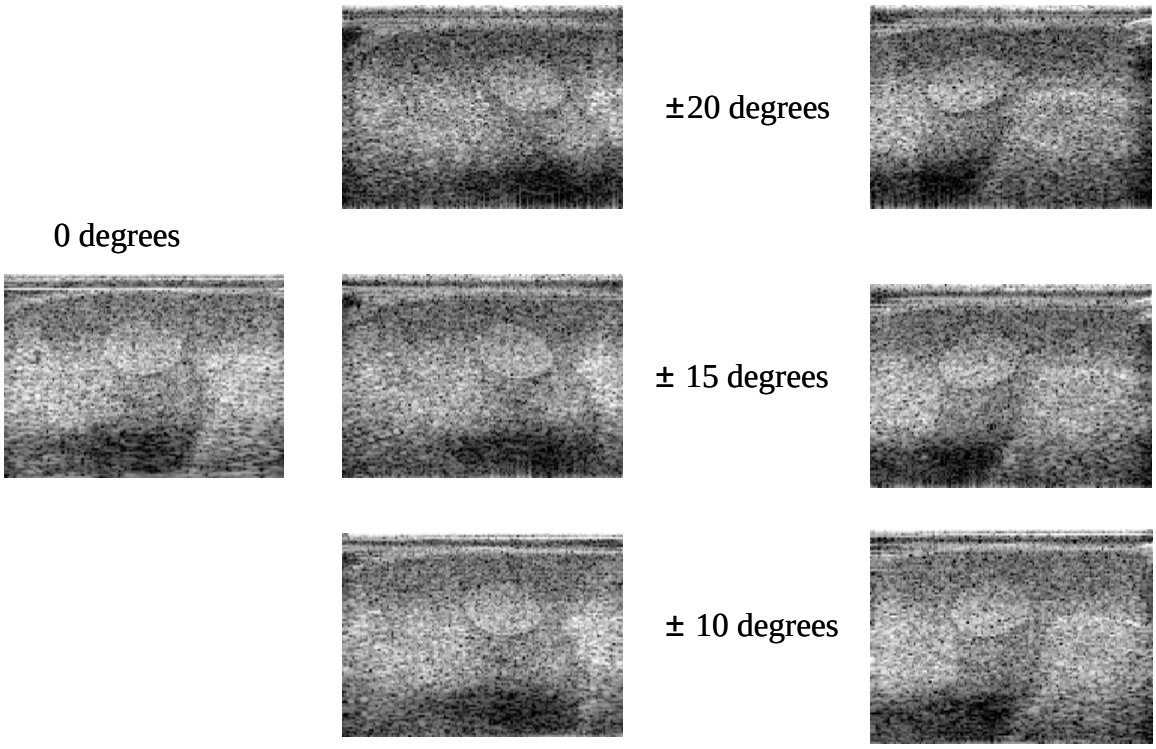

Fig 6.3: Sample grayscale images of tissue mimicking breast phantom at each insonification angle for crossbeam "high" setting.

IQ image size and cineloop length varied with crossbeam level, summarized in Table 6.2. Kernel and filter sizes were adjusted so that the kernel size in each direction was spatially equivalent to one speckle spot, and the filter size was twice the kernel size for all crossbeam levels.

Table 6.2: IQ data image size for each available crossbeam level.

Crossbeam Level	***Range Samples***	***Beams***	***Maximum Cineloop Length (Frames)***
Off	529	297	91
Low	547	199	138
Medium	561	199	138
High	561	143	192

As with conventional 2D speckle tracking, the original IQ data is upsampled axially by a factor of 4 (from a 10 MHz sampling rate to a 40 MHz sampling rate) before speckle tracking. Conventional 2D speckle tracking algorithms are then applied to corresponding frames of each insonification angle and displacement estimates are accumulated. Final results of tracking are thus one final displacement image for each insonification angle. After tracking, each displacement image is then upsampled laterally so the images contain the correct aspect ratio, and then axial and laterally downsampling to reduce calculation times for scan conversion. At this point, results are ready for scan conversion. This process is presented graphically in Fig. 6.4.

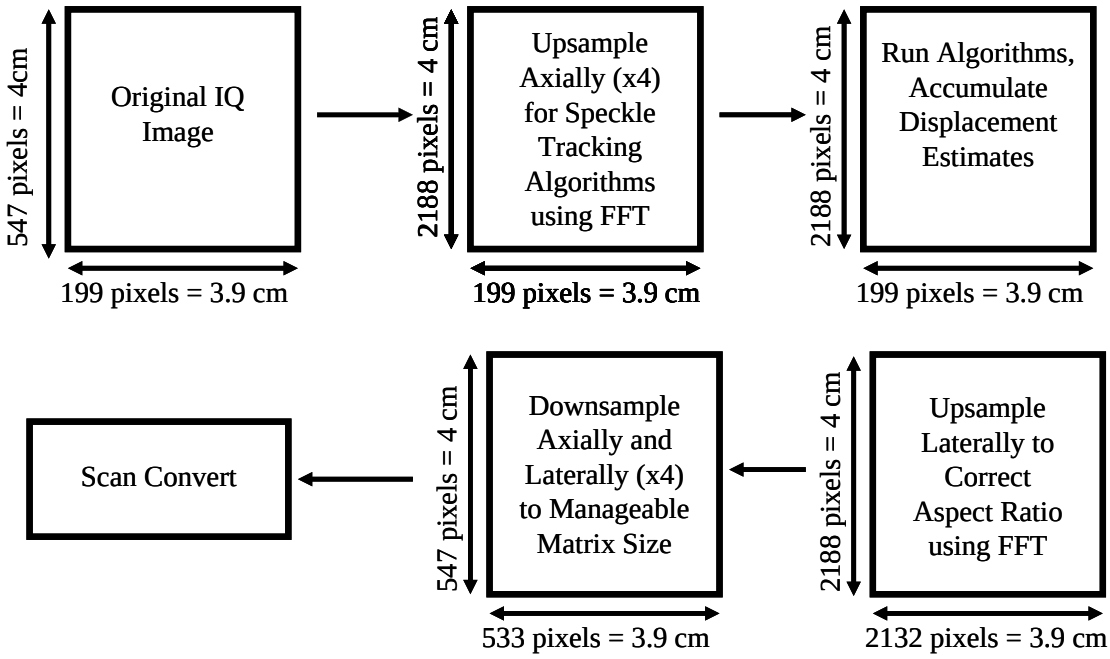

Fig. 6.4: Process of preparing IQ data for scan conversion. After speckle tracking algorithms are separately run on the data from each insonification angle and displacement estimates are accumulated, final displacement estimates must be adjusted to the correct aspect ratio before scan conversion.

Scan conversion of crossbeam displacement estimates to the original 0° geometry is a 3-step process:

- Step 1: Define the grid for (x_θ, y_θ)

- Step 2: Interpolate angled displacement estimates onto the original (x_0, y_0) grid

- Step 3: Combine results into a final displacement image incorporating all crossbeam angles

Fig. 6.5 shows the implementation of steps 1 and 2. In this figure y_0 and y_θ are the sampled positions along the axial beam direction in meters; x_0 and x_θ are the sampled positions along the lateral beam direction, in meters; θ is the insonification angle.

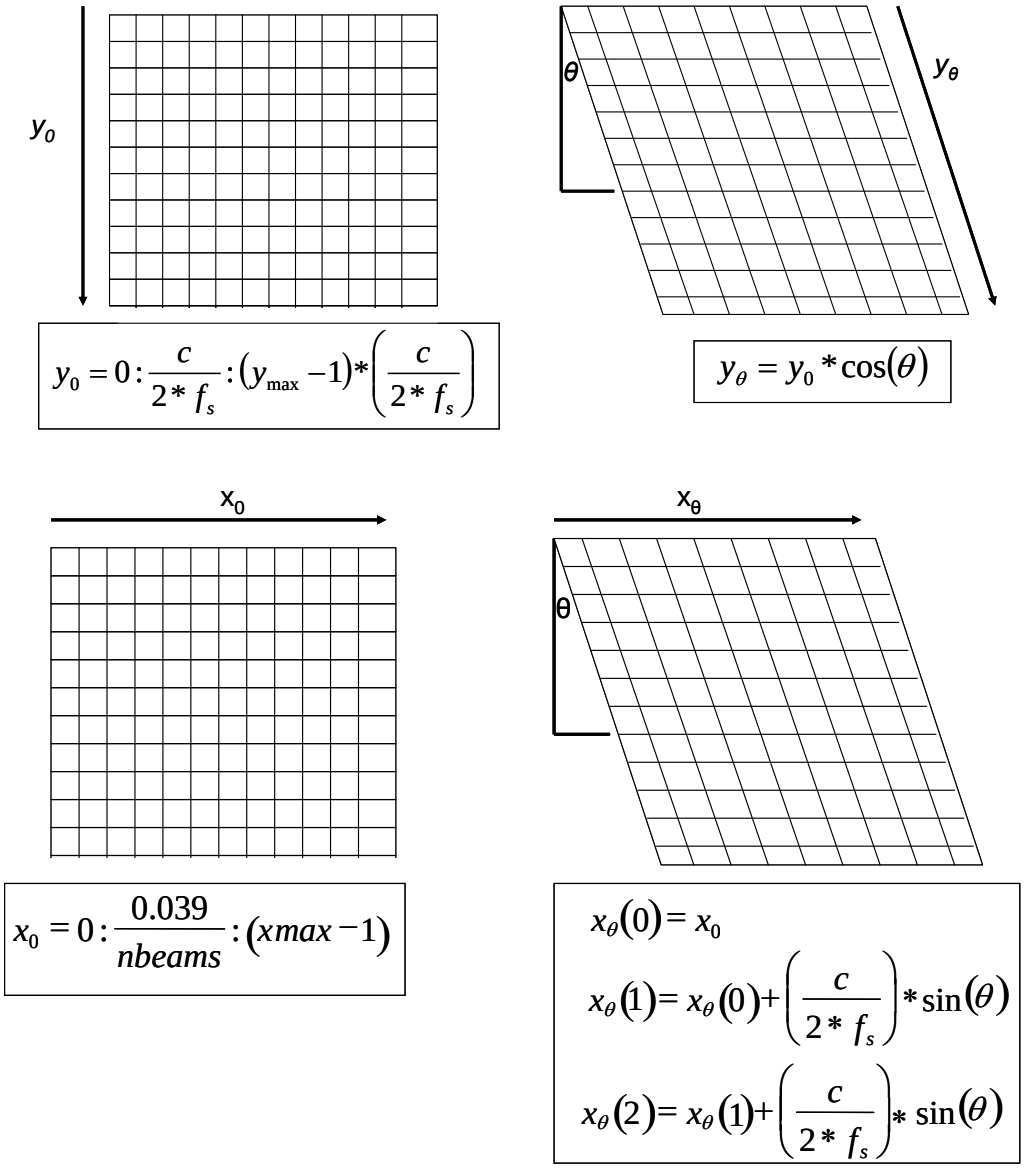

Fig 6.5: Interpolation of accumulated axial displacement estimates from varying insonification angles onto the original 0° grid.

The result of this interpolation is shown in Fig. 6.6.

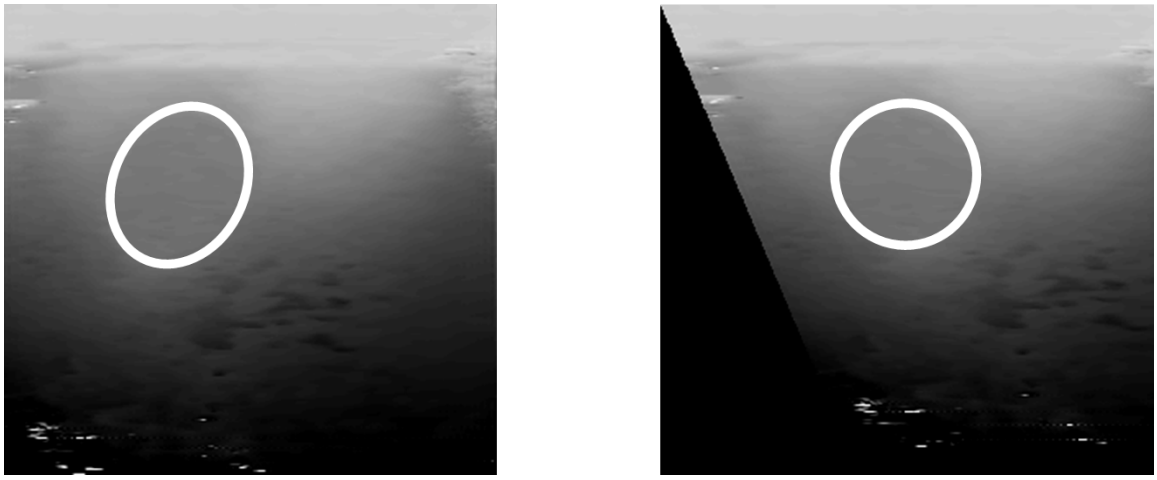

Fig. 6.6: Sample result of interpolation of displacement estimates from angled geometry to original geometry. Interpolation corrects the distortion of the circular hard inclusion (white circle).

After scan conversion, angled displacement estimates are combined to create a final displacement image (Fig. 6.7). In Fig. 6.7, q_1 and q_2 correspond to insonification angles θ and $-\theta$ and U_θ and V_θ are the original lateral and axial displacement directions, respectively. The greatest improvements in image quality are in the areas of maximum overlap and thus only these areas were displayed.

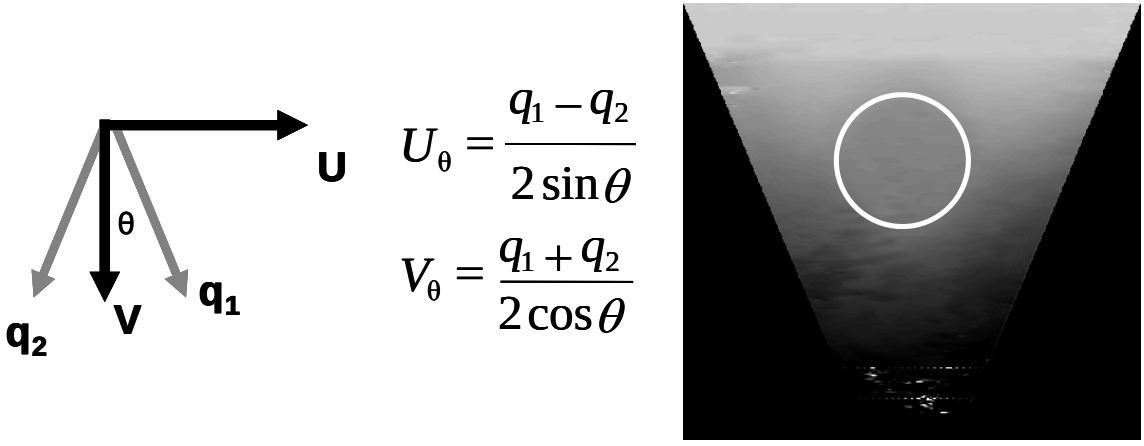

Fig. 6.7: Combination of angled displacement estimates into one final displacement image.

After scan conversion, final displacement estimates were converted into strain images as in conventional 2D elastography. Final elastograms are shown in Fig. 6.8 for

each insonification angle measured in this study. Results were disappointing and clearly image quality in the scan converted elastograms was much poorer than in the elastogram created from the 0° beam, particularly at insonification angles greater than 10°. This is most likely because image quality losses through the mammographic paddle are exacerbated at beam steered angles.

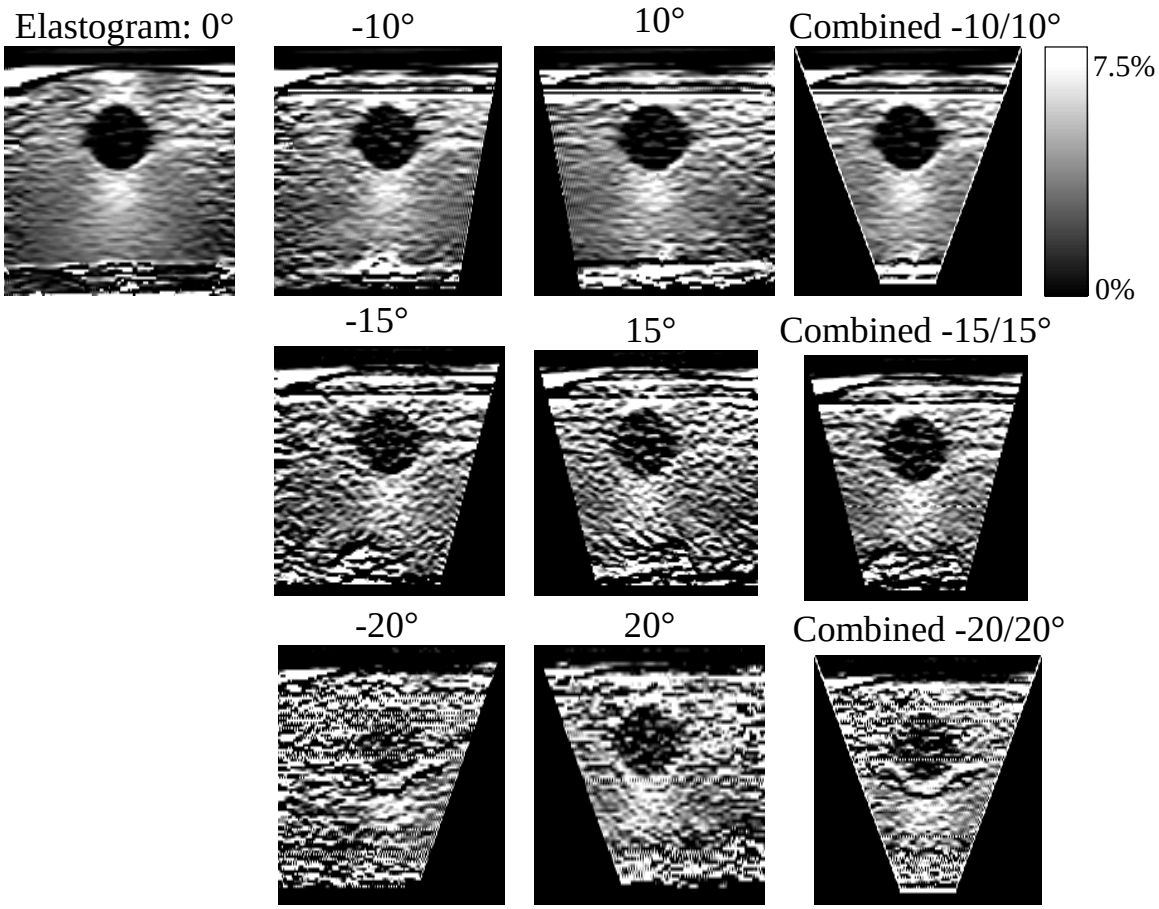

Fig. 6.8: Final elastograms created from ultrasound images created at multiple insonification angles. The poor elastogram image quality is most likely due to losses in ultrasound image quality by imaging through the mammographic paddle.

To investigate the potential of crossbeam elastography in the future, appropriate transducer requirements should first be determined. This includes determining the number of elements, pitch of the transducer, and type of transducer (linear versus phased array) necessary to acquire high quality crossbeam images. The number of insonification

angles and the degrees to which these angles should be steered should also be examined. Additionally, grating lobes may be introduced into the crossbeam images, and the effects these might have on image quality should be explored. Finally, image quality through the mammographic paddle is exacerbated by imaging at different insonification angles, and thus, through-paddle crossbeam elastography is most likely not a possibility.

6.2.2. Monitoring Carcinoma Elasticity Changes to Predict Pathologic Response to Neoadjuvent Chemotherapy

The diagnostic efficacy of elasticity imaging may also be extended to evaluate neoadjuvent chemotherapy efficacy. Neoadjuvent chemotherapy is given to patients before tumor surgery, improving breast conservation [11]. Because this kind of chemotherapy allows changes in tumor malignancy to easily be monitored, it holds potential for improving treatment efficacy. Monitoring tumor changes throughout chemotherapy would allow treatments to be tailored to each patient's needs, improving efficacy by minimizing patient exposure to ineffective and toxic drugs. Studies have also shown that a "complete pathologic response" to neoadjuvent chemotherapy is a reliable predictor of overall patient survival [11]. A complete pathologic response is defined as having no residual carcinoma, determined by biopsy.

Imaging with ultrasound alone has not been able to consistently evaluate tumor changes after neoadjuvent chemotherapy. Roubidoux et al. examined several ultrasound features to determine complete response, including grayscale image to assess mass shape and size, and ColorFlow Doppler to monitor tumor vascularity [11]. The study showed that vascularity decreased with chemotherapy but was not specific for complete response.

No vascular or B-mode ultrasound feature at initial imaging predicted complete responders. False negatives occurred with residual tumor size ≤ 6mm. False positives occurred with histologic fibrosis or biopsy changes.

Though conventional ultrasound can provide information regarding mass size and shape, it lacks histologic information that can be provided by biopsy to accurately track changes in tumor malignancy. Developing a method to evaluate tumor changes with ultrasound elastography instead of with biopsy would make chemotherapy follow-up non-invasive as well as reduce patient wait time for results. Additionally, because ultrasound is an imaging tool commonly used for breast cancer diagnosis and analysis, no additional costs would be added to the follow up procedure.

It would be interesting to investigate whether elasticity imaging could provide similar information to biopsies regarding histology. It is likely that several indicators will be necessary to predict complete response to chemotherapy. Several elasticity components as well as conventional grayscale features (i.e. mass size, shape, characteristic) could be reviewed and compared to biopsy. This combination of imaging characteristics and histology (provided by elasticity information) would give the most comprehensive analysis of the lesion. An appropriate weighting scheme should be developed to determine which combination of elements provides information to correspond to the biopsy and indicates complete response. This determination would be more comprehensive than any independent indicators.

With these goals in mind, a large clinical trial (> 50 subjects) should be designed in which the subject is imaged at four different intervals: T0 – the time when the subject is diagnosed, T1 – immediately preceding the first chemotherapy session, T2 - after the

first round of chemotherapy, and T3 – after completion of chemotherapy. A preliminary 2D elastography experiment conducted a subject at time T2 and T3 using a 10L transducer at 7.5 MHz is shown in Fig. 6.9.

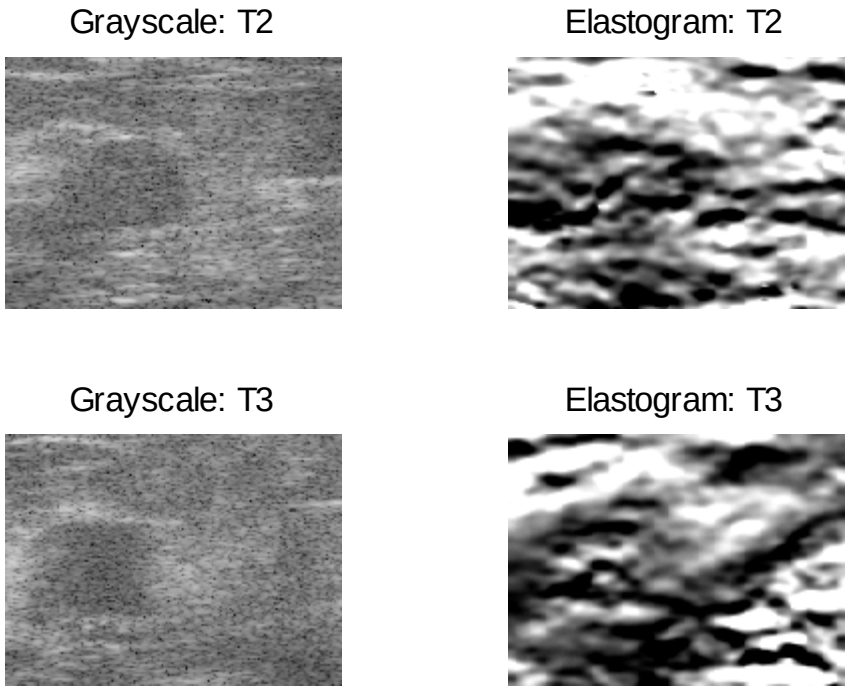

Fig 6.9: Grayscale and elastogram images of a carcinoma at time T2 (after the first round of chemotherapy) and T3 (after completion of chemotherapy). In the elastogram obtained at T2, the carcinoma is stiffer and larger in the elastogram, a characteristic observed in many carcinomas in previous studies [12-13].

As seen in this figure, the carcinoma is originally larger and stiffer in the elastogram than in the grayscale image, most likely due to desmoplasia, a property observed in previous studies [12-13]. However, after completion of chemotherapy, though the carcinoma is still present in the grayscale image, it is smaller and more heterogeneous in the elastogram than before. Relative stiffness and elastogram variance at different stages in the chemotherapy process may be good quantitative measures for assessing response to chemotherapy.

6.4. References

[1] Booi RC, Krücker JF, Goodsitt MM, O'Donnell M, Kapur A, LeCarpentier GL, Roubidoux MA, Fowlkes JB, Carson PL. Evaluating thin compression paddles for mammographically compatible ultrasound. Ultrasound in Medicine and Biology 2007; 33(3): 472-482.

[2] Booi RC, Krücker J, Goodsitt MM, O'Donnell M, Kapur A, LeCarpentier GL, Roubidoux MA, Fowlkes JB, Carson PL. "Evaluation of thin compression plates for mammographically compatible breast ultrasound." Proceedings of the 2004 IEEE Ultrasonics Symposium; p. 2129-2132.

[3] Booi RC, O'Donnell M, Knoth MM, Xie H, Hall AL, Rubin JM, Carson PL. "3D breast elastography with a combined ultrasound/tomography system." Proceedings of the 2006 IEEE Ultrasonics Symposium; p. 2056-2059.

[4] Booi RC, Carson PL, Erkamp RQ, et al. "Applying *in vitro* elasticity imaging results to optimize *in vivo* breast lesion characterization using a combined 3D ultrasound/digital x-ray system." Proceedings of the 2005 IEEE Ultrasonics Symposium; p. 727-730.

[5] Booi RC, Carson PL, O'Donnell M, Richards MS, Rubin JM. Diagnosing cysts with correlation coefficient images from 2D freehand elastography. J of Ultras in Med 2007 *(in press).*

[6] Booi RC, Carson PL, O'Donnell M, Roubidoux MA, Hall AL, Rubin JM. Characterization of cysts using differential correlation coefficient values from 2D and 3D elastography. Ultrasound in Medicine and Biology 2007 *(in press).*

[7] Lubinski MA, Emelianov SY, Raghavan KR, Yagle AE, Skovoroda AR, O'Donnell M. Lateral displacement imaging using tissue incompressibility. IEEE Trans Ultrason Ferroelectr Freq Control 1996; 43(2): 247-256.

[8] Techavipoo U and Varghese T. Improvements in elastographic contrast-to-noise ratio using spatial-angular compounding. Ultras in Med and Biol 2005; 31(3):529-536.

[9] Techavipoo U, Chen Q, Varghese T, and Zagzebski JA. Estimation of Displacement Vectors and Strain Tensors in Elastography Using Angular Insonifications. IEEE Transactions on Medical Imaging 2004; 23(12):1479-1489.

[10] Techavipoo U, Chen Q, Varghese T, Zagzebski JA, and Madsen EL. Noise Reduction Using Spatial-Angular Compounding for Elastography. IEEE Transactions on Ferroelectrics, and Frequency Control 2004; 51(5):510-520.

[11] Roubidoux MA, LeCarpentier GL, Fowlkes JB, Bartz B, Pai D, Gordon SP, Schott AF, Johnson TD, Carson PL. Sonographic evaluation of early-stage breast

cancers that undergo neoadjuvant chemotherapy. J Ultrasound Med. 2005; 24(7):885-95.

[12] Hall TJ, Zhu Y, Spalding CS. In vivo real-time freehand palpation imaging. Ultrasound Med Biol 2003; 29:427-435.

[13] Garra BS, Céspedes EI, Ophir J, et al. Elastography of breast lesions: initial clinical results. Radiology 1997; 202:79-86.